UNIVERSITY OF CALIFORNIA,
IRVINE

Fundamental Investigation of Directed Energy Deposition: Understanding the Process Through In-situ Monitoring and Numerical Simulations

DISSERTATION

submitted in partial satisfaction of the requirements
for the degree of

DOCTOR OF PHILOSOPHY

in Materials Science and Engineering

by

Sen Jiang

Dissertation Committee:
Professor Julie M. Schoenung, Chair
Professor Timothy J. Rupert
Distinguished Professor Diran Apelian

2021

TABLE OF CONTENTS

LIST OF FIGURES

LIST OF TABLES

ACKNOWLEDGEMENTS

I would like to begin by expressing my deepest gratitude to my amazing advisor, Professor Julie M. Schoenung, for offering me the opportunity to work in her research group. It has been a wonderful experience in every respect. I would like to thank for her guidance, encouragement, and patience. As she oversaw me throughout my entire PhD, she has exemplified what it is to be an insightful researcher and a dedicated professor. The help and support I received from her will undoubtedly benefit me for the rest of my life. I am so lucky to have her as my advisor.

Many thanks to my committee members, Distinguished Professor Diran Apelian and Professor Tim Rupert, for their invaluable suggestions for my dissertation and enlightening discussions regarding my research.

I would like to extend my great appreciation to Dr. Baolong Zheng, for being both my mentor and friend, offering me detailed guidance and explanation on every part of my research. Without his help I could not have made the progress that I did.

I must express my thanks to Dr. James Haley, who inspired me a great deal. I am particularly indebted to him for teaching me, step by step, how to use COMSOL® and explaining things in detail. It is my hope that I did not annoy him too much with my endless questions. His patience with me in this regard was greatly appreciated.

I am thankful for the financial support from the BIAM-UCI Research Centre for the Fundamental Study of Novel Structural Materials (Research Agreement #210263). It has been a wonderful experience collaborating with Prof. Enrique Lavernia, Prof. Tim Rupert, and Prof. Lorenzo Valdevit. I am grateful for their technical discussion, insight, and tremendous assistance on my work. I also would like to acknowledge Dr. Yizhang Zhou for his advice and coordination in this project, Dr. Xin Wang for her help with TEM works, and Dr. Benjamin MacDonald for his

help with work related to CALPHAD. Special thanks to Prof. Jean-Pierre Delplanque from UC Davis for his advice and assistance on many of the simulations in this work.

I also had the great pleasure of collaborating with Prof. Eliaz and David Svetlizky from Tel Aviv University, Israel, on the research project for the Israel Ministry of Defense, P.O. No. 4440873734. It has been a fun and fruitful experience working with them and I learned a lot from their unparalleled knowledge.

Last but not the least, my heartfelt thanks go out to my labmates and friends in the JMS and EJL groups. You are such brilliant people who were always supportive, respectful, and professional. You've made the past five years a wonderful and memorable experience. It is my hope we can continue our collaboration for many years to come. Best wishes to all of you.

Some portions of the text in this dissertation is a partial reprint of the material as it appears in the following publication:

- A.L. Vyatskikh, T.B. Slagle, **S. Jiang**, S.A. El-Azab, U. Scipioni Bertoli, L. Valdevit, E.J. Lavernia, J.M. Schoenung. "Thickness-dependent microstructure in additively manufactured stainless steel*," Journal of Materials Engineering and Performance*. *(In Press, 2021)*
- K.L. Terrassa, T.R. Smith, **S. Jiang**, J.D. Sugar, J.M. Schoenung. "Improving build quality in Directed Energy Deposition by cross-hatching," *Materials Science and Engineering: A*. 765, 138243 (2019)

CURRICULUM VITAE

Sen Jiang

Education

University of California, Irvine (UCI) December 2021

PhD in Materials Science and Engineering

Dissertation title: "Fundamental Investigation in Directed Energy Deposition: Understanding the Process Through In-situ Monitoring and Numerical Simulations"

Advisor: Professor Julie M. Schoenung

University of California, Santa Barbara (UCSB) December 2014

BA in Chemical Engineering

Publications

S Jiang, B. Zheng, D. Svetlizky, Y. Zhou, L. Valdevit, N. Eliaz, E.J. Lavernia, J.M. Schoenung. "Determining the process window for retaining encapsulated ZA-8 particles in direct energy deposition." *(In preparation)*

S. Jiang, B. Zheng, X. Wang, B.E. MacDonald, J.M. Schoenung. "Phase formation in directed energy deposited nickel-based superalloy composites." *(In preparation)*

S. Jiang, B. Zheng, J.M. Schoenung. "Numerical simulation and visualization of particle flow during DED additive manufacturing of metal matrix composites." *(Submitted for initial review)*

X. Wang, B. Zheng, K. Yu, **S. Jiang**, E.J. Lavernia, J.M. Schoenung. "The role of cell boundary orientation on mechanical behavior: a site-specific micro-pillar characterization study," *Additive Manufacturing. (In Press, 2021)*

A.L. Vyatskikh, T.B. Slagle, **S. Jiang**, S.A. El-Azab, U. Scipioni Bertoli, L. Valdevit, E.J. Lavernia, J.M. Schoenung. "Thickness-dependent microstructure in additively manufactured stainless steel*," Journal of Materials Engineering and Performance*. *(In Press, 2021)*

K.L. Terrassa, T.R. Smith, **S. Jiang**, J.D. Sugar, J.M. Schoenung. "Improving build quality in Directed Energy Deposition by cross-hatching," *Materials Science and Engineering: A*. 765, 138243 (2019)

Research Experience

PhD researcher April 2016-November 2021

Department of Materials Science and Engineering, University of California, Irvine

- Fabricated 6 different compositions of ceramic reinforced Ni based superalloy composites samples via direct energy deposition (DED) additive manufacturing technique with superior tensile properties.
- Utilized microscopy (OM, SEM) to study microstructures of the DED deposited samples.
- Constructed 3D fluid dynamic models to study powder flow behavior during the DED process.
- Investigated influence of 2 scan strategies on thermal history with COMSOL heat transfer models.
- Constructed heat and phase transformation models in COMSOL to determine the required operation parameters to retain coated particles in DED depositions.
- Recorded high-speed videos and thermal images to study the molten pool dynamics during the DED depositions under ultra-sonic vibrations.
- Analyzed phase evolution of TiC reinforced superalloy composites with aids of CALPHAD software.
- Designed and deposited functionally graded material (FGM) via DED.

- Conduct daily maintenance, troubleshooting and modifications of DED system.

Research intern June 2013-August 2013

Center for Energy Efficient Materials, University of California, Santa Barbara

- Tested performance of multi-junction solar cells and recorded I-V curve using solar simulator.
- Improved procedure and equipment to get accurate and convenient testing and measurement.
- Gave a formal presentation to 50-member colleagues and mentors.

Conferences Presentations

S. Jiang, B. Zheng, X. Wang, B.E. MacDonald, Y. Zhang, J.M. Schoenung. *Particle injection and phase formation in directed energy deposited nickel-based superalloy composites.* 151th TMS annual meeting, Anaheim, CA, 2022. [Invited]

S. Jiang, B. Zheng, D. Svetlizky, Y. Zhou, L. Valdevit, N. Eliaz, E.J. Lavernia, J.M. Schoenung. *Behavior of coated particles in directed energy deposition.* 151th TMS annual meeting, Anaheim, CA, 2022.

D. Svetlizky, B. Zheng, **S. Jiang**, Y. Zhou, L. Valdevit, N. Eliaz, E.J. Lavernia, J.M. Schoenung, N. Eliaz. *Design and fabrication of a novel Al-based self-healing metal-matrix composite.* 151th TMS annual meeting, Anaheim, CA, 2022. [Plenary]

A. Vyatskikh, T. Slagle, **S. Jiang**, S. El-Azab, U. Scipioni Bertoli, L. Valdevit, E.J. Lavernia, J.M. Schoenung. *Section Thickness Dependent Behavior in Additively Manufactured Stainless Steel.* 150th TMS annual meeting, Virtual, 2021.

S. Jiang, BL. Zheng, E.J. Lavernia, J.M. Schoenung. *Numerical simulation and high-speed photography characterization of powder delivery during LENS® additive manufacturing for metal matrix composites*. 149th TMS annual meeting, San Diego, CA, 2020.

B. Zheng, X. Wang, **S. Jiang**, B. Chen, J. Liang, S. Huang, Y. Zhou, E.J. Lavernia, J.M. Schoenung. *Micro-Mechanical characterization of directed energy deposited 316L stainless steel with hierarchical microstructure.* 149th TMS annual meeting, San Diego, CA, 2020.

S. Jiang, B.L. Zheng, J.C. Haley, EJ. Lavernia, J.M. Schoenung. *Powder flow, melting and solidification process in additive manufactured Ni-based metal matrix composites*. 148th TMS annual meeting, San Antonio, TX, 2019.

J. Haley, P. Kiani, **S. Jiang**, B. Zheng, J.M. Schoenung, E.J. Lavernia. *Quantifying particle-melt interactions via in-situ high speed imaging in Laser Engineered Net Shaping (LENS).* 148th TMS annual meeting, San Antonio, TX, 2019.

Teaching and Mentoring Experience

Graduate Interconnect Mentor

University of California, Irvine March 2018-December 2018

- Mentored 8 incoming international graduate students with orientation and English writing

Math Tutor

Sierra College September 2011-June 2012

- Assisted in teaching of undergraduate math courses.
- Helped students with calculus and physics problems from classes.
- Led discussion section for groups of 5-10 students.

Additional Experience

U.S. Army Reservist

Automated logistics specialist (MOS: 92A) May 2015-December 2018

Technical Skills

- Materials characterization: scanning electron microscopy (SEM), energy dispersive X-ray spectroscopy (EDS), electron backscattered diffraction (EBSD), focused ion beam (FIB), X-ray diffraction (XRD), Transmission electron microscopy (TEM), high-speed camera, thermal imaging.
- Mechanical tests: tensile, compression, micro-hardness.
- Materials processing: wire electrical discharge machining (EDM), Laser Engineered Net Shaping (LENS).
- Wet chemistry.
- Computer software and programming: Python, Matlab, Mathematica, C++, COMSOL, Thermocalc, ANSYS, Solidworks, Origin, ImageJ, Microsoft Office.

Language

English (fluent), Chinese (native speaker)

References

Julie M. Schoenung, Professor and Department Chair
Department of Materials Science and Engineering
University of California Irvine
Email: julie.schoenung@uci.edu
Phone: 530-902-4418

Enrique Lavernia, Distinguished Professor
Department of Materials Science and Engineering
University of California Irvine
Email: lavernia@uci.edu
Phone: 949-824-6296

Tim Rupert, Professor
Department of Materials Science and Engineering
University of California Irvine
Email: trupert@uci.edu
Phone: 949-824-4937

ABSTRACT OF THE DISSERTATION

Fundamental Investigation of Directed Energy Deposition: Understanding the Process Through In-situ Monitoring and Numerical Simulations

by

Sen Jiang

Doctor of Philosophy in Materials Science and Engineering

University of California, Irvine, 2021

Professor Julie M. Schoenung, Chair

Directed Energy Deposition (DED), one of the additive manufacturing techniques, has seen rapid growth over the last decade in multiple industries, including aerospace, medical devices, and energy systems. Although showing great potential and having proven itself a promising manufacturing alternative, the complex physics and highly non-equilibrium processes involved in DED exhibit unique challenges in optimizing the design parameters and controlling the overall quality of the final parts. Often times the entire process is treated as a "black box", in which the effort has been focused on correlating the final built properties with input parameters, without fully understand the governing physics. This dissertation aims to provide a deeper understanding of the fundamental physics at each stage during the DED process, with the aid of in situ process monitoring tools and numerical simulations. In the first study, particle flow behavior of a gas atomized metallic powder (Inconel 718) and a ceramic powder (TiC) during the coaxial nozzle injection was studied through both experimental and numerical analysis. A 3-dimensional COMSOL numerical model was formulated to simulate the particle trajectories under the influence of gas flow, particle-gas interactions, and particle-wall collisions. High-speed photography was

used to examine and compare the powder flow behavior of the Inconel 718 and TiC particles. The results reveal distinct differences in particle velocity and spatial distribution between the Inconel 718 and TiC particles, due to the dissimilar particle sizes, morphologies, material densities, and particle collision behavior. Next, thermal behavior of coated particles during the interaction with the molten pool was studied by constructing heat and phase transfer models using COMSOL software. Transient temperature and phase fields were calculated for coated and uncoated stainless steel (SS316L) and Zn-Al particles under different particle size, coating thickness, molten pool temperature and coating material conditions. Particle residence time values, defined as how long the particle can exist before undergoing a certain phase change, were determined from the calculations. The results show large variations in residence time due to the external parameters, especially the thermal diffusivity of the coated materials. Recommendations regarding coating material selection for retaining the Zn-Al particle were made based on the calculation results. In the third study, macroscopic thermal histories for a cuboidal build were analyzed in a 3-dimensional heat transfer model. Hatch rotation angle of 0 and 90 degrees were compared. A more randomized thermal history was observed for the 90-degree hatch rotation angle, which may inhibit epitaxial grain growth due to the dissimilar heat flux from pre-deposited layers. Finally, the tensile deformation behavior and phase formation in two nickel-based superalloys, Inconel 718 and Haynes 282, plus TiC-reinforced metal matrix composites of these alloys, were characterized experimentally for DED as-deposited samples. Scheil solidification calculations were also performed to understand the role of Nb (in the Inconel 718) and excess Ti and C (from the partially dissolved TiC reinforcement particles) on the phase formation sequence during solidification. The results reveal that the excess Ti+C leads to Nb-rich carbide formation in the Inconel MMCs, which depletes the Nb in the matrix and thus limits the formation of Laves and γ” phases. This leads to

the Inconel MMC matrix having a similar composition as in the Nb-free Haynes MMC matrix, and yields similar tensile behavior in the two sets of bulk, as-deposited MMC samples. These studies, combined, provide insight into the importance of materials properties and phase transformations in comprehensively understanding the DED process to facilitate expanded application in the industry.

Chapter 1: Introduction to Directed Energy Deposition Process and Research Tools

1.1. Directed energy deposition overview and process description

Directed energy deposition, or DED, refers to a type of additive manufacturing process, which uses a high energy source such as a laser, electron beam or electric arc, to melt and deposit feedstock materials to form dense metallic parts. The technique allows the fabrication of metallic parts with complex geometries via a layer-by-layer building pattern by implementing computer aided design (CAD) files. Many high-performance materials have been successfully deposited, including stainless steels, titanium-based alloys, cobalt-based alloys, nickel-based alloys, aluminum alloys, high-entropy alloys, intermetallics, shape memory alloys, ceramics, composites, and functionally graded materials (FGMs) [1]. Figure 1 shows a schematic representation of a typical laser based DED system [2]. The powder feedstock is first injected through a co-axial nozzle onto the substrate by a carrier gas, often argon or nitrogen, and simultaneously irradiated by a high energy density laser source from above. A small molten pool forms on the substrate upon heating by the laser source, and the powder feedstock interacts with the molten pool, being captured and melted. A metal track forms as the substrate moves, and desired parts can be fabricated as the material is continuously deposited according to the prewritten CAD codes.

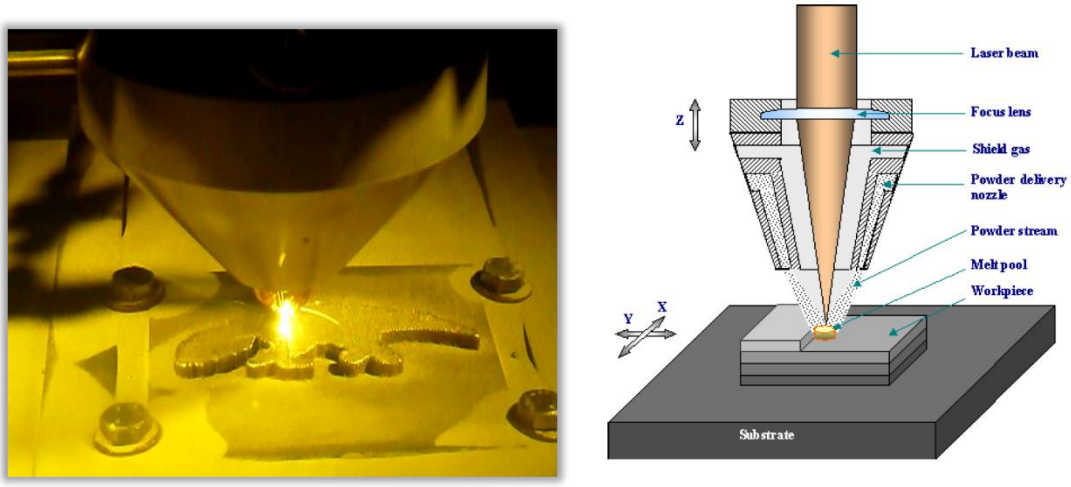

(a) (b)

Figure 1. (a) Photograph of directed energy deposition (DED) during deposition of stainless steel part, and (b) schematic representation of DED system. Courtesy of Zheng et al. [2]

As shown from the above, DED is an extremely complicated process with many physical and non-equilibrium phenomena happening simultaneously, including but not limited to: heat transfer (conductive, convective and radioactive), mass transfer (Marangoni flow, gas flow, particle-gas interactions) and phase transformations (melting, evaporating, solidification). These physical phenomena depend on important parameters such as laser power, scan speed, and powder flow rate, and will have strong effects on the quality and mechanical properties of the final parts [3]. Such complexity leads to difficulties in easily understanding the overall process and direct effects of parameters on part quality, and poses challenges to develop stable and reliable approaches for mass production. To address the above issues, extensive research has been done to characterize, analyze and quantify the DED process and establish good correlations between process parameters and material properties. In-situ monitoring and simulations are two important tools among in this research.

1.2. In-situ process monitoring tools

To achieve high levels of quality and reproducibility in metallic additive manufactured parts, in-situ monitoring tools are necessary to characterize the process and control the key variables [4]. This section introduces two major types of the in-situ process monitoring tools used in additive manufacture related research, namely high-speed photography and thermal imaging.

High speed photography

As stated previously, DED is a highly non-equilibrium process that involves multiple physical phenomenon, including turbulent flow of carrier gas and powders, rapid heating, melting, cooling and solidification. Starting from the powder feedstock leaving at the nozzle exit to the deposition of materials onto the substrate, the entire process takes only about several milliseconds. Therefore, utilizing high speed photography to characterize and monitor the DED process can be extremely useful to understand the complex physics that are happening. High-speed photography has been used to study two aspects in the DED process: (i) powder delivery and (ii) molten pool dynamics. For the first, particle trajectories when leaving the nozzle can be observed. Particle speed, mass flux, and particle concentrations can be obtained by post-processing of the recorded images. Figure 2 represents an example of work from Ref. [5], in which the images of a powder stream of two different materials, namely NT-20 nickel alloy and WC, were captured using a CCD camera with 30 frames per second (fps). Particle concentrations at various nozzle distances and particle velocities for both powders were obtained from the images, and the influence of nozzle angle, carrier gas flow rate, particle shape factor and particle diameter on particle concentration were analyzed. Similarly, Haley et al. [6] recorded the flow pattern for gas atomized 316L stainless steel powder during LENS® deposition at 10000 fps with an iX iSpeed 720 camera. Image analysis

software was used to count the positions of the particle from each frame, and a 2D-Gaussian distribution analytical model was proposed.

Other than observing particle flow behavior, the high-speed videos can also be used to study the molten pool dynamics. Molten pool morphologies and the mechanisms for particle interaction with each other and being captured by the molten pool can be revealed from the recorded images of the molten pool surface. Figure 3 shows an example study from Haley et al. [7], who used four high-speed cameras with >10000 fps to capture trajectories of individual powder particles impacting the molten pool. Different stages of particle-molten pool interactions are recognized, and the relationship between particle residual time and surface tension of the molten pool was obtained. Bertoli et al. [8] used similar high-speed photography to observe the deposition of SS 316L in selective laser melting (SLM). Cooling rates were estimated from the captured videos by dividing the difference of boiling point and melting point with measured time interval. Cooling rates for numerous single tracks were estimated and compared to a COMSOL finite element model, and the resultant solidification microstructure were used to validate the calculated and measured cooling rate values.

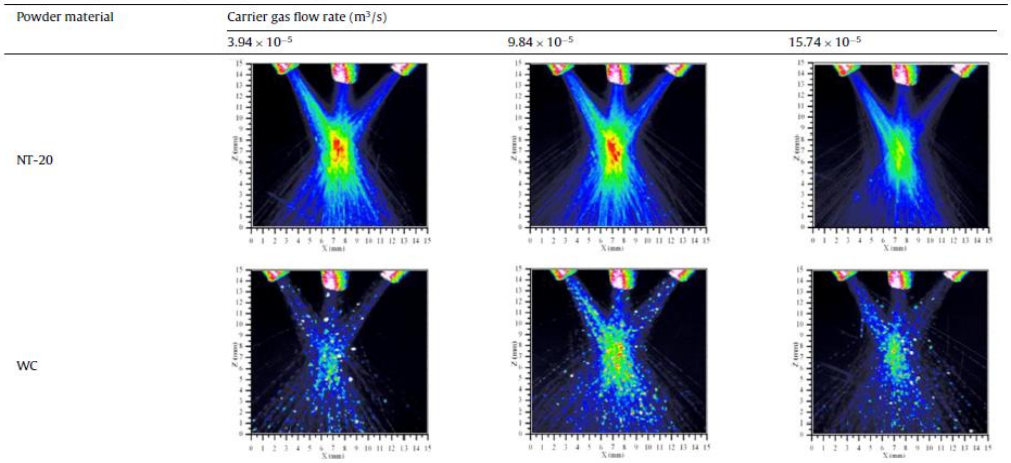

Figure 2. Flow of Ni–WC powder with different mass fractions of the micro and nano-sized WC powder and monolithic micro-sized WC powder at three different carrier gas flow rates. Courtesy of Balu et al. [5].

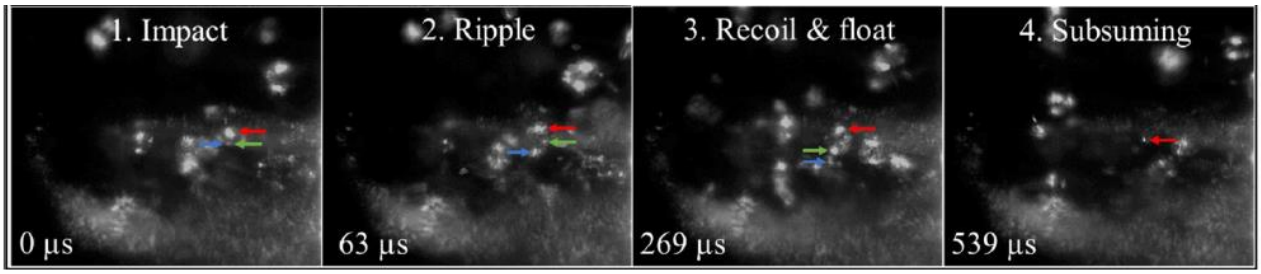

Figure 3. Color coded arrows highlight generated contrast points tracking the particle through four characteristic stages. Courtesy of Haley et al. [7].

Thermal imaging

The temperature field near the molten pool is of great interest since important physical values such as cooling rate and temperature gradient can be determined [9]. Due to the rapid cooling and highly non-equilibrium nature of the laser deposition process, conventional thermal couples may not be sufficient to quickly measure the temperature. Therefore, non-contact thermal imaging methods have been applied to acquire temperature information from the molten pool. A typical system contains a CCD to detect the thermal radiation signal reflected from the molten pool and convert it into an electrical signal [4]. The intensity of the radiation can be then quantified and converted to temperature data, upon careful calibration, according to the material properties. An example, shown in Figure 4, is from Ref. [10], digital CCD camera is installed above the laser beam to capture images of the molten pool, during the LENS® deposition of WC-Co thick-wall samples. The signal was later calibrated to convert to a temperature measurement, and cooling rate and temperature gradient information were obtained from the captured images. The temperature data were later validated with a numerical finite difference model.

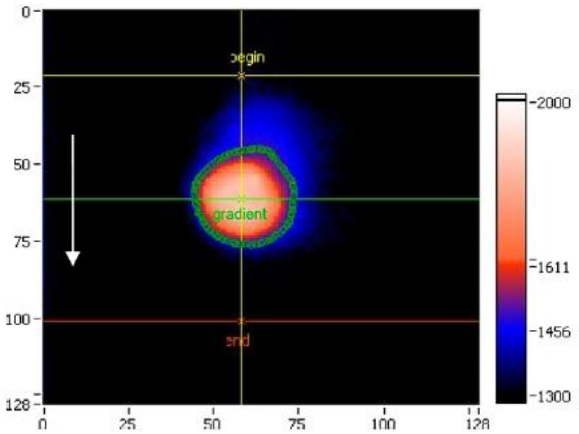

Figure 4. A thermal image of a WC–Co thick-wall sample looking from the top when layer 5 was being deposited. The image is colorized to show temperature in degrees K. Values on the X- and Y-axes show image size in pixels. The white arrow indicates the traverse direction of the laser beam. Courtesy of Xiong et al. [10].

1.3. Simulation methods

Despite the advantages of the in-situ monitoring tools described above, limitations are that both high-speed photography and thermal imaging devices can only probe the surface of the build but not at interior locations [9]. Therefore, simulation tools are beneficial as they can provide comprehensive analysis of physical processes, and potentially reduce the burden for extensive experimental work.

Transient, three dimensional (3D), temperature fields are prerequisites for understanding the most important parameters that affect the metallurgical quality of the components, such as the cooling rates, solidification parameters, microstructures and residual stresses and distortion of the components [9]. Due to the constraints of computing time, some simplifications need to be made when constructing simulation models. Perhaps the most simplified (and famous) model to describe the temperature field generated from a moving heat source is the Rosenthal equation, commonly cited in welding literature [11]. This equation assumes an infinitely large substrate, a point heat

source, ignores any mass addition and considered only conductive heat transfer. The temperature field has the following form [12]:

$$T - T_0 = \frac{q_0}{2\pi kR} \exp\left[-\frac{v}{2\alpha}(R + x)\right] \quad (1)$$

with

$$R = \sqrt{x^2 + y^2 + z^2} \quad (2)$$

where T is the temperature, T_0 is the initial temperature, q_0 is the energy source power, v is the scanning speed (motion is assumed to be in the positive x-axis direction), α is the thermal diffusivity, k is the thermal conductivity, and x,y,z are coordinates with respect to the laser spot. Since the Rosenthal equation gives infinite temperature at the origin (laser spot), some variations in the analytical model have been proposed, such as Ashby & Easterling [13] (assuming line-shaped heat source) and Eagar & Tsai's solution [14] (assuming a Gaussian distributed heat source). These analytical models, since not considering convective fluid flow in molten pool, tend to overestimate the temperature and molten pool size [9]. To have a better reproduction of the molten pool dynamics, numerical simulations have been used, including finite element methods (FEM) and finite difference methods (FDM). Solving fully coupled heat transfer and fluid flow equations are required to obtain accurate calculations of the 3-D temperature field. The governing equations are listed below for conservation of mass, momentum and energy [12]:

$$\frac{\partial(\rho u_i)}{\partial x_i} = 0 \quad (3)$$

$$\frac{\partial(\rho u_j)}{\partial t} + \frac{\partial(\rho u_j u_i)}{\partial x_i} = \frac{\partial}{\partial x_i}\left(\mu \frac{\partial u_j}{\partial x_i}\right) + S_j \quad (4)$$

$$\rho \frac{\partial h}{\partial t} + \frac{\partial(\rho u_i h)}{\partial x_i} = \frac{\partial}{\partial x_i}\left(\frac{k}{C_p}\frac{\partial h}{\partial x_i}\right) - \rho \frac{\partial \Delta H}{\partial t} - \rho \frac{\partial(u_i \Delta H)}{\partial x_i} \quad (5)$$

where ρ is the density, u_i and u_j are the velocity components along the *i* and *j* directions, respectively, and x_i is the distance along the *i* direction, *t* is the time, μ is the dynamic viscosity, *Sj*

is a source term for the momentum equation that accounts for buoyance forces, electromagnetic forces etc., h is the sensible heat, Cp is the specific heat, k is the thermal conductivity, and ΔH is the latent heat. Figure 5 shows an example of FEM simulation results for the deposition of Inconel 718 [15]. Once the transient temperature field has been calculated, important parameters such as cooling rate, temperature gradient, molten pool size, and heat flux can be determined and correlated with operating parameters and microstructural evolution.

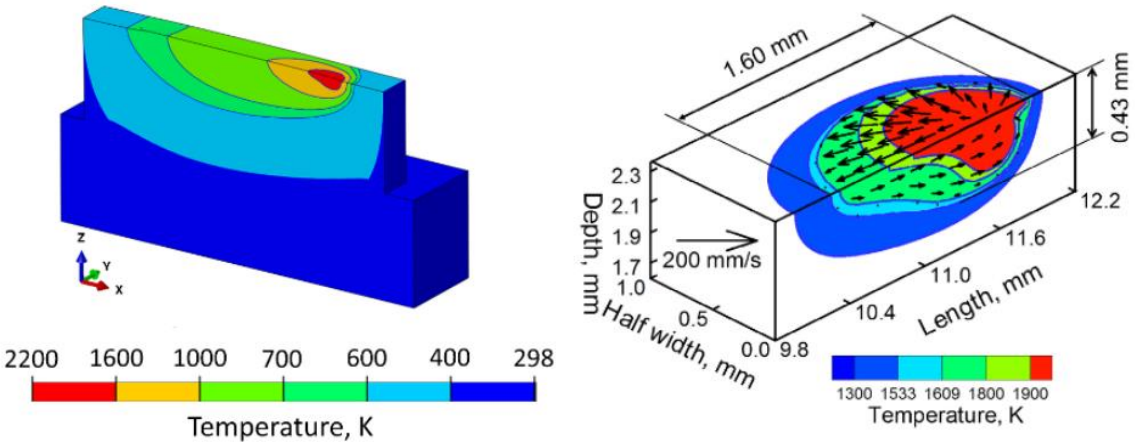

(a) (b)

Figure 5. Simulation results showing: (a) the temperature distribution during the deposition of 10th layer of Inconel IN718; (b) the temperature and velocity field near the molten pool during the deposition of 2nd layer of IN718. Courtesy of Mukherjee et al. [15].

1.4. Current challenges for novel and emerging materials

In recent years, the DED technique has seen rapid growth, and the fabrication with pure alloys such as steels, nickel-, titanium- and aluminum-based alloys, has become relatively mature. As DED offers excellent flexibility compared to laser powder bed fusion (PBF), another major type of additive manufacturing, the demand for using DED to manufacture novel materials, such as metal matrix composites (MMC) and functionally graded materials (FGM), is also growing at a rapid pace. Often these materials contain more than one type of feedstock powder, therefore their inhomogeneous nature can cause unique challenges during the deposition process. For example,

in MMC materials, the metallic powder and the ceramic reinforcement powder usually exhibit very different morphologies, size and density. When feeding the two powders simultaneously, the flowability of the powder mixture may be reduced due to the interlocking and entangling of irregular-shaped ceramic particles, and therefore leads to the formation of porosity in the solidified part [16]. Furthermore, since the melting point of ceramic particles is usually much higher than that of metallic particles, the ceramic particle may remain mostly unaffected or only partially melted during DED, therefore resulting in a molten pool containing solid reinforcements [16]. The solid reinforcement particles may exert a unique influence on the solidification structure, and the chemical interaction between any dissolved ceramic reinforcement and the metallic matrix may lead to unexpected phase formation. Even worse, the poor wettability between the solid reinforcements with the surrounding melt may result in the formation of porosity and cracks [16]. While the new technologies brings new opportunities, it also brings new challenges. Understanding better the DED process is essential to improve and solve these existing issues for manufacturing of complex material systems.

1.5. Research scope

The goal of this dissertation is to provide a fundamental investigation into the DED process and physics involved, with the aid of in-situ process monitoring tools and numerical simulations. The overall scope of this dissertation is shown in Figure 7. The chapters are arranged such that each chapter discusses a stage of the DED process: powder flow behavior during powder delivery (Chapter 2), particle-molten pool interactions (Chapter 3), macroscopic thermal histories (Chapter 4) and solidification/phase formation in as-deposited MMCs (Chapter 5). In Chapter 2, a computational fluid dynamic (CFD) model was constructed in COMSOL for analyzing particle

flow behavior of larger, spherical Inconel 718 powder and smaller, irregular shaped TiC powder. Particle mass concentration distribution and particle velocity were calculated, and the calculation results were validated by high-speed videos. The work provides insight into how the morphologies of the powder feedstocks ultimately determine the dispersion angle of the particle stream, the particle mass concentration, and the particle focal distance, which are key design parameters for DED. In Chapter 3, the thermal effect of particle coatings when interacting with the molten pool was studied through numerically modeling the heat transfer and phase transformation. The correlations between coating material, coating thickness, molten pool temperature and the particle residence time were evaluated. In Chapter 4, the work shifts to a relatively macroscopic scale of heat transfer phenomena, to analyze the thermal histories of the entire part. Temperature field, histories and heat flux were calculated and compared when adopting different hatch rotation strategies. Efforts have been made to use the calculated temperature data to explain the relationship between scan strategy and the microstructural and mechanical properties of the deposited parts. In the final part of this dissertation, phase formation in TiC-reinforced nickel MMCs was examined by microscopy and rationalized with the aid of CALPHAD. Scheil solidification calculations were performed for both Inconel 718/TiC and Haynes 282/TiC MMCs, to analyze the phase formation sequence during DED solidification. The work highlighted the interesting role that the Nb element plays in the composite material systems. The combination of these studies demonstrated an integrated overview on DED process and research tools to expand the applications in the future.

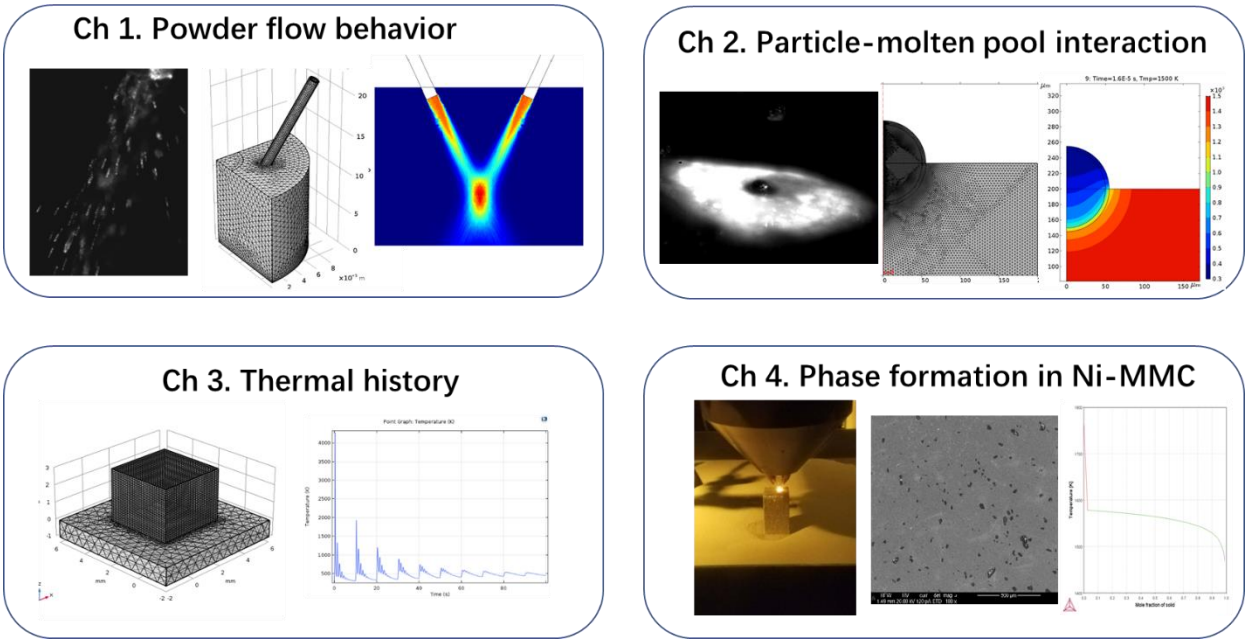

Figure 6. Schematic representation of the overall scope for this dissertation.

Chapter 2: Directed Energy Deposition of Metal Matrix Composites: Computational and Experimental Comparison of Powder Particle Flow Behavior

2.1. Introduction

Laser Engineered Net Shaping (LENS®) is one of several so-called directed energy deposition (DED) additive manufacturing techniques, which is rapidly gaining acceptance for the fabrication of metallic components. LENS® uses a laser beam as a heat source to melt and deposit injected metal powder onto a substrate via a line-by-line and layer-by-layer building pattern from a computer-aided design file [17]. The powder feedstock is carried by an inert gas, usually argon, onto a substrate, where the powder interacts with the laser beam and the molten pool and eventually becomes deposited. In addition to a wide range of metal alloys, LENS® has also been implemented to fabricate metal matrix composite (MMC) materials. The layer-by-layer additive material deposition allows for the production of parts with complex geometries while eliminating the need for postprocessing and machining [18–20]. MMCs consisting of metallic matrix materials including stainless steel, titanium alloys, nickel alloys and aluminum alloys, and ceramic reinforcement particles including TiC, TiB_2, WC, B_4C, Al_2O_3 etc., have been reportedly fabricated via LENS® [21–27].

Despite limited success with various combinations of metal and ceramic powders, it has become apparent that the delivery of a heterogeneous mixture during LENS® presents some unique challenges. For the material to be successfully deposited onto the substrate, powder particles must be efficiently delivered to and be captured in the molten pool created by the laser beam. For metallic alloys, the powders used in DED systems are usually near-spherical shaped, gas atomized

powders, with diameters ranging from 45-150 μm [9]. Gas atomized powders are selected because of their good flowability and high packing density [9,27,28]. However, ceramic particles often have small particle sizes and irregular morphologies that make the powder delivery difficult [16,29]. The powder flowability tends to decrease with increasing ceramic reinforcement particle content due to the interlocking and entangling of the irregular shaped particles, resulting in non-homogeneous microstructures and porosity in the deposited parts [29]. The range of particle morphologies and differences in physical properties between the metal and the ceramic particles affect their spatial distribution in the particle stream, and consequently influence the final microstructure and local composition in the deposited materials [30,31]. Furthermore, the overall process efficiency is critically influenced by the design and operational parameters of the powder injection nozzle, which determines the particle mass concentration at the working distance and thus influences the particle capture efficiency [6].

In the LENS® process, the size and morphology of the feedstock particles, carrier gas flow conditions and nozzle geometry all affect the behavior of the particles during deposition, which further influence the number of powder particles being delivered into the molten pool. Coaxial powder feed nozzles are commonly adopted due to their versatility and relatively simple design and installation [32]. For simplicity, the particle mass concentration is often analytically modelled assuming the mass flux from each nozzle has a 2-D Gaussian distribution, with the standard deviation increasing with increasing nozzle distance [6,33,34]. Due to the dilute particle concentration, the collisions between particles can be safely ignored [6,34], so the overall mass concentration is simply a superposition from each nozzle. Recently, research studies have been reported on actual observations of the flight characteristics of various types of particles during delivery to the molten pool using high speed photography. For instance, Haley et al. [6] recorded

the particle flow pattern of gas atomized 316L SS during LENS® deposition using an iX iSpeed 720 camera operating at 10,000 frames per second (fps). Image analysis software was used to count the positions of the particles in each frame, and a 2D-Gaussian distribution analytical model was proposed. Balu et al. [5] captured the images corresponding to the particle stream of two different materials, a nickel alloy and tungsten carbide, using a CCD camera at 30 fps. Particle concentrations at various nozzle distances and particle velocities for both powders were obtained, and the results were validated by a fluid dynamic simulation model. Mazzucato [35] designed a new nozzle geometry to maximize the particle capture efficiency, and the particle flow performance was recorded by a high-speed camera and analyzed using ImageJ software. A computational fluid dynamic (CFD) model was used to validate the acquired particle stream shape and mass flux data. Their results, however, failed to reveal a clear trend as to how the carrier gas flowrate will impact the particle stream pattern. Some researchers have considered the effect of particle collisions against the nozzle inner wall and found that the collisions will also affect the formation of the particle stream morphology [36,37]. Still, an in-depth, quantitative analysis of collision phenomena remains to be established.

This work aims to reveal the distinct particle flow behavior of a gas atomized metallic powder and a ceramic powder in the LENS® process and to provide insight into the factors that influence the particle trajectories and spatial distributions, through both experimental and numerical analysis. The overall scope of work is shown schematically in Figure 7. Numerical simulations are performed using COMSOL Multiphysics® software, to investigate the gas flow, particle-gas and particle-particle interactions. Special attention was focused on how the differences in particle size, density and morphology between metallic and ceramic powders would result in distinct particle stream patterns and mass concentration profiles, by carefully addressing the effect

of random particle-nozzle wall collisions inside the nozzle. To validate the simulated results, we implement high-speed photography to observe the particle injection in the case of the Inconel 718 and TiC powder binary system. The particle spatial distributions for both types of powders are determined from the recorded images and statistically analyzed.

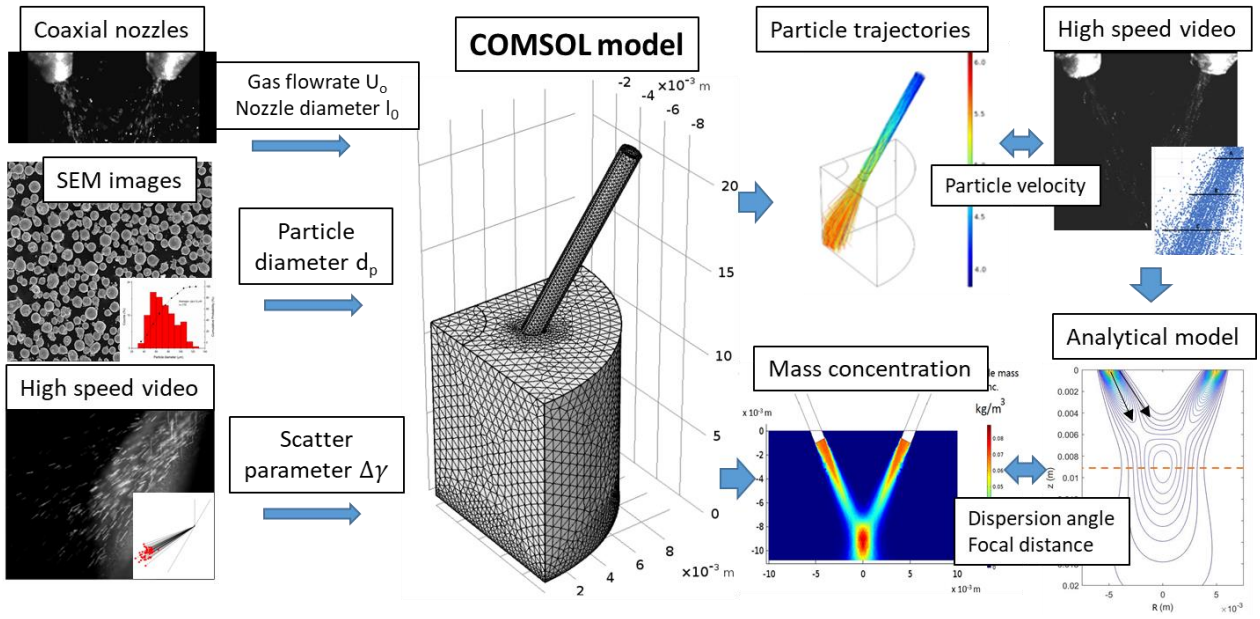

Figure 7. Schematic representation of the overall scope of Chapter 2.

2.2. COMSOL model methodology

A 3-D finite element method (FEM) model was formulated using COMSOL Multiphysics® 5.3a software to provide fundamental insight into the relative flow fields of the argon gas and the particles. The model solves the Navier-Stokes equations for a viscous and compressible gas with low Reynolds number, and computes the force balance for particles under the action of the drag of the argon flow. The computational sequence is set as two time-dependent steps: first, the argon flow field is calculated using a time-dependent solver, starting at t=0 s until steady state has been reached; second, powder particles are released from the nozzle inlet and injected toward the bottom

surface due to gravity and gas drag forces. Figure 8 shows the calculation domain and the geometry of the formulated model.

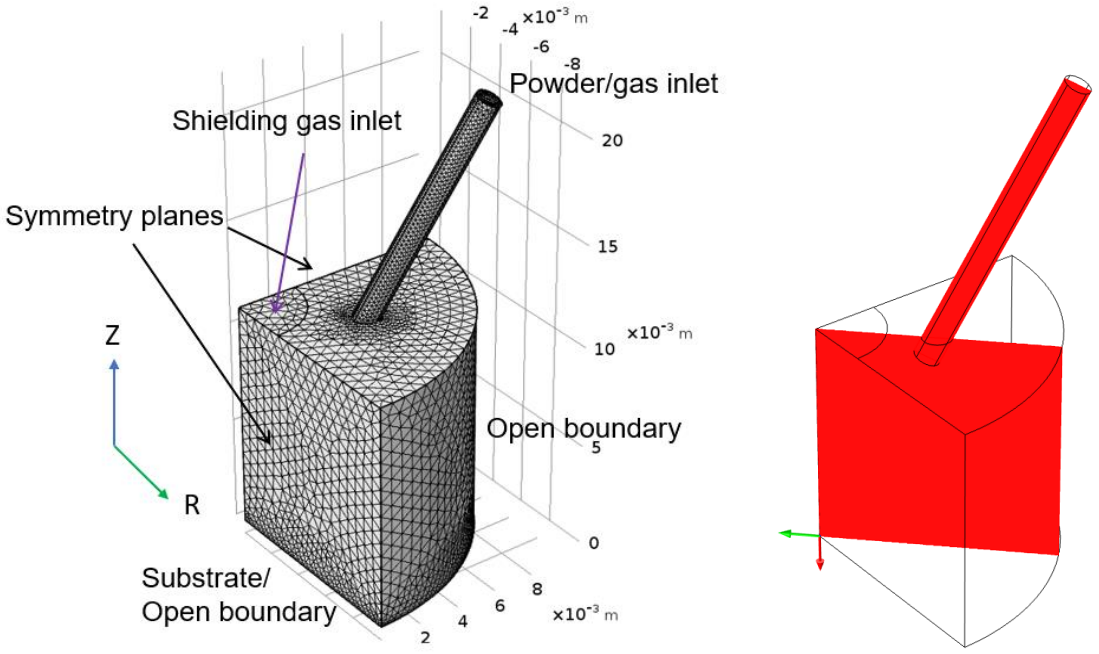

(a) (b)

Figure 8. (a) Calculation domain and the geometry of the 3-D COMSOL® model, and (b) the selected cut plane.

2.2.1 Gas flow field

The conservation of mass equation for a compressible Newtonian fluid can be expressed as follows [38]:

$$\frac{\partial \rho}{\partial t} + \text{div}\, \rho \boldsymbol{v} = 0 \tag{6}$$

where ρ is the density of the gas and $\boldsymbol{v}$ is the velocity vector of the carrier gas. The conservation of momentum can be expressed by Navier-Stokes equations, in Einstein notation [38]:

$$\rho \frac{d\boldsymbol{v}}{dt} = \rho \boldsymbol{g} - \nabla p + \frac{\partial}{\partial x_j}\left[\mu \left(\frac{\partial v_i}{\partial x_j} + \frac{\partial v_j}{\partial x_i}\right) - \frac{2}{3}\mu\, \delta_{ij}\, \text{div}\, \boldsymbol{v}\right] \tag{7}$$

where $\boldsymbol{g}$ is the acceleration due to gravity, p is the pressure of the gas, μ is the dynamic viscosity and δ_{ij} is the Kronecker delta.

The Reynolds number is estimated to range from 250-800 in this work, indicating the gas flow is mostly laminar in nature. However, to account for the possible turbulent flow during the injection, the standard k–ε model was used, in which turbulent kinetic energy (*k*) and viscous dissipation rate (ε) are considered [39]:

$$\rho \frac{\partial (k v_i)}{\partial x_i} = \frac{\partial}{\partial x_j}\left[\left(\mu + \frac{\mu_t}{\sigma_k}\right)\frac{\partial k}{\partial x_j}\right] + \boldsymbol{P}_k - \rho\varepsilon \tag{8}$$

$$\rho \frac{\partial (\varepsilon v_i)}{\partial x_i} = \frac{\partial}{\partial x_j}\left[\left(\mu + \frac{\mu_t}{\sigma_\varepsilon}\right)\frac{\partial \varepsilon}{\partial x_j}\right] + C_{\varepsilon 1}\frac{\varepsilon}{k}\boldsymbol{P}_k - C_{\varepsilon 2}\rho\frac{\varepsilon^2}{k} \tag{9}$$

$$\boldsymbol{P}_k = \mu_t[\nabla \boldsymbol{v} : (\nabla \boldsymbol{v} + (\nabla \boldsymbol{v})^T)] \tag{10}$$

$$\mu_t = \rho C_\mu \frac{k^2}{\varepsilon} \tag{11}$$

where *i*,*j*= 1,2,3, μ_t is the turbulent viscosity, $\boldsymbol{P}_k$ represents the sum of rate of production of kinetic energy and the generation of turbulence due to buoyancy, the empirical constants $C_{\varepsilon 1}$= 1.44, $C_{\varepsilon 2}$= 1.92, σ_k= 1.00, σ_ε= 1.3, and C_μ= 0.09. Equation (8) and (9) are solved simultaneously with the above equation (6) and (7) for Navier-Stokes and the continuity equations. The initial inlet gas velocity is set to be a fully developed flow, with an average flow rate of 3.78 L/min, as determined from the experimental measurements. The shielding gas is applied with a nozzle diameter of 5 mm and a flow rate of 20 L/min, directed downward. No slip boundary conditions are assumed for the nozzle inner wall and the substrate, and open boundaries are selected for all other surfaces.

2.2.2 Particle movement

The force balance on the powder particle can be expressed as [40]:

$$\frac{d\boldsymbol{u}}{dt} = \frac{3\mu C_D Re}{4\rho d_p^2}(\boldsymbol{v} - \boldsymbol{u}) + \boldsymbol{g}\frac{\rho_p - \rho}{\rho} \tag{12}$$

where $\boldsymbol{u}$ is the particle velocity, and ρ_p and d_p are the density and diameter of the particle, respectively. The drag coefficient C_D can be expressed using a correlation with the Reynolds number, Re and the sphericity suggested by Haider and Levenspiel [41]:

$$C_D = \frac{24}{Re}\left[1 + A(\varphi)Re^{B(\varphi)}\right] + \frac{C(\varphi)}{1+D(\varphi)/Re} \tag{13}$$

where *A, B, C, D* are parameters that are all functions of φ, the sphericity of the particle, and:

$$\text{A} = \exp\left(2.3288\text{-}6.4581\varphi\text{+}2.4486\varphi^2\right) \tag{14}$$

$$\text{B} = 0.0964\text{+}0.5565\varphi \tag{15}$$

$$\text{C} = \exp\left(4.905\text{-}13.8944\varphi\text{+}18.4222\varphi^2\text{-}10.2599\varphi^3\right) \tag{16}$$

$$\text{D} = \exp\left(1.4681\text{+}12.2584\varphi\text{-}20.7322\varphi^2\text{+}15.8855\varphi^3\right. \tag{17}$$

where φ is the sphericity. The Reynolds number can be expressed as:

$$\text{Re} = \frac{\rho d_p|\boldsymbol{u}-\boldsymbol{v}|}{\mu} \tag{18}$$

The sphericity φ is approximated from the particle projections in scanning electron microscopy (SEM) images (presented below in Figure 9a and 9b) using Cox circularity and is defined as follows [42]:

$$\varphi = \frac{4\pi A}{P^2} \tag{19}$$

where *A* is the area of the particle projection in the SEM image, and *P* is the perimeter of the particle. 170 Inconel 718 particles and 270 TiC particles were measured, respectively, and the average sphericity value were taken. φ is thus calculated to be 0.9 for the gas atomized Inconel 718 powder and 0.65 for the TiC powder. The influence of the particles on the gas flow and the interactions between particles were neglected due to the low volume fraction of particles in the nozzle (less than 0.1 vol% for dilute suspension [43]).

In addition to the gas flow field, particle trajectories are significantly affected by the initial conditions as well as by the collisions that occur against the inner wall of the nozzle. In this study, three initial and boundary conditions are considered: (a) parallel inlet; (b) cone inlet, with fully elastic wall collisions (hereafter referred to as 'cone-elastic'); and (c) cone inlet, with random wall collisions (hereafter referred to as 'cone-random'). A schematic representation of the three scenarios is shown in Figure 9. In the first scenario, particles are released with an initial velocity parallel to each other and perpendicular to the inlet surface. Under this condition, particles maintain their parallel trajectories and are unlikely to collide with the inner nozzle wall, unless their trajectory is altered by the gas field. In the second scenario, the particles are released with a certain initial tangential velocity component thereby forming cone-shaped trajectories. The angles corresponding to each particle follow a normal probability distribution, with the standard deviation set arbitrarily to 10^{o}. Most of the particles will hit the nozzle inner wall, and a fully elastic collision is assumed for the wall boundary condition. In the last scenario, particles are released at the same cone-shaped initial velocity but will experience random collisions against the nozzle due to the combined effects of the roughness of the inner wall surface and the irregular particle geometry. This irregular bouncing is handled by assuming that the incident and reflected angles follow the relationship suggested by Sommerfeld [44]:

$$\alpha' = \alpha + \Delta\gamma\zeta \tag{20}$$

where α is the incident angle, α'is the reflected angle, $\Delta\gamma$ is the scatter parameter, representing the variation in the reflected angle due to surface roughness and non-sphericity of the particles, and ζ is a Gaussian random number with zero mean and a standard deviation of one. The $\Delta\gamma$ values for both powders were determined via high-speed photography, as described in the next section.

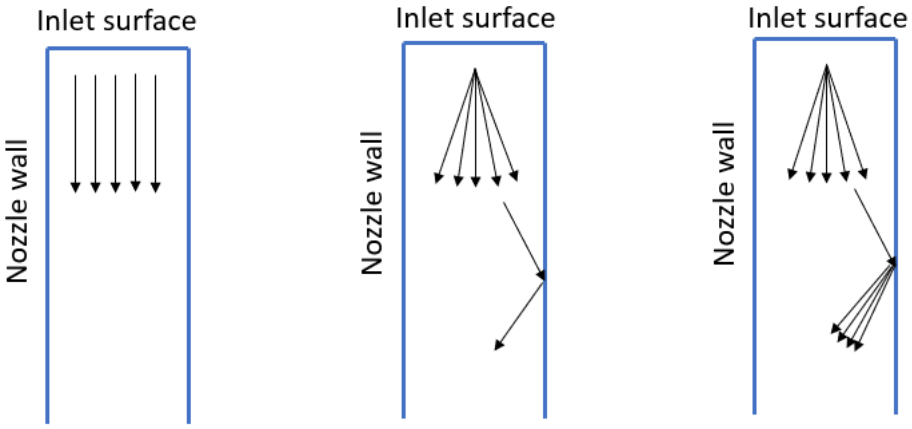

(a) (b) (c)

Figure 9. Select initial and boundary conditions for an inlet particle: (a) parallel inlet; (b) cone shaped inlet with fully elastic collision (cone-elastic) and (c) cone shaped inlet with random collision (cone-random)

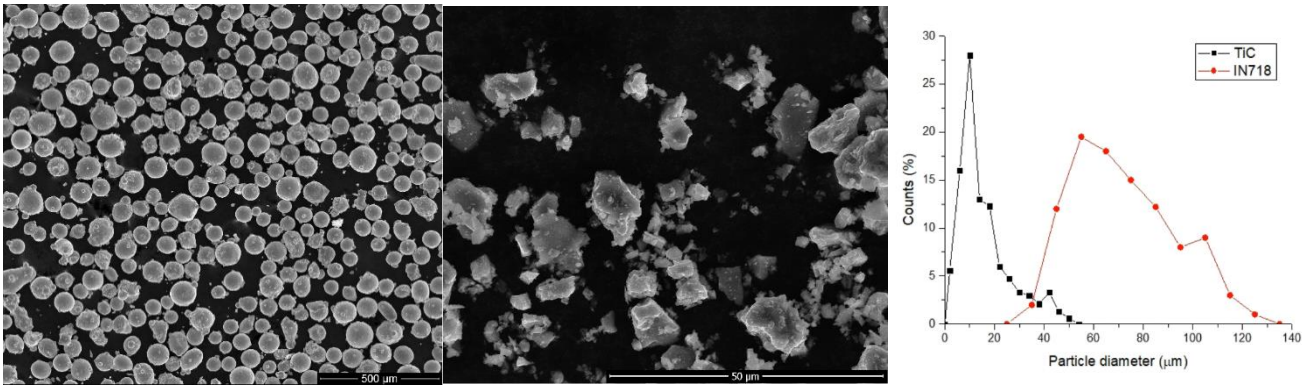

(a) (b) (c)

Figure 10. SEM micrographs for feedstock: (a) Inconel 718 powder and (b) TiC powder; and (c) particle size distributions. Note differences in magnification.

2.3. COMSOL model input parameters

The COMSOL model requires several input parameters to be specified, including operating parameters, powder particle sizes and scatter parameters. These values were empirically determined as described below, and the values uses are summarized in Table 1.

2.3.1 LENS® operating configuration

The LENS® 750 system (Optomec Inc. Albuquerque, NM, USA) used in this study consists of four coaxial nozzles angled at 25º along the vertical direction, with an inner nozzle diameter of 2.2 mm at the upper region, which decreases to 1.1 mm at the end tip. The argon carrier gas flowrate during normal operation was 6.3×10^{-5} m^3/s, and shielding gas flowrate was 3.3×10^{-4} m^3/s. The particle mass flowrates corresponding to these operating conditions are 3.92×10^{-4} kg/s and 2.41×10^{-4} kg/s for the Inconel 718 and TiC powders, respectively. Furthermore, it was assumed that the particles were generated randomly at the inlet surface with an initial velocity of 4 m/s, which is equal to the carrier gas velocity before entering the nozzle.

2.3.2 Particle size

The powder feedstocks considered in this study are gas-atomized Inconel 718 powder (Praxair Inc, 45 μm - 125 μm) and TiC powder (Advanced Powder Solutions, 5 μm - 45 μm). Figure 10 shows representative SEM images (FEI Quanta 3D SEM) of each powder and the associated particle size distribution (PSD) histograms. The average particle sizes were determined to be 64 μm and 14 μm, for the Inconel 718 and TiC powders, respectively. The particle sphericity was also measured from the SEM images as described in Section 2.2.

Table 1. Input parameters for COMSOL model

Property	Symbol	Value	Source
Average particle diameter	d_p	IN718: 64 μm TiC: 14 μm	Measured
Material density of the particle	ρ_p	IN718: 8200 kg/m^3 TiC: 4900 kg/m^3	[45] [46]
Gas velocity (before entering nozzle)	U_g	4 m/s	Measured
Gas velocity (entering nozzle)	U_o	16 m/s	Measured
Particle initial velocity	U_p	4 m/s	Assumed equal to carrier gas velocity before entering the nozzle
Characteristic length (nozzle diameter)	l_o	1.12 mm	Measured
Dynamic viscosity of Ar	μ	2.1x10^{-5} Pa·s	[47]
Scatter parameter	$\Delta\gamma$	IN718: 10^o TiC: 15^o	Measured

2.3.3 Scatter parameter $\Delta\gamma$

To determine the $\Delta\gamma$ for the particles, high-speed photography was used to measure the reflected angles and velocities of the particles when colliding with an inclined surface. Figure 11a represents a schematic diagram of the experimental set up, and Figure 11b is a snapshot of a captured video. A brass substrate was held steady and tilted to different angles (15^o, 30^o, and 45^o relative to the vertical direction) and carefully polished so that the surface roughness mimics the inner wall of the copper nozzle. A funnel was placed 20 cm above the substrate where powders were allowed to fall freely and collide with the inclined substrate. LED lighting was used to provide extra illumination. The incident and reflected angle (α and α'**)** and velocity before and after colliding with the substrate (U and U') for each powder were measured, and the results are summarized in Table S1 in the Supplemental Information. A total of 100 particles for Inconel 718

and TiC were measured, respectively, and the $\Delta\gamma$ was determined to be ~10^{o} for the Inconel 718 particles and ~15^{o} for the TiC particles. These parameters were used as inputs for the wall boundary conditions in the COMSOL model.

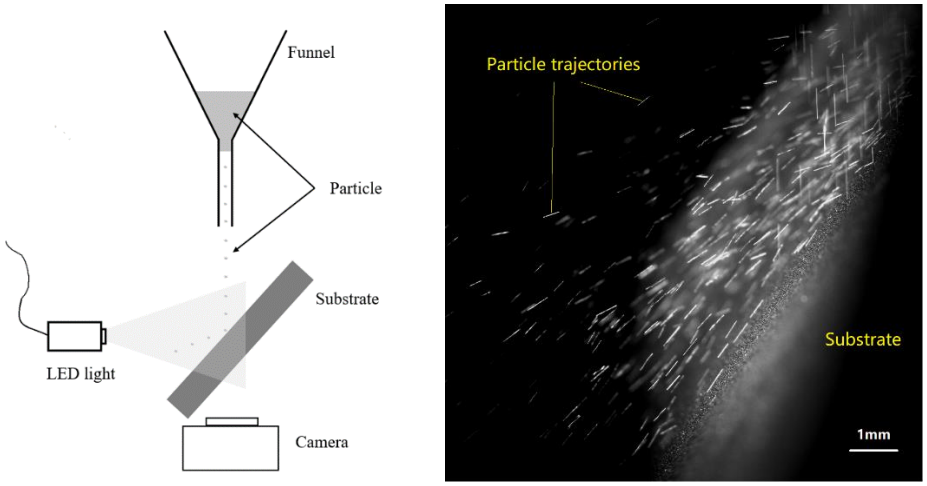

(a) (b)

Figure 11. (a) Schematic diagram of the experimental setup used to conduct particle collision measurements. (b) Representative snapshot from recorded high-speed videos.

2.4. COMSOL model simulation results

2.4.1 Particle velocity

Figure 12a shows the calculated gas velocity field at steady state. The gas flow maintains laminar flow characteristics, with streamlines mostly parallel at the nozzle tip. The velocity of the carrier gas decreases rapidly when leaving the nozzle exit and entering the open space beneath. Figure 12b plots the velocity of the carrier gas, Inconel 718 and TiC particles. Before the particles leave the nozzle (left side of the dashed line), the velocity of the carrier gas is higher than that of the particles, and thus the drag force causes the particles to accelerate. TiC particles accelerate to a faster speed, approximately 12 m/s, due to their smaller size and lower material density. The

carrier gas velocity is significantly reduced after leaving the nozzle exit and entering the open space (right side of the dashed line), and at the position where the gas velocity is slower than the TiC particle velocity, the particle will be decelerated until it reaches the substrate. The particle velocity is approximately 10.5 m/s when reaching the substrate. By contrast, for larger and heavier Inconel 718 particles, the speed is only accelerated to approximately 5 m/s, and the gas velocity is always higher than the particle velocity, and the particles do not experience deceleration after leaving the nozzle.

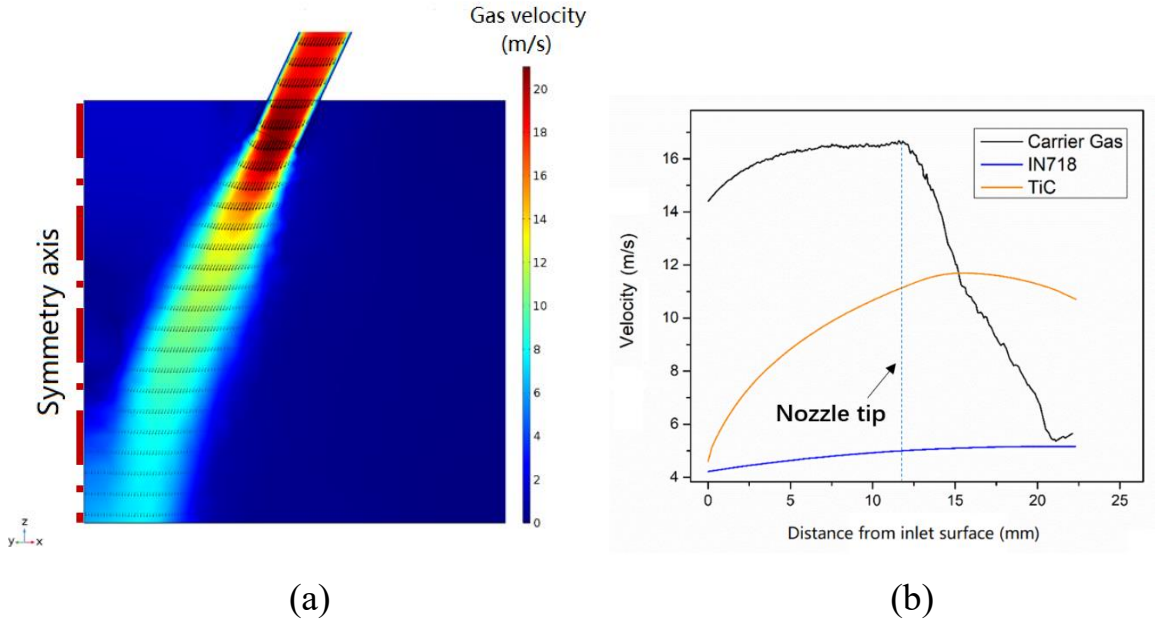

Figure 12. (a) Calculated gas velocity fields and (b) average velocity of the carrier gas, and the two types of powder particles, Inconel 718 and TiC, assuming parallel inlet. Dashed line represents the position of the nozzle tip.

2.4.2 Particle trajectories and mass concentration profiles

Figure 13 shows the calculated particle trajectories and mass concentration profiles for Inconel 718 (a-c) and TiC (d-f) under different inlet and wall collision conditions. Figure 13a and d assume a parallel inlet for the particle velocity initial condition, i.e., each particle is released perpendicular to the releasing surface. The trajectories for both Inconel 718 and TiC particles

remain straight and parallel after leaving the nozzle until they reach the substrate, and the argon carrier gas does not significantly alter the particle trajectories. The carrier gas does, however, cause the particle to accelerate inside the nozzle, as indicated by the velocity color scales shown in Figure 12b.

Figures 13b and e show the particle trajectories for the cone-elastic conditions. In this scenario, the particle trajectories now diverge instead of remaining parallel when they exit the nozzle due to the collision effect. Due to its lower particle velocity, an Inconel 718 particle will have a lower axial velocity component when leaving the nozzle, and thus tend to be more divergent than a TiC particle, which has a higher velocity. Figures 13c and f show the particle trajectories for the cone-random conditions. The particle trajectories in this case appear to be more divergent for both Inconel and TiC particles, resulting from the random collisions during the flight inside the nozzle. In prior studies, the particle-wall collision phenomenon during the powder delivery process in DED was suspected to cause the particle streams to diverge under the nozzle [36,37]. In this study, the distinct morphologies of the Inconel 718 and the TiC particles lead to significant differences in collision behavior inside the powder nozzle. The gas atomized Inconel 718 particles are near-spherical in shape, while the TiC particles are facetted, with much lower sphericity (φ= 0.65), as shown in Figure 10. The irregular-shape, low sphericity nature of the TiC particles will result in more randomness when colliding against a flat surface, as indicated by the larger $\Delta\gamma$ value (15^o for TiC particles) compared to that for Inconel 718 particles (10^o). The higher degree of randomness in collisions associated with the TiC particles leads to a more divergent particle stream, i.e., TiC has a larger dispersion angle than that for Inconel 718. However, the higher velocity of the TiC particles reduces the residence time inside the nozzle and hence decreases the frequency of particle collisions with the nozzle wall, which slightly offsets the aforementioned effect and

leads to a more concentrated particle cloud. Furthermore, a more convergent particle stream means a higher mass concertration at the focal point (Figure S1). For the parallel inlet conditions, the particle streams are the most concentrated, with the highest maximum mass flux at the focal point. When the particle stream spreading is more divergent (cone-elastic and cone-random), the maximum mass flux decreased drastically, from 3.5 kg/m^2•s (parallel inlet) to 0.4 kg/m^2•s (cone-random) for Inconel 718 particles, and from 2.5 kg/m^2•s (parallel inlet) to 0.9 kg/m^2•s (cone-random) for TiC particles.

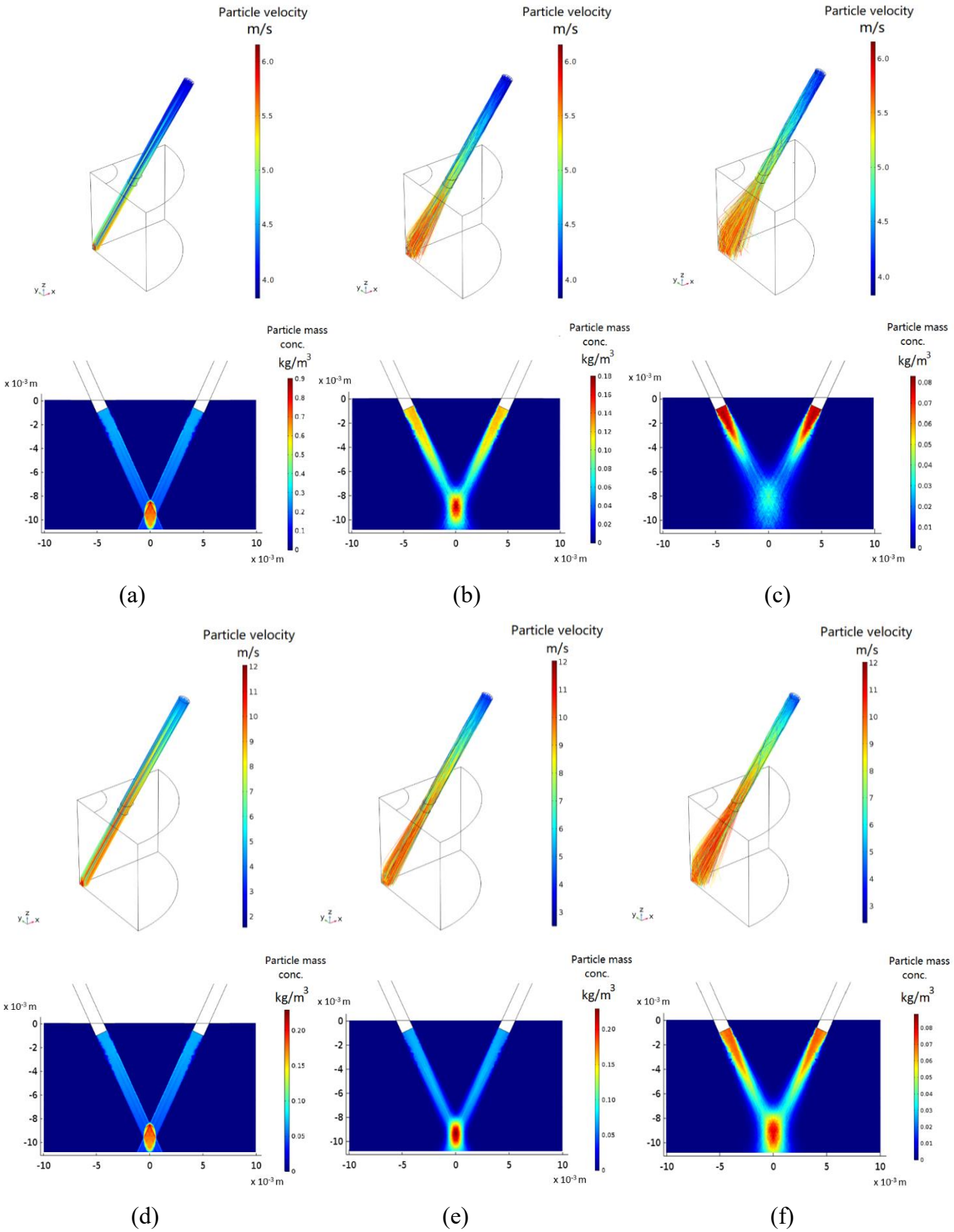

Figure 13. Calculated particle trajectories (top rows) and particle mass concentration between

the nozzle and the substrate (bottom rows). (a) (b) (c) for Inconel 718 particle, and (d) (e) (f) for TiC particle. (a) (d) parallel inlet; (b)(e) cone-shaped inlet with 10^{o} cone angle (cone-elastic); and (c)(f) cone-shaped inlet with random particle-wall collisions (cone-random).

2.5. Experimental validation

2.5.1 High-speed photography characterization

A Photron Fastcam SA-Z high performance high-speed camera equipped with a Model K2 long-distance microscope system was used to capture high-speed videos of the particle streams leaving the nozzle. A pulsed laser with a frequency of 60 kHz and 638 nm wavelength was used to provide additional illumination. Videos were recorded at a frame rate of 10,000 fps (see video files provided in the Supplemental Information); representative snapshots are provided in Figure 14a. From the recorded high-speed videos, differences in the particle flow behavior are evident and the following qualitative trends are observed: (1) the velocity of the TiC particles is higher than that of the Inconel 718 particles; (2) the TiC particle stream appears to have a wider distribution relative to that for the Inconel 718 powder; (3) the TiC particles have a focal point that is closer to the nozzle outlet than that for the Inconel 718 particles. Particle velocity values were determined from the captured images by multiplying the trajectory length and the frame rate. Due to the smaller particle size and lower material density, the TiC particles tend to accelerate to a faster velocity (6-7 m/s) as compared to that for the Inconel 718 particles (4 m/s). The particle velocity remained mostly unchanged for the Inconel 718 particles as the particle travelled along the nozzle axis, while the velocity decreased slightly for the TiC particles.

To further quantify the results, the captured images were processed using the MIPAR® software, allowing the centroid positions of each particle to be identified. The number of particles at select distances from the nozzle tip could then be determined, the results of which are plotted, along with fitted Gaussian distribution curves, in Figure 14b. A total of 100,000 particles were

counted for both Inconel 718 and TiC. The standard deviations are determined from the Gaussian curve fit of the particle number measurements. The statistical measurements (Figure S2) revealed that the standard deviation increases linearly with increasing nozzle distance, indicating that the particle streams expand and widen as they travel from the nozzle exit tip toward the substrate. The steeper slope for the TiC particles suggests that the TiC particle stream is expanding faster than the Inconel 718 particle stream. From the linear relationship, a dispersion angle can be defined as the arctangent of the slope of the linear fit. The dispersion angle is estimated to be 6^{o} for the TiC particles, and 3.5^{o} for the Inconel 718 particles. The dispersion angle will have a significant influence on the shape and focal distance of the particle stream, as illustrated in the next section.

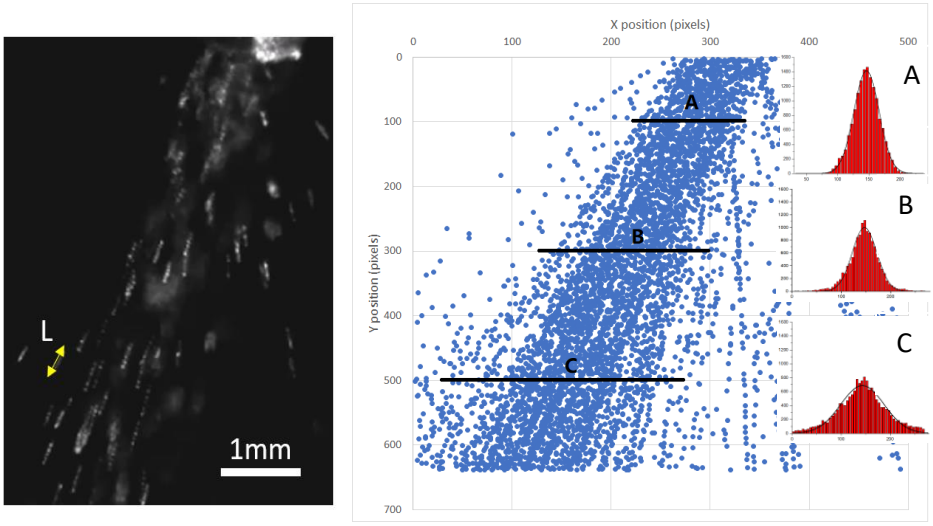

(a) (b)

Figure 14. (a) Snapshots from the high-speed videos showing the particle stream, and (b) particle centroid positions obtained from processed captured high-speed video images. A total of 100,000 particles are identified and counted, and the number density at different nozzle axial distances (represented by the black lines: A, B and C) are each plotted and fit with a Gaussian curve.

2.5.2 Analytical model

A good visualization of the spatial distribution of the particle mass concentration profile for four-coaxial nozzles can be obtained by applying the analytical model developed by Haley et al. [6].

The first section of the model was utilized and modified for the current study, in which the superimposed particle mass concentration profiles from the four nozzles were calculated for both Inconel 718 and TiC particles. The model assumes that the particle mass concentration profiles follow a 2-D Gaussian distribution with the standard deviation increasing linearly along the nozzle axial distance. The mass flux of the particle *J* was expressed using the following equation:

$$J(x,y,z) = \sum_{i=-1,1} \sum_{j=-1,1} \frac{F}{4} \cdot \frac{1}{2\pi\sigma^2} \exp\left(-\frac{x'^2+y'^2}{2\sigma}\right) \quad (21)$$

where *F* is the total mass flowrate of the particle stream, *x'* and *y'* are transformed coordinates oriented with *z'* being the nozzle axis direction, and the subscripts *i* and *j* represent the four nozzles. The standard deviation σ is linearly related to the tangent of the dispersion angle, θ_{disp}:

$$\sigma = z' \tan\left(\theta_{disp}\right) + \sigma_0 \quad (22)$$

where σ_0 is the fit standard deviation at *z'*=0. The mass concentration can be calculated:

$$C_m(x,y,z) = \frac{J}{v} \quad (23)$$

where *v* is the particle velocity and is assumed to be constant. Particles are assumed to not be affected by the carrier gas, and the diameter is assumed to be monodispersed, i.e., a constant.

Figure 15 shows the particle mass concentration contours generated when the dispersion angles obtained from the statistical measurements (3.5^o for Inconel 718 and 6^o for TiC) are applied. When ignoring the influences of the carrier gas, gravity and collisions between particles, the contours of the particle mass concentration profiles as the powder particles exit and travel from the nozzle tip to the substrate will depend only on the dispersion angle. As such, larger dispersion angles will result in a wider and more divergent distribution in the particle stream, as well as a shorter focal distance. Since the particle stream expands as particles travel along the vertical direction, the Gaussian curves for the particle mass concentration profiles become more flattened (larger standard deviation) at lower vertical positions (farther from the nozzle tip), and the two curves

move closer to each other and eventually merge The expansion of the particle stream causes the peak particle mass concentration (at the focal point) to be attained *before* the full overlap of the two Gaussian curves occurs. The expansion of a particle stream with a larger dispersion angle occurs at a faster rate than for the case with a smaller dispersion angle, and the two curves begin to overlap at a higher vertical position (closer to the nozzle tip), thus resulting in a shorter focal distance. Table 2 provides a summary of the focal distance for the two powders compared with the values obtained from the COMSOL simulations for the three inlet conditions. Because of the larger dispersion angle, the TiC particle stream has a shorter focal distance than the Inconel 718 particle stream, and therefore the TiC particles will be out of focus for the case when the working distance (the user-defined distance between the substrate and nozzle tips) is chosen on the basis of successfully depositing only Inconel 718. This condition will consequently yield a lower particle mass concentration and particle capture efficiency for the TiC powder particles. These results indicate that the selection of deposition conditions that are simultaneously optimal for both metal and ceramic particles present inherent challenges. It is worth noting, however, that particle mass concentration is relatively less sensitive to vertical position (larger "depth of field") for larger dispersion angles, which may facilitate a more flexible selection of working distance values. The factors that affect the dispersion angle are analyzed and discussed within the framework of the COMSOL Multiphysics® simulation results, as presented in the next section.

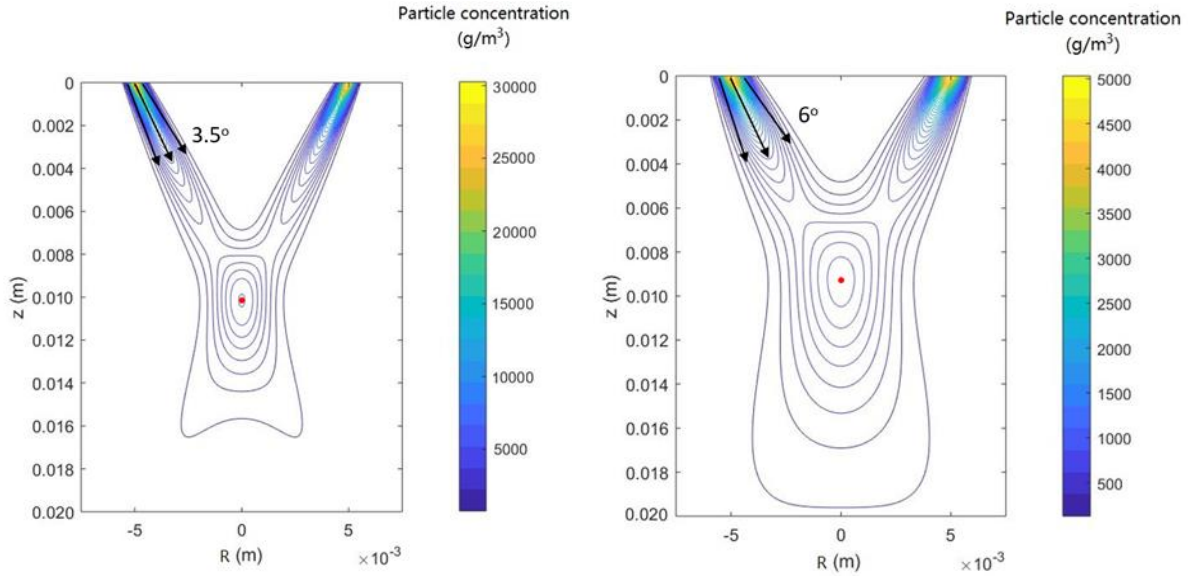

(a) (b)

Figure 15. Analytical model results for particle mass concentration contours: (a) IN718, dispersion angle of 3.5°; (b) TiC, dispersion angle of 6°. Z is the vertical distance from the nozzle tip; R is the horizontal radial distance from the center point between the two nozzles. The focal point is shown as a red dot in each figure. Note variations in scale.

Table 2. Particle focal distance (in mm) from nozzles under different assumed inlet conditions.

	Inlet conditions	**COMSOL model**	**Analytical model**
IN718	Parallel	10.3	10.2
	Cone-Elastic	10.0	
	Cone-Random	9.3	
TiC	Parallel	10.3	9.4
	Cone-Elastic	10.2	
	Cone-Random	9.9	

2.6. Discussion

2.6.1 Factors that determine the particle dispersion angle

As mentioned in an earlier section, the particle dispersion angle is the predominant parameter in describing the particle stream pattern. This dispersion angle is often pre-assumed in analytical models [34] or can be determined experimentally from high-speed photography [6]. Although it is known that many factors could potentially influence the value of the particle dispersion angle, a thorough and detailed analysis has yet to be established. Below we describe three parameters that are found to have significant influence on the particle dispersion angle based on the COMSOL simulations:

Initial particle inlet angle.

The initial velocity conditions for the particles entering the nozzle space are extremely difficult to determine, as it is almost impossible to accurately probe the particle trajectories inside a nozzle. In this numerical simulation, the particle is assumed to have a cone shaped inlet, with a cone angle arbitrarily set to 10^{o} (Figure 13b). However, the actual scenario may deviate from this assumption, and may be affected greatly by the geometry of the nozzle and particle-particle collision effect. A smaller cone angle would result in less divergent particle streams, and when the angle diminishes to zero, i.e., parallel inlet (Figure 13a), the particle streams become the most concentrated and thus with the smallest dispersion angle. Further analysis and better characterization techniques are required to fully understand the particle flow behavior inside the nozzle.

Particle-nozzle wall collisions.

The high-speed videos and COMSOL simulation results indicate that the particle-nozzle wall collisions play an essential role in the formation of the particle stream pattern. When taking

into account the random collision effects, the particle stream becomes more divergent as compared to the case when a fully elastic collision is assumed, i.e., $\Delta\gamma = 0$. This randomness is due to both the particle non-sphericity and the roughness of the nozzle inner wall surface. From the measurement results shown in Table S1, the TiC particles have a larger scatter parameter value ($\Delta\gamma$ ~ 15°) than that for Inconel 718 ($\Delta\gamma$ ~ 10°), most likely due to the irregular morphology of the TiC particles. This effectively increases the divergence of the TiC after impact and thereby results in a larger dispersion angle. Hence, our results suggest that using spherical or near-spherical powder feedstock could potentially facilitate the formation of a convergent particle stream. Moreover, past studies have found that fully elastic collisions could result in a larger particle dispersion angle as compared to the assumption of plastic collisions [36]. This result suggests that the nozzle material needs to be carefully selected such that the collision is more plastic in nature, in order to obtain a more convergent particle stream.

Particle speed.

The particle speed determines the particle residence time inside the nozzle, and therefore influences the collision frequency against the nozzle wall. A higher particle speed decreases the residence time and collision frequency, and consequently reduces the divergence caused by irregular particle-nozzle wall collisions. A smaller particle size and higher argon carrier gas flow rate could increase the particle velocity, and therefore contribute towards having a smaller dispersion angle and thus a more convergent particle stream.

2.6.2 Sensitivity analysis on particle size effects

The trajectory of a particle in a fluid flow field is very sensitive to the particle size, material density and particle morphology. A dimensionless number, the Stokes number (Stk), is usually used to describe the particle travel characteristics under the influence of a flow field. In

the case of Stokes flow where the Re number approaches zero, i.e., for very slow fluid velocity, the Stokes number is defined as:

$$\mathrm{Stk} = \frac{\tau U_0}{l_0} \tag{24}$$

where τ is the relaxation time of the particle:

$$\tau = \frac{\rho_p d_p^2}{18\mu} \tag{25}$$

U_0 is the fluid velocity far away from the particle, l_0 is the characteristic length of the fluid flow (nozzle diameter), and μ is the dynamic viscosity of the fluid. For Stk<<1, a particle will follow the streamlines closely, while for Stk>>1, a particle will tend to maintain its previous trajectory due to inertial forces. In non-Stokesian flow cases, a correction function $\Psi(\mathrm{Re_p})$ needs to be added for more accurate computation of the Stokes number [48]:

$$Stk_{eff} = \Psi\left(Re_p\right) \cdot Stk \tag{26}$$

where the correction function is defined as follows:

$$\Psi\left(Re_p\right) = \frac{24}{Re_p} \int_0^{Re_p} \frac{dRe\prime}{C_d(Re')Re\prime} \tag{27}$$

The drag coefficient C_d for non-spherical particles is calculated using Equation (13) in Section 2.2.2. An illustration on how the particle diameter and the Stokes number would affect the particle trajectories under a certain gas velocity field is shown in Figure S3. The Stokes number is calculated $\mathrm{Stk_{In718}} = 648$, and $\mathrm{Stk_{TiC}} = 15$ for the Inconel 718 and TiC particles, respectively. The smaller Stokes number for TiC particles, resulting from the smaller particle size, irregular shape and lower material density, means that it is more sensitive to changes in the fluid flow than Inconel 718 particles and could be accelerated by the carrier gas faster, as shown in Figure 12b. However, the Stokes number for both materials is much greater than unity, indicating that the gas flow may not have a significant effect on the particle flight trajectories. This is also supported by the high-

speed video observations, which show that the particles mostly maintained their initial flight direction when leaving the nozzle exit, instead of exhibiting wavy or turbulent trajectories. The divergence in the particle distribution patterns seen in the high-speed videos is more likely due to the collision phenomena described in the previous section.

2.6.3 Effect of molten pool vaporization

The high energy density laser beam can heat the molten pool to temperatures above the boiling point of many metals, resulting in vigorous turbulence and vaporization flow above the molten pool. The partial pressure of the resultant metal vapor could reach as high as several atmospheres [49]. Figure 16 shows snapshots of the recorded high-speed video (see videos 4 and 5 in Supplemental Information) for pure Inconel 718 and Inconel 718+TiC composites during LENS® deposition. The Inconel 718 particles are captured by the molten pool more easily than the TiC particles due to the size and density of the Inconel 718 particles being larger than the TiC particles. TiC particles (bright in the image), on the other hand, are shown to be significantly influenced by the vaporization torrent from the molten pool. TiC particles tend to be blown upward by the vapor and experience turbulent flow due to their fine particle size and low density. This may result in the TiC particles having difficulty being captured by the molten pool surface, and thus may lead to decreased TiC content in the final deposited part. More detailed research is required to account for this effect on the powder delivery process.

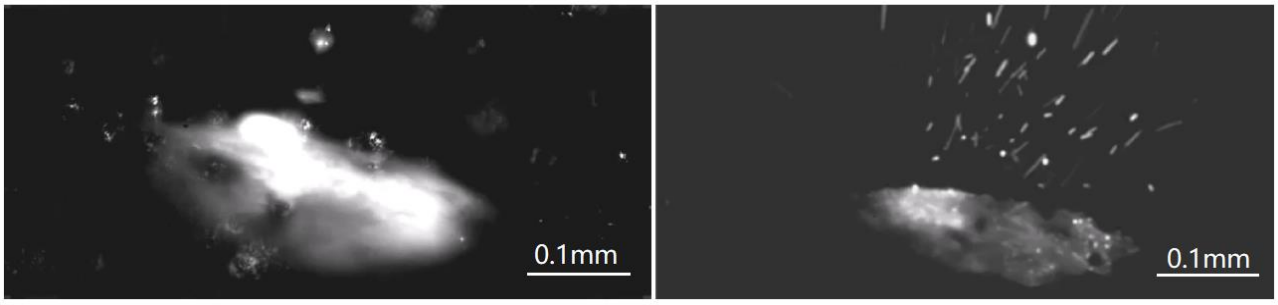

(a) (b)

Figure 16. Snapshots from the high-speed videos showing the molten pool for: (a) the pure Inconel 718, and (b) the blended Inconel 718+TiC. Videos were recorded at a frame rate of 20,000 frames per second, and can be found in the Supplemental Information (videos 4 and 5).

2.7. Summary

In this work, high-speed photography was used to observe the variation in the powder spray pattern, flow dynamics, velocity behavior and distribution of the particles with different sizes, morphologies and densities from four nozzles. A COMSOL numerical simulations of the gas field, particle-gas interactions and particle-wall collisions were performed to understand the physics during LENS® nozzle injection and to validate the experiment data. Key findings are summarized below:

(1) TiC particles have a higher velocity and larger dispersion angle than Inconel 718 particles during the powder injection process. The larger dispersion angle for TiC is expected to result in a shorter focal distance of the powder stream and thus decrease the TiC particle content in the final deposited material.

(2) Initial particle inlet angle, particle-nozzle wall collisions and particle flight velocities all affect the dispersion angle of the particle stream. Using spherical particles and higher carrier gas velocities may be beneficial to obtain a smaller dispersion angle and thus a concentrated particle mas concentration profile.

(3) Vaporization in the metal matrix molten pool can cause turbulent flow of the TiC reinforcement particles above the surface of the molten pool and may result in reduced particle capture efficiency.

Chapter 3: Thermal Behavior of Coated Particles in Directed Energy Deposition

3.1. Introduction

In powder based additive manufacturing (AM), the feedstock material quality is critical for obtaining high-level mechanical properties [50]. Studies have shown that the coatings can effectively reduce the surface roughness of the powder and therefore enhance flowability [51–53]. By applying appropriate coating and surface modification, the flowability of the powder can be promoted by decreasing the inter-particle friction [53], and potentially beneficial for powder spreading in powder bed fusion (PBF) [51,53] and powder delivery in directed energy deposition (DED) [52]. Gärtner et al. [53] applied ~ 13 nm sized SiO_2 coating to gas atomized CoCrFeNi powder using dry-coating method, and the flowability of the coated powders were characterized with dynamic angles. Their results showed that the dynamic angle decreased from 63–78° to 20–25° as the surface area coverage (SAC) increased from 0 % to 300 %. Similarly, Karg et al. [51] dry coated Al powder with 0.3 wt% SiOx nano particle for the laser powder bed fusion process. A 20-25 % drop in angle of repose was observed when the SiOx coating was applied to <20 μm Al powder. Other than for metallic powders, the coatings are more commonly seen in AM of ceramic and composite materials, to act as binders between ceramic particles as well as to prevent agglomeration of particles. For example, Cavaleiro et al [54]. used stainless steel thin film sputter coated WC for selective laser sintering (SLS), and near dense layers were produced. Zheng et al. [52] used Ni-coated TiC powders for fabrication of Inconel 625/TiC metal matrix composites with Laser Engineered Net Shaping (LENS®). Higher powder flowrate and TiC content were achieved when compared to non-coated powders in the as-deposited samples.

Coated particle can also find their applications in self-healing materials. The self-healing concept has gained more attentions across various fields, including automotive, aerospace, and building industries [55,56]. By enclosing micron-sized particles in an inert coating, microcapsules can be generated that isolate themselves from the external environments [55], and once reheated at higher temperatures such as 0.7-0.9 T_m, mass transfer of metal occurs producing either solid state or liquid phase bonding across powder interfaces to achieve self-healing effect [57]. One such example is in aluminum alloy, namely Al–8Zn–2.5Mg–1Cu, according to Lumley and Schaffer [57]. They have found that the porosity decreased by 8% due to the heterogeneous precipitation of the equilibrium of Zn-rich η phase ($MgZn_2$).

Despite these studies on preparing and characterization of coated particle, a systematic understanding of how coatings would affect the thermal behavior during the particle-molten pool interaction during DED is still lacking. Several modelling and high-speed video characterization studies have been done to observe and analyze the particle and molten pool dynamics [7,58,59]. Based on these works, it is well established that two particle capture regimes are identified when the particle reaches the molten pool surface: submergence regime and floating regime [7]. When the molten pool liquid can wet the surface of the particle and particle has a relatively high initial velocity, the particle will penetrate easily into the molten pool, resulting in a submergence regime. By contrast, if the particle and molten pool liquid exhibit poor wetting, the particle tends to oscillate on the surface of the molten pool because of the surface tension force, therefore leading to a floating regime [58,60]. Particle residence time, which represents how long a particle can exist on the molten pool surface before becoming fully melted, was either measured from the video or calculated and correlated with parameters including particle size, molten pool temperature and contact angle [7,58]. However, none of these works considered the effect of coating applied to the

impinging particles. Therefore, in the current study, a heat transfer model was constructed in COMSOL for both coated and uncoated stainless steel 316L and zinc/aluminum (ZA-8) particle. The transient temperature and phase field were calculated, and particle residence times were calculated and the influence of coating thickness, coating materials, particle radius and molten pool temperature were analyzed. Specifically, for ZA-8 particles, the material and process parameter selection criterion to retain the ZA-8 particle in the final deposited parts are discussed.

3.2. Numerical simulation methodologies

The meshes and geometries of the calculation domain are shown in Figure 17 for both submerging and floating regime. In this study, the particle was assumed to be half submerged in the molten pool for the floating regime. Molten pool flow and convective heat transfer were considered to be negligible to influence the particle residence time, given the fact that the Biot number for the particle, Bi, is estimated to be less than 0.1, which indicates that the heat conduction would be the dominating heat transfer mechanism inside the particle. The governing equation therefore is Fourier's heat equation :

$$\rho \cdot c_p \cdot \frac{\partial T}{\partial \mathrm{t}} = k\nabla^2 T \tag{28}$$

where ρ is the density of molten pool liquid, c_p is the specific heat capacity, and k is the thermal conductivity. To account for solid to liquid phase transition inside the particle, the material properties are expressed as functions of solid phase fraction θ:

$$\rho = \theta\rho_s + (1-\theta)\rho_l \tag{29}$$

$$k = \theta k_s + (1-\theta)k_l \tag{30}$$

$$c_p = \frac{1}{\rho}\left(\theta\rho_s c_{p,s} + (1-\theta)\rho_l c_{p,l}\right) + L\frac{\partial \emptyset}{\partial T} \tag{31}$$

where L is the latent heat of fusion and $\emptyset$ is an order parameter:

$$\emptyset = \frac{(1-\theta)\rho_l - \theta\rho_s}{2(\theta\rho_s + (1-\theta)\rho_l)} \tag{32}$$

The coating was assumed to maintain the solid phase during the entire simulation as the melting point for coatings are much higher than the assumed molten pool temperature. The molten pool is assumed to be in liquid phase during the entire simulation.

The molten pool far from the particle is assumed to cool down and follows the Newton's law of cooling, in which the cooling rate is proportional to the temperature difference:

$$\dot{T} = -\frac{1}{\tau}(T_i - T_{amb}) \tag{33}$$

where τ is the time constant, T_i is the initial temperature of the molten pool, and T_{amb} is the ambient temperature. The time constant τ can be written in the following form:

$$\tau = \frac{\rho c_p}{kd} \tag{34}$$

where d is the thickness of the molten pool. The molten pool temperature therefore follows exponential decay respect to time. For a very short period of time (t<3 ms in this study), the cooling rate can be assumed to be a constant, and thus the molten pool temperature is decreasing linearly with respect to time:

$$T_{mp} = T_i - \dot{T}t \tag{35}$$

The initial particle temperature is assumed to be equal to the ambient temperature, $T_p = T_{amb} = 293\ K$. All input parameters and materials properties are listed in Table 1.

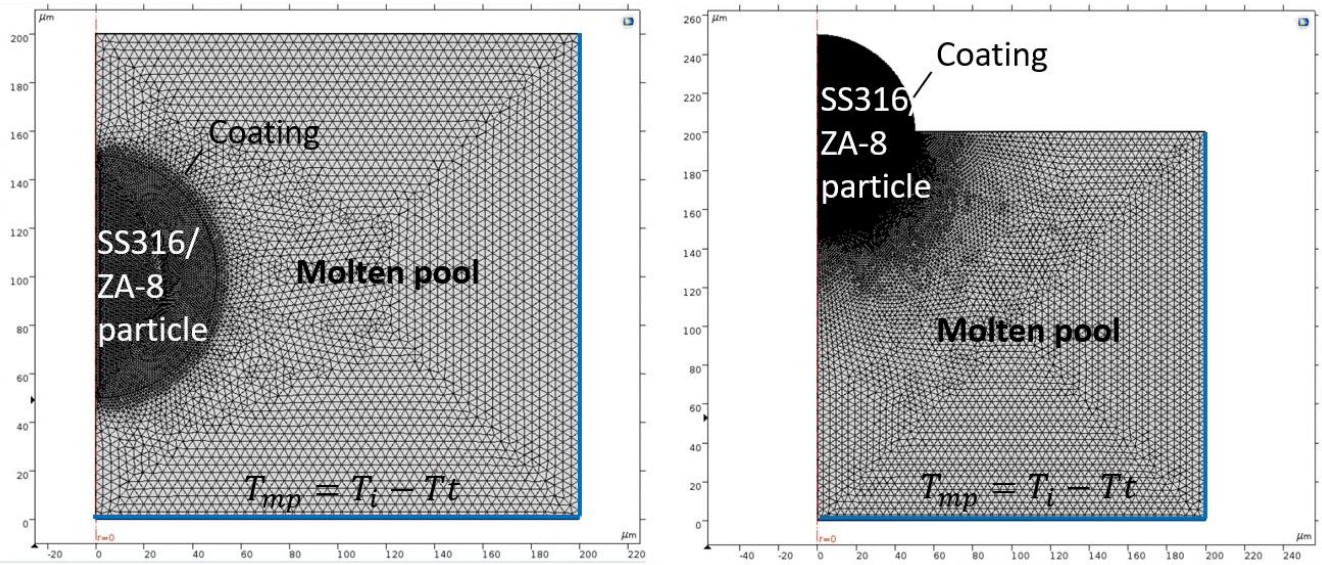

(a) (b)

Figure 17. Meshed calculation domain for (a) submergence regime and (b) floating regime.

Table 3. Input parameters for COMSOL models

Parameters	Description	Value		Units	Source
$c_{p,l}$	Liquid phase heat capacity	SS316	824	J/(kg·K)	COMSOL database
		ZA8	480		
		Al5083	1176		
$c_{p,s}$	Solid phase heat capacity	$c_{p,s}(T)$		J/(kg·K)	COMSOL database
d	Molten pool depth	2 x 10^{-4}		m	Assumption
k_l	Liquid thermal conductivity	$k_l(T)$		W/(m·K)	COMSOL database
k_s	Solid thermal conductivity	$k_s(T)$		W/(m·K)	COMSOL database
l	Coating thickness	2, 5, 10, 30, 50, 70		μm	Assumption
L	Latent heat of fusion	SS316	247	kJ/kg	[61]
		ZA8	101		[62]
L_{vap}	Latent heat of vaporization	ZA8	1782	kJ/kg	[63]
ρ_l	Liquid phase density	$\rho_l(T)$		kg/m^3	COMSOL database
ρ_s	Solid phase density	$\rho_s(T)$		kg/m^3	COMSOL database
T_{amb}	Ambient temperature	293		K	Assumption
T_p	Particle initial temperature	293		K	Assumption
T_i	Molten pool initial temperature	SS316	1800, 2000, 2200, 2400	K	Assumption
		ZA8	1300, 1400, 1500, 1600, 1700		

3.3. Simulation results

3.3.1. Silica coated stainless steel particle

Representative temperature fields and phase fields for a stainless steel 316 particle are shown in Figure 18 and Figure 19 for the submergence regime and floating regime, respectively. As the particle reaches the molten pool surface or penetrates into the molten pool, it is heated up quickly by the molten pool and the melting process starts after a short period of time. For uncoated

particles, the melting starts at less than 100 μs for both regimes (Figure 18b and Figure 19b). More liquid phase is formed as the heating process proceeds and eventually reaches 100% liquid, i.e., fully melted. The time elapsed to reach this fully melted state is defined as the particle's "residence time", indicated in Figure 18e and Figure 19e. Figure 20 shows the trend for residence time with respect to molten pool temperature and particle radius, and Figure 21 is a 3-D surface plot that combines these results. Significant increases in residence time are observed for increasing particle radius and decreasing molten pool temperature. In the floating regime, the residence times are more than twice as long as for the submerged regime, due to the reduced contact surface area between the molten pool and the particle. Large variations in residence times are observed, from 27 μs to 1400 μs.

Figure 22 shows the influence of a SiO_2 coating on the residence time for coating thickness values of 2 and 5 μm. Significant increases in residence time are seen when a SiO_2 coating was applied, as SiO_2 acts as a thermal barrier with significantly lower thermal diffusivity than SS316 (0.739 mm^2/s for SiO_2 vs. 4.08 mm^2/s for SS316 at room temperature).

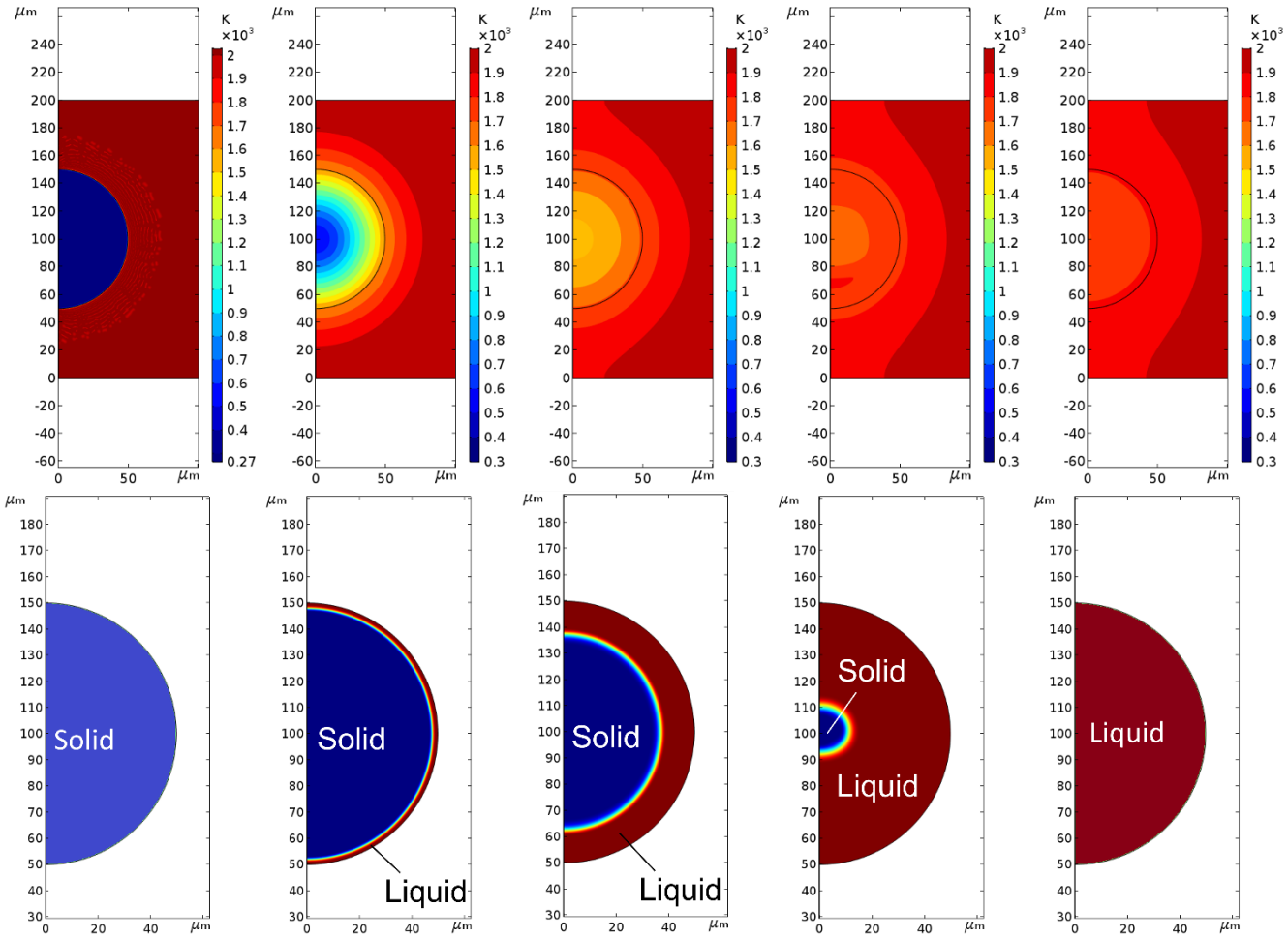

(a) (b) (c) (d) (e)

Figure 18. Representative temperature field (top row) and phase field (bottom row) for the submergence regime for stainless steel, SS316 particle at different simulation times: (a) t=0; (b) t=80 μs; (c) t=180 μs; (d) t=220 μs; (e) t=260 μs.

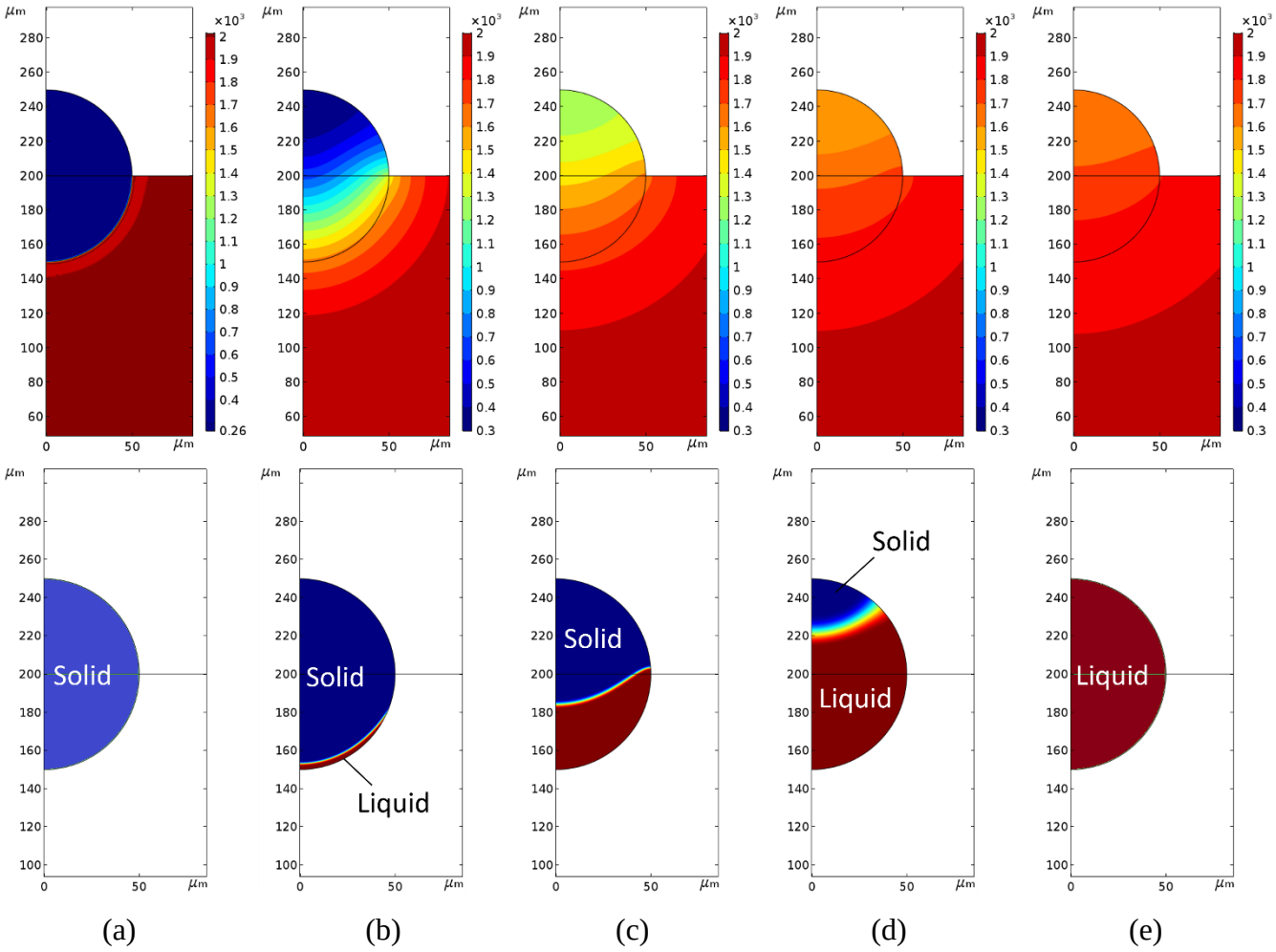

Figure 19. Representative temperature field (top row) and phase field (bottom row) for the floating regime for stainless steel, SS316 particle at different simulation times: (a) t=0; (b) t=80 μs; (c) t=370 μs; (d) t=630 μs; (e) t=750 μs.

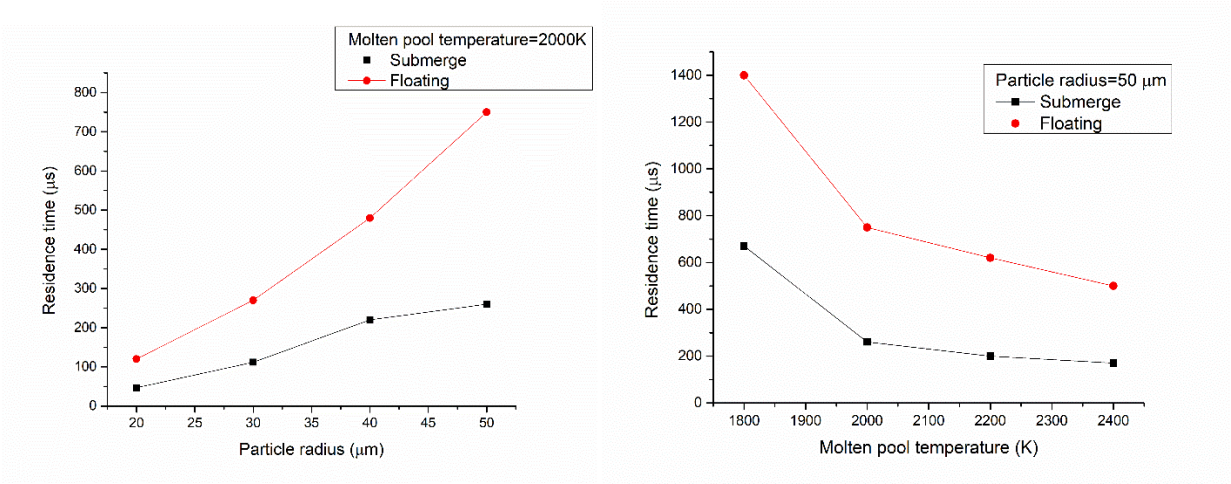

(a) (b)

Figure 20. Calculated residence times for stainless steel, SS316, for different (a) particle radius, assuming molten pool temperature of 2000 K, and (b) molten pool temperature, assuming particle radius of 50 μm.

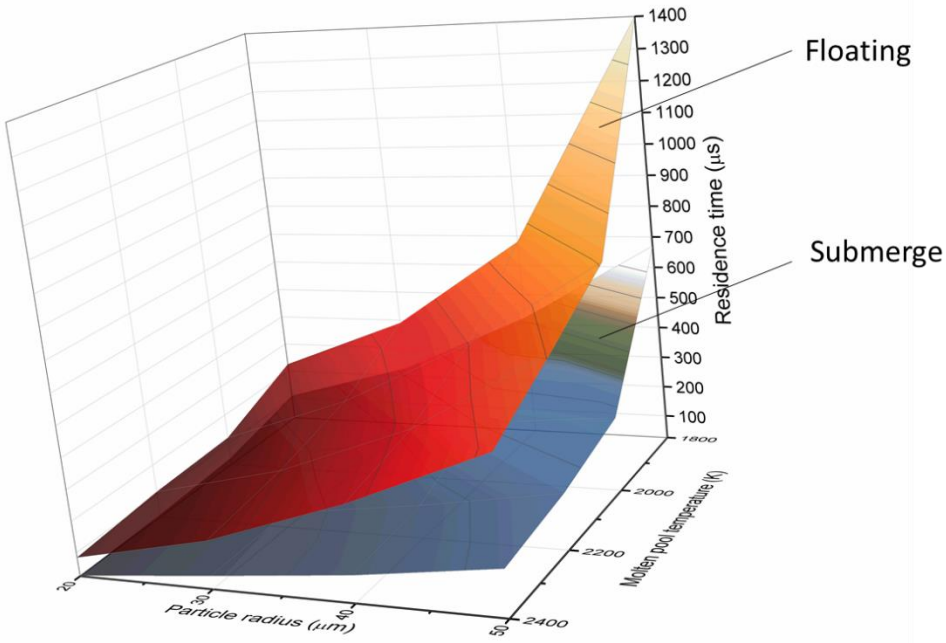

Figure 21. 3-D surface plot showing the calculation results for the influence of particle radius and molten pool temperatures on residence time for stainless steel, SS316.

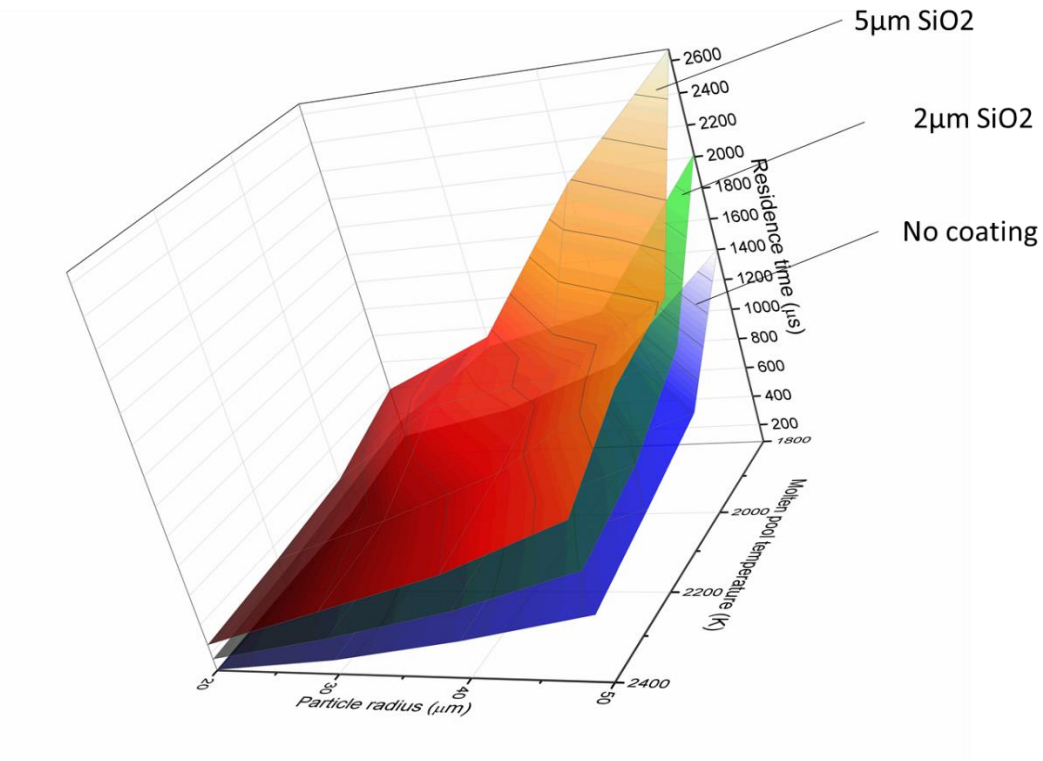

Figure 22. 3-D surface plot comparing particle residence time under for different coating thickness values.

3.2. Coated ZA-8 particle

Representative temperature and phase field sare shown in Figure 23 for coated ZA-8 particles for the floating regime, with a 5 µm Ni coating and a 50 µm particle diameter. The melting starts within 10 µs, and the liquid phase increases along with the heating. At t=76 µs the vaporization starts as the gas phase starts to form. The corresponding time to initiate vaporization is defined as particle residence time. This residence time is calculated for various particle radius, molten pool temperatures, coating thickness values and coating materials. The results are summarized in Table 4. An infinite residence time value represents when the particle does not experienced vaporization and therefore survives during the deposition. Figure 24 represents the calculation results in 3-D surface plots for different coating materials. The shaded regions

represent the parameter combinations that would result in infinite residence time, and furthermore correspond to the allowed process window to retain the ZA-8 particle in the deposited parts.

Figure 25a shows the effects of different particle radius on residence time. A Ni coating with a 1500 K molten pool temperature was assumed in this calculation. A slight increase in particle residence time was observed when the particle radius increased from 20 μm to 50 μm. The effect of coating thickness was found to be more significant than that of particle radius.

Table 5 summarized the calculated particle residence time values assuming 10 μm coating thickness when using various coating materials, and Figure 25b presents the effect of thermal diffusivity of the coating material on particle residence time. All assumed thermal diffusivity values are at room temperature. A significant increase in residence time was observed when using coating material with lower thermal diffusivity. When using SiO_2 as the coating material, the calculation shows that it is possible to use a coating thickness as thin as 10 μm to prevent boiling of the ZA-8 particle, given a sufficiently low molten pool temperature.

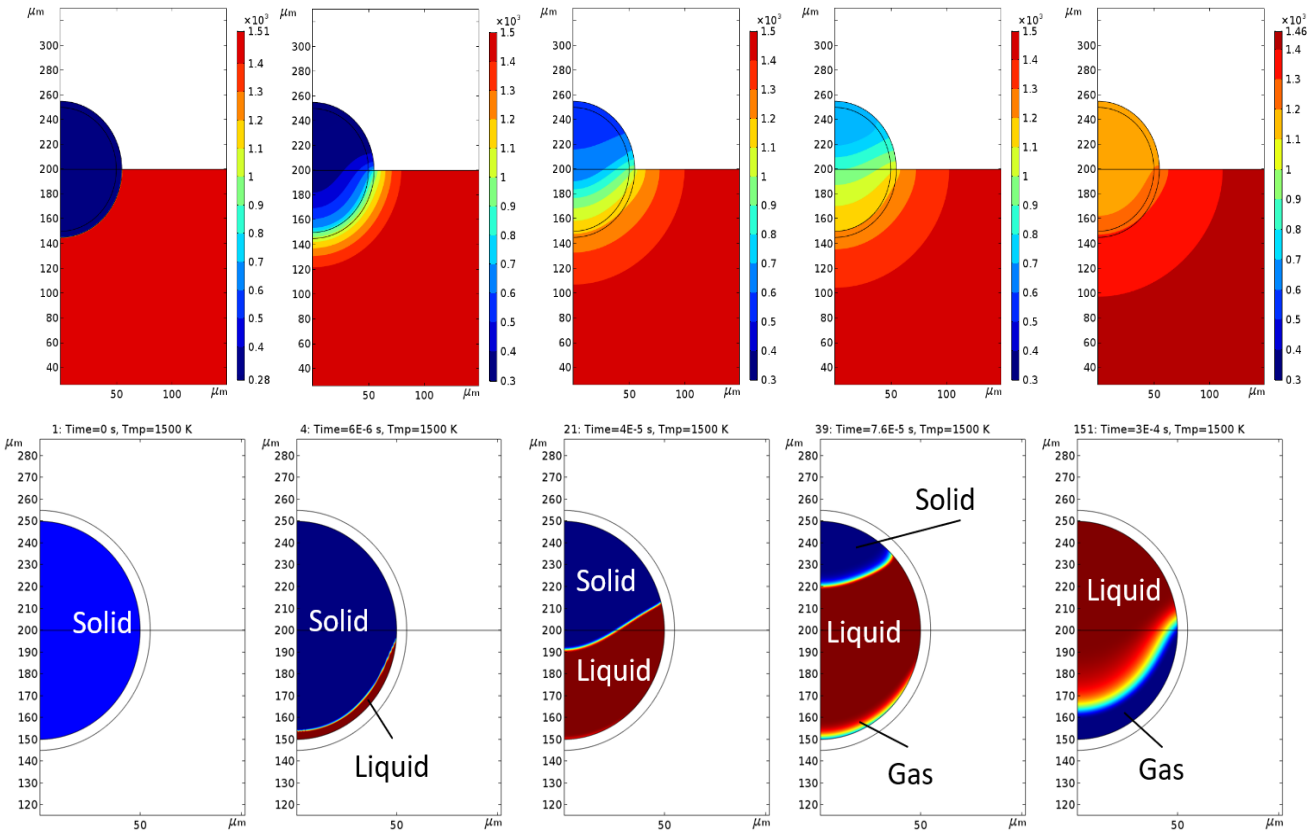

Figure 23. Representative temperature field (top row) and phase field (bottom row) for ZA-8 particle at different simulation times: (a) t=0; (b) t=6 μs; (c) t=40 μs; (d) t=76 μs; (e) t=300 μs.

Table 4. Summary of COMSOL calculated residence time results for coated ZA-8 particles.

	Molten pool temperature (K) / **Coating thickness (μm)**	**1300**	**1400**	**1500**	**1600**	**1700**		**1300**	**1400**	**1500**	**1600**	**1700**
Co coating	**5**	138(μs)	96	74	50	36	**Ni coating**	150	106	82	48	36
	10	176	134	112	84	64		186	130	110	86	52
	30	435	270	215	195	175		415	310	210	185	150
	50	775	525	425	350	300		725	500	375	300	250
	70	∞	775	600	475	425		∞	720	550	425	375
	100	∞	1150	900	825	700		∞	1025	750	575	500
Ti coating	**5**	188	130	112	74	48	**Al_2O_3 coating**	336	224	164	142	98
	10	276	158	144	124	96		594	414	318	249	204
	30	665	430	295	240	195		∞	∞	1190	970	810
	50	∞	750	525	400	325		∞	∞	3125	1975	1700
	70	∞	1250	775	600	500		∞	∞	∞	∞	3075
	100	∞	∞	1350	1050	825		∞	∞	∞	∞	∞

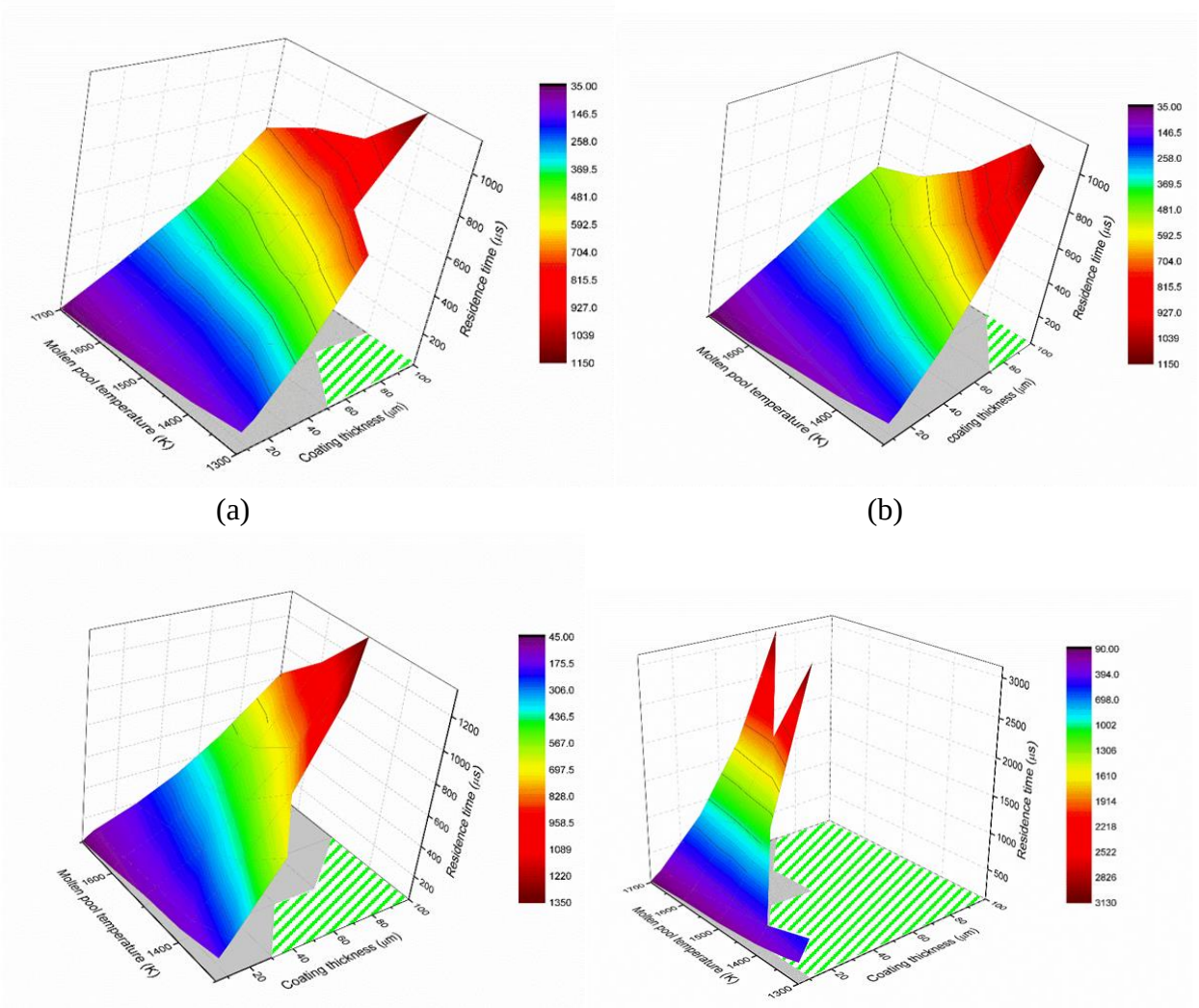

(a) (b)

(c) (d)

Figure 24. 3-D surface plot comparing ZA-8 particle residence time using various coating materials: (a) Co; (b) Ni; (c) Ti; (d) Al_2O_3. The shaded regions represent parameters that will result in infinitely long residence time.

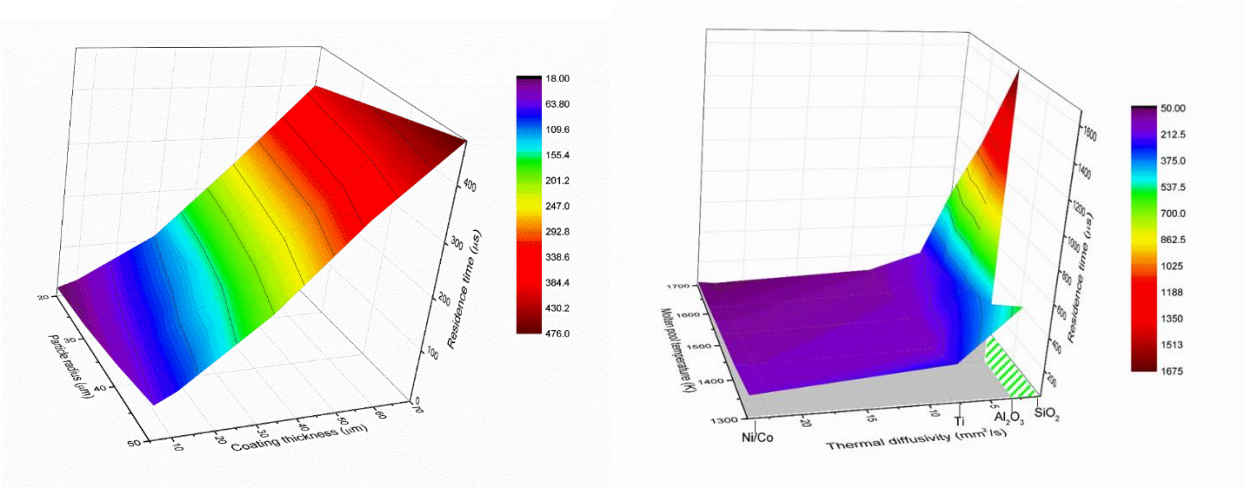

(a) (b)

Figure 25. (a) Calculated results for various ZA-8 particle radius values, assuming molten pool temperature of 1500 K and a Ni coating is used. (b) Calculated results for various coating thermal diffusivity values, assuming a coating thickness of 10 μm and a particle radius of 50 μm.

Table 5. Calculated particle residence time results assuming various coating materials.

Molten pool temperature (K) / **Coating materials**	**1300**	**1400**	**1500**	**1600**	**1700**	**Thermal diffusivity α (mm^2/s)** [64]
Co	176(μs)	134	112	84	64	24.1
Ni	186	130	110	86	52	22.5
Ti	276	158	144	124	96	8.08
Al_2O_3	594	414	318	249	204	3.25
SiO_2	∞	∞	1675	1100	625	0.739

3.4. Discussion

3.4.1 Factors that determine the residence time

The calculation results from this study revealed that the particle residence time is dependent on and sensitive to many parameters, including but not limited to: particle size, molten pool local temperature, coating thickness, particle material, coating material, particle capture mechanism etc. Due to these many variables, large deviations in residence time have been found, and are in

agreement with the high-speed video measurements from previous studies [7,58]. The residence time was found to be in positive correlation with particle radius and coating thickness, and in negative correlation with molten pool temperature and coating material thermal diffusivity. Unlike the assumption in the simulation, the temperature of the molten pool is not actually uniform and has a spatial distribution: with higher temperatures near the center where the laser spot is irradiating and lower near the periphery of the molten pool. Consequently, the particle would have a longer residence time if it landed on the region where the temperature is lower and possibly not fully melted. Unmelted particles in the final DED parts are commonly reported in the literature [65].

The contact angle of the particle and molten pool can also play an important role on particle residence time, since it determines the portion of the particle submerged into the molten pool. Figure 26 illustrates the scenarios for various contact angles and Figure 27 shows the COMSOL simulation results for different contact angles, assuming a SS316 particle with radius of 50 μm and molten pool temperature of 2200 K. The submergence regime is also shown for comparison. Since the contact surface area between the particle and the molten pool decreases with increasing contact angle, the conductive heat exchange rate will decrease and consequently result in a longer residence time. The contact angle is a function of surface tension energy between the boundary of the molten pool liquid and the particle, described by Young's equation [66]:

$$\gamma_{sv} - \gamma_{sl} = \gamma_{lv} cos\theta_e \tag{36}$$

where γ_{sv}, γ_{sl}, γ_{lv} are surface energy between solid-vapor, solid-liquid and liquid-vapor, respectively, and θ_e is the equilibrium contact angle. The surface energy decreases approximately linearly with increasing temperature, according to Eotvos equation [67]:

$$\gamma V^{\frac{2}{3}} = k(T_c - T) \tag{37}$$

where V is the molar volume of the liquid, k is the Eotvos constant and has a value of 2.1×10^{-7} J/(K·mol$^{2/3}$), T_c is the critical temperature. The resultant contact angle is also a function of temperature[68]:

$$cos\theta_e = C(T_c - T)^{\frac{a}{b-a}} + 1 \tag{38}$$

where C is a constant that determined by material properties, a and b are empirical parameters. In general, the contact angle remains mostly unchanged at low temperature, and decrease at medium to high temperature [68]. Larger contact angles have been observed from the high-speed videos for molten pools with lower laser power (shown in Figure 28), indicating the molten pool temperature has significant effect on particle contact angle. Significantly longer residence time has also been observed as a result.

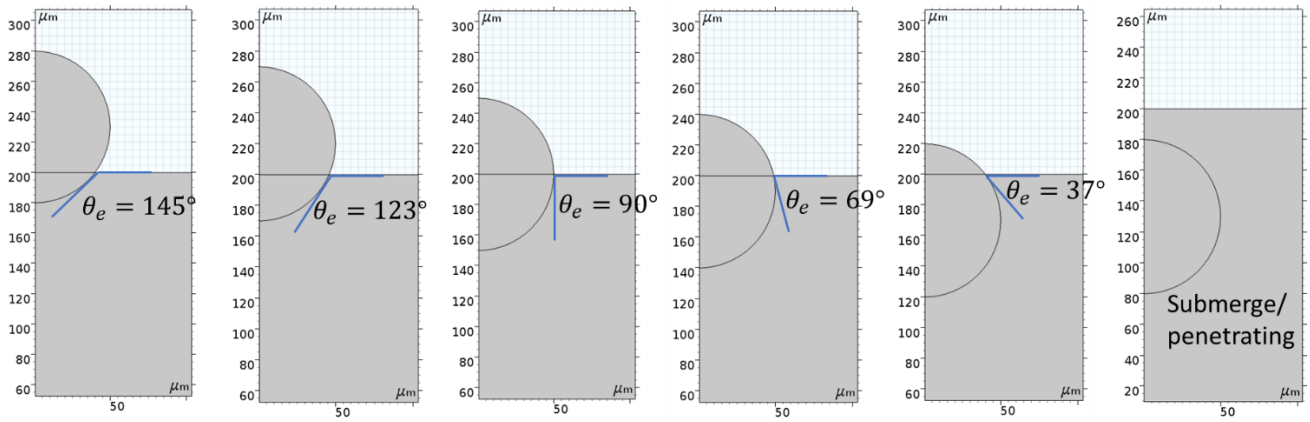

Figure 26. Schematic representation of COMSOL models assuming different particle contact angles. Submergence regime is also shown for comparison.

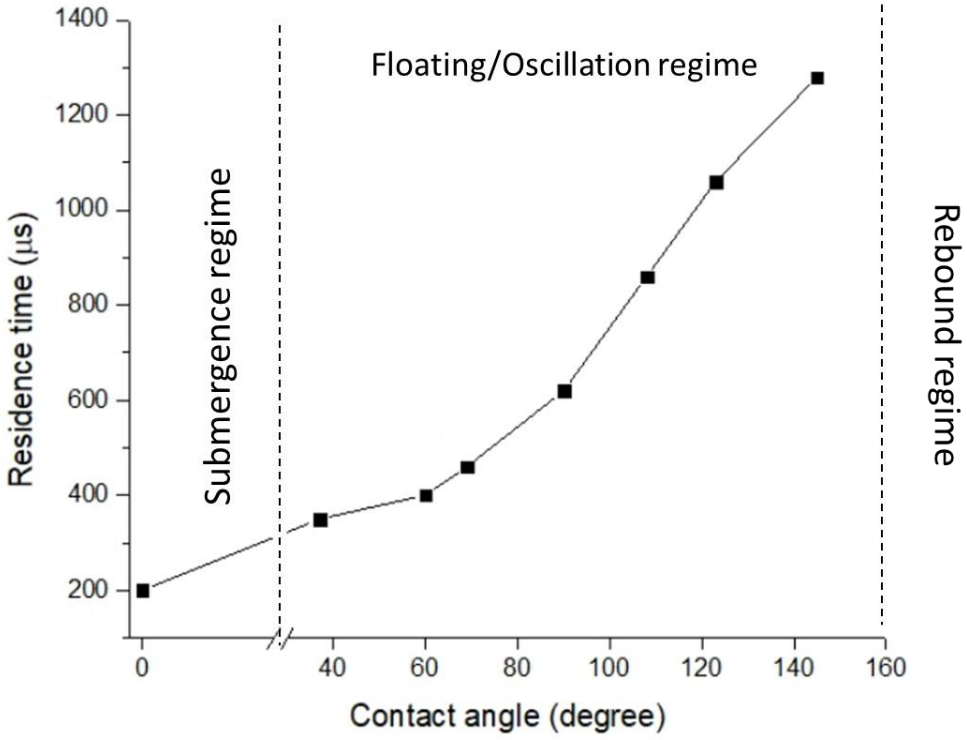

Figure 27. Calculation results for particle residence time assuming different contact angles.

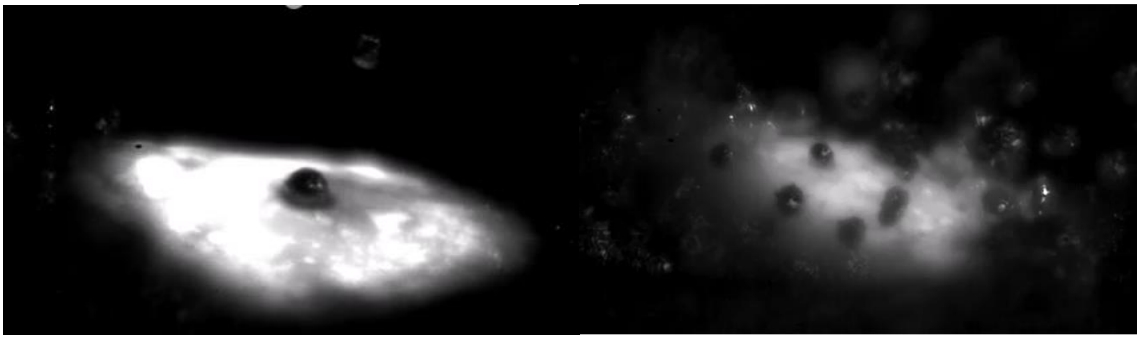

(a) (b)

Figure 28. Snapshots from high-speed videos for molten pools using different laser parameters: (a) 600W, 10 mm/s; (b) 400W, 10 mm/s. Larger contact angle and significantly longer residence time were observed when lower laser power has been used.

3.4.2 Material and parameter selection for retaining ZA-8 particle

As discussed in the above sections, the particle residence time is dependent on particle size, molten pool temperature, coating thickness and coating material. In the application of self-healing materials, it is desired to retain the ZA-8 particle in the deposited parts. Therefore, longer residence

time is desired. This means that coating materials and laser parameters need to be carefully selected in order to achieve this goal. The COMSOL model results suggested that the thermal diffusivity of the coating material has a significant effect on particle residence time (as shown in Figure 25b). When metallic coatings (Ni, Co, Ti) with relatively higher thermal diffusivity were used, the coating would need to be more than 30 μm thick to prevent the ZA-8 particle from boiling. The metallic coatings do not act as good thermal barriers in these scenarios due to their high thermal diffusivity. By contrast, when using low thermal diffusivity ceramics as the coating material, such as Al_2O_3 and SiO_2, the required coating thickness is much reduced. Calculation shows that a coating thickness of less than 10 μm would lead to infinite long residence time, i.e., the criterion to retaining the particle, given a low enough molten pool temperature. Therefore, from solely a heat transfer perspective, it is recommended to use SiO_2 as coating material to retaining the ZA-8 particle.

3.5. Summary

Phase and heat transfer models has been constructed in COMSOL Multiphysics to calculate coated particle residence time in the molten pool during the DED process. Various parameters including molten pool temperature, coating thickness, particle size, coating materials and contact angles have been evaluated. The following key findings are listed below:

- The residence time was found to be 27-1400 μs for uncoated SS316 particle. A large range of residence time was estimated.
- The residence time was found to be in positive correlation with particle radius and coating thickness, and in negative correlation with molten pool temperature and coating material thermal diffusivity.

- Contact angle was found to influence the particle residence time due to the variation in thermal contact surface area. Submergence regime is found to lead to longer residence time than for the floating regime.
- The coating material has significant influence on residence time. SiO_2, due to its extremely low thermal diffusivity, could lead to a large increase in residence time and therefore is recommended for use to retain the ZA-8 self-healing particle.

Chapter 4: Numerical Simulations of Thermal History in Additive Manufactured Parts

4.1. Introduction

In laser based additive manufacturing, it is a common practice to rotate the deposition hatch pattern by a fixed angle between deposited layers, to minimize empty space (i.e., minimize lack of fusion (LoF) defects) and promotes microstructure and property homogeneity. A hatch rotation angle of 105° between layers has been reported to most effectively eliminate LoF related to surface corrugation, thereby increasing the density of deposits [69]. Furthermore, mechanical testing of powder bed fusion (PBF) 304 stainless steel (SS) structures fabricated with many different hatch rotation angles showed a 105° hatch rotation angle improved mechanical properties [70]. It was hypothesized, but not demonstrated, that the greater number of layers between identical scanning directions increased the randomness of the microstructure by repeatedly altering the directionality of heat flow, thus altering the direction of preferred grain orientation during solidification [70,71].

Numerous analytical and numerical models that have been developed to understand and predict the heat transfer mechanisms and thermal history during DED processes provide the foundation for the computational simulation aspect of the current study. For instance, the well-known Rosenthal's solution set the groundwork for DED simulation by solving for the temperature field that results from a moving point heat source [11]. Peyre et al.[72] established a COMSOL® finite element method (FEM) model that simulates heat conduction for a single wall deposition using the quiet element method, where the entire structure geometry is included in the simulation with the elements not yet deposited assigned void material properties. This FEM method successfully predicted wall morphology and thermal conductivity. Zheng et al. [2] used an alternate-direction explicit (ADE) finite difference method (FDM) numerical simulation to solve

the thermal history of a 20-layer single wall build, utilizing the computational simplicity to validate experimental observations. Roberts et al. [73] built a three-dimensional FEM model to simulate thermal history of a five-layer parallel deposition during the PBF process.

In this study, a FEM heat transfer model was constructed in COMSOL® Multi-physics software to simulate the thermal histories resulted from laser scanning during the DED process. 0° and 90° hatch rotation angle deposition scenarios were considered, in which differences in temperature field and heat flux were compared. The calculation results were also used to validate crystallographic orientation and further correlated toe compressive mechanical properties to elucidate how hatch rotation angle influences structure-property relationships in as-deposited SS 316L samples.

4.2. Numerical model methodologies

The deposition model was designed to mimic the actual depositions while minimizing processing time. Figure 29 shows the mesh of the COMSOL model and illustration of laser scan direction for 0° and 90° hatch rotation angle. The builds were simulated as 4 mm×4 mm x 3 mm cubes with ten layers and ten tracks in each layer. The laser scan speed was 4 mm/s with 1 s for each track, thus the time duration for each layer was 10 s and total deposition time was 100 s. The laser scans in a serpentine pattern within each layer to replicate the actual LENS® deposition. The bottom surface of the substrate was assumed to have a constant temperature, T_s=300K which equals to the ambient temperature. The rest of the surfaces were assumed to be thermally insulated. The temperature field were calculated by solving the transient conductive heat flow equations in three dimensions:

$$\rho \cdot C_p \cdot \frac{\partial T}{\partial \mathrm{t}} + \rho \cdot C_p \cdot v \cdot \nabla T - \nabla(k \cdot \nabla T) = Q \tag{39}$$

where ρ, Cp, k are the density, specific heat and thermal conductivity of the 316L SS, respectively; v (m/s) is laser scan speed, and Q (w/m^2) is the heat source from the laser beam.

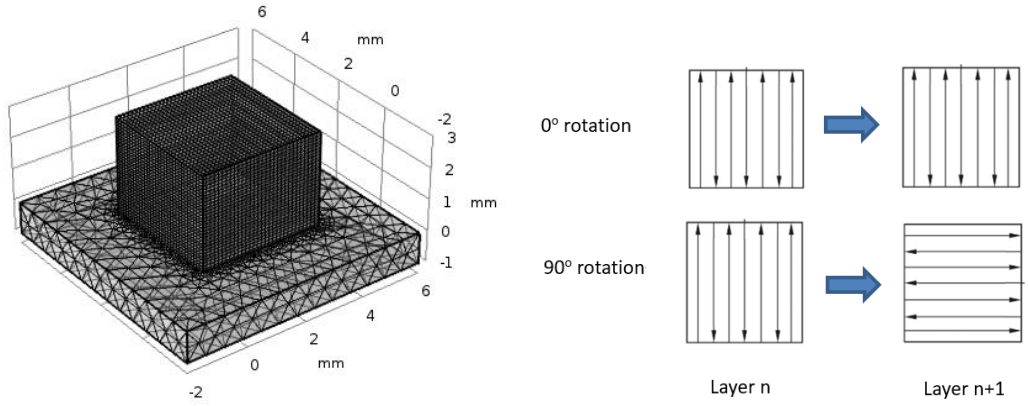

Figure 29. (a) Geometry and mesh for COMSOL model (b) illustration of laser scan strategies for adopting 0° and 90° hatch rotation angles.

To simulate mass generation and accumulation during the deposition process, analytical expressions are used to describe the thermal conductivity (k), density (ρ) and heat capacity (Cp) as functions of time (t) and position (x,y,z). The algorithm is set up such that when the laser spot moves to a certain point in the cube, thermal properties (k, ρ, Cp) of the material are switched from those of argon to the metal. This quiet element method is similar to the one described in [72], but differs in that the desired geometry is a 3-dimensional cube instead of a single wall. Expressions below demonstrate the thermal properties used as functions of x,y,z and t:

For 0 degrees:

$$M(x,y,z,t) = M_{Inconel} \cdot step[H\big((zpos(t)+d-z)\big) \cdot H\left(\left((ypos(t)-y)\cdot(-1)^{osl(t)}+d\right)+ 10\big(z<(zpos(t)-d)\big)+10(x<xpos(t)-w)\right)\cdot H\big((xpos(t)+w-x)\big)+ 10\big(z<(zpos(t)-d)\big)] \quad (40)$$

For 90 degrees:

$$M(x,y,z,t) = M_{Inconel} \cdot step[H\big((zpos(t) + d - z)\big)$$

$$\cdot H\left[\left((ypos(t) + osl(t+10)\cdot w - y)\big((-1)^{osl(t)}\big)^{osl(t)} + d \cdot osl(t)\right)\right.$$

$$\left. + 10(z < zpos(t) - d) + 10 \cdot osl(t)(x < xpos(t) - w)\right)$$

$$\cdot H\left(\big((xpos(t) + osl(t)w - x)\big)\big((-1)^{osl(t)}\big)^{osl(t+10)} + d \cdot osl(t+10)\right.$$

$$\left. + osl(t+10) * 10\big(y < (ypos(t) - w)\big) + 10\big(z < (zpos(t) - d)\big)\right)]$$

(41)

where M represents the material's thermal properties which can be substitute by k, Cp or ρ; d is the layer thickness and w is the track spacing. H is the Heaviside step function. Functions xpos(t), ypos(t) and zpos(t) represents the x, y, z positions of the laser spot as a function of t, respectively. The osl(t) is an oscillation function to produce the serpentine mass accumulation pattern.

4.3. Results

4.3.1 Thermal histories for different hatch rotation angles

Figure 30 compares the COMSOL results for the thermal history of point P, located in the middle of the edge of the first layer of the build, for hatch rotation angles of 0° and 90° hatch rotation angle. The simulation results show that the deposited material will experience different periodic reheating and cooling with different hatch rotation angles. The reheating occurs from both the nearby tracks within the same layer as well as the tracks directly above point P in subsequent layers. When the laser passes through point P at t=0.5 s, the material temperature rapidly increases, which results in a temperature peak for both scenarios. The material then cools as the laser moves

away from the point. Because the laser scans in a serpentine pattern in each layer, point P will be reheated with each subsequent laser deposition track in the first layer, as shown by the periodic temperature spikes in Figure 30 (a) and 30 (b) for times 0–10 s. The laser scan directions are identical in subsequent layers for the 0° hatch, but are traversed at an increasing distance from the initial point P. For example, at t=10.5 s the laser spot is located at the same horizontal xy position but one layer higher in the vertical z direction and the temperature of point P suddenly increases. This temperature pattern repeats every 10 s with decreased maximum temperature as the laser moves farther away accompanied by an increase in minimum temperature due to heat accumulation in the build. For the 90° hatch, the initial point P will be traversed at different time intervals with subsequent layers due to the rotation of the hatch pattern. The effect on thermal history is apparent during the time period between 10 and 20 s in Figure. 30 (c), where the material experiences two reheats within a very short time duration in the middle of the 10 s window that causes a “double peak” in the temperature plot when t=14–16 s. The repetition of these different temperature profiles is representative of the difference in thermal history experienced by the deposited materials in the 0° build and 90° build.

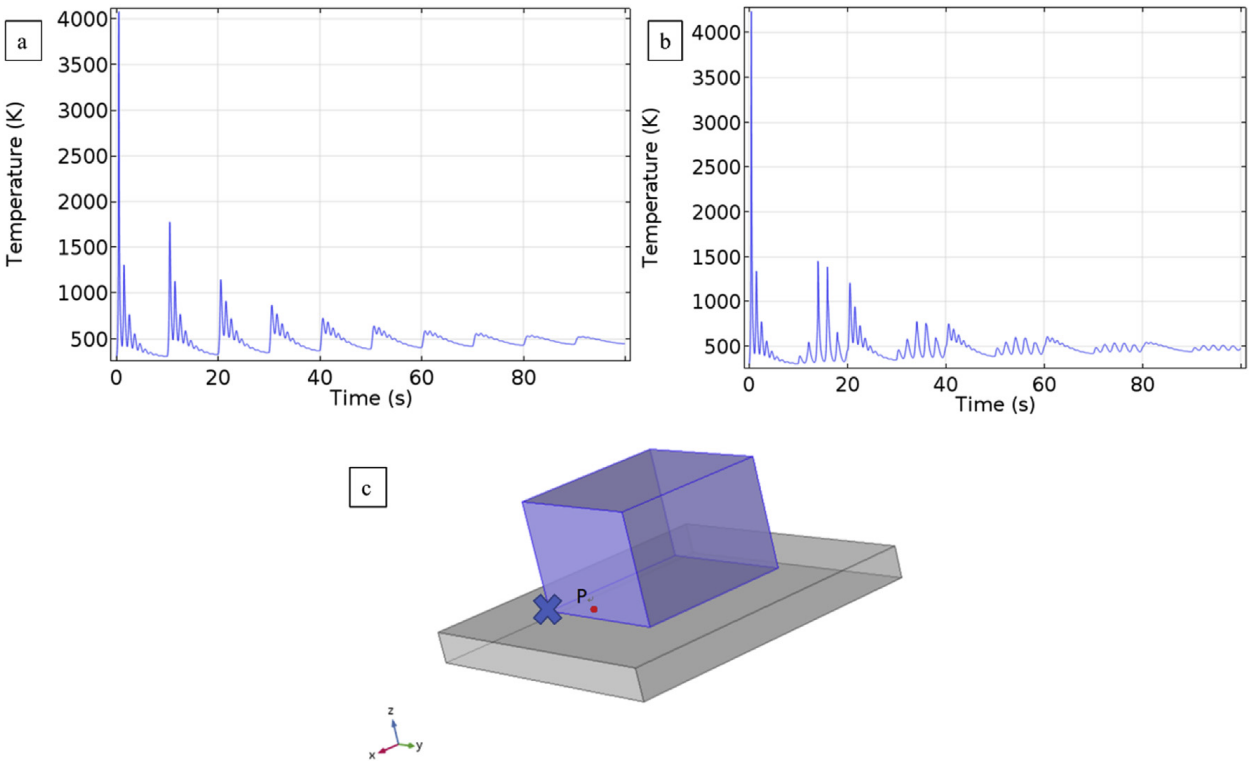

Figure 30. Simulated temperature history for (a) a 0° build and (b) a 90° build. (c) Geometry of the substrate (gray) and build (blue) in COMSOL model with a red dot representing the point of interest, P, for thermal history. The time to deposit one layer is 10 s. Laser scanning begins from the 'x' at the left-front bottom corner and moves in the positive y direction.

There is evidence that during the LENS® deposition process, it may take several tracks or even several layers for the system to reach a quasi-steady state in terms of mass capture, temperature history and energy balance [9]. This can be supported from the change of the peak temperature for each track in the first layer, plotted in Figure 30a. The peak temperature for the first track is 4132K, the highest among all the tracks in first layer, and then drops significantly for the second (3464K) and the third track (3320K). After the third track the peak temperature stabilized at around 3300K and appeared gradually increasing until the last track due to the heat accumulation on the substrate. The first track has the highest peak temperature, which can be explained by the geometry of the deposited tracks. Figure 31b and c show a schematic geometry

of the deposited first track and first ten (10) tracks. The deposited first track is surrounded by inert gas such as argon, acting as a thermal insulator whose thermal conductivity is usually very low compared with that of alloys. As such, most of the heat can only be conducted down vertically through the metal substrate. In contrast, when there is already deposited metal next to the current depositing track, heat can be dissipated parallel into the previously deposited tracks, which are metallic alloys with much higher thermal conductivity. Therefore, the peak temperature for the first track tends to be higher than the proceeding tracks due to the thermal insulation of the surrounding inert gas. The deposited tracks will also cause the molten pool to be asymmetric because of the huge difference in thermal conductivity between the metal alloy and inter gas. Heat flux near the molten pool and molten pool asymmetry are further explained in the next section.

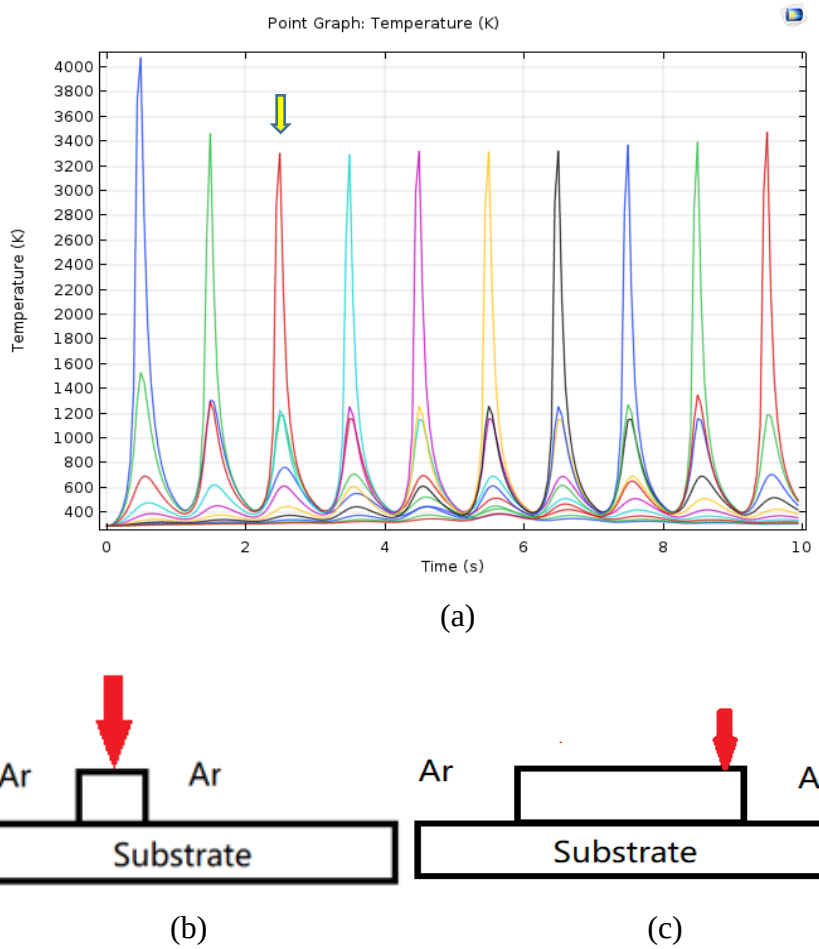

Figure 31. (a) Temperature profiles for each track in the first layer. The peak temperature starts to stabilize after the third track, highlighted by the yellow arrow. (b) Schematic representation of the geometry after the deposition of the first track and (c) after the 10th track. Red arrows represent the laser position.

4.3.2 Heat flux and effects on microstructures

Figure 32 a, b, and c show the temperature field and heat flux near the laser beam center for 1st, 5th and 9th layer respectively, for the 90-degree rotation build. The red arrows represent the magnitude and direction of the heat flux. The bolded circles represent T=1700K temperature contour, which corresponds to the melting temperature of the SS316L. The asymmetric shape of the temperature contours and the molten pools, which differ from welding literatures, are seen because during the laser additive manufacturing process, the previously deposited track will affect

the transient temperature distribution, heat flow, fluid flow and molten pool geometry of the adjacent track. During the LENS® deposition, heat is accumulating in both substrate and deposited material, causing the rise of the material temperature, as shown in Figure 33. Consequently, the molten pool size and maximum temperature will increase as the deposition proceeds to a higher layer. Figure 33 represents the increasing trend of molten pool area and maximum temperature from layer 1 through 10. The increasing molten pool size would result in more powder being captured and potentially affects the geometric consistency of the final build parts.

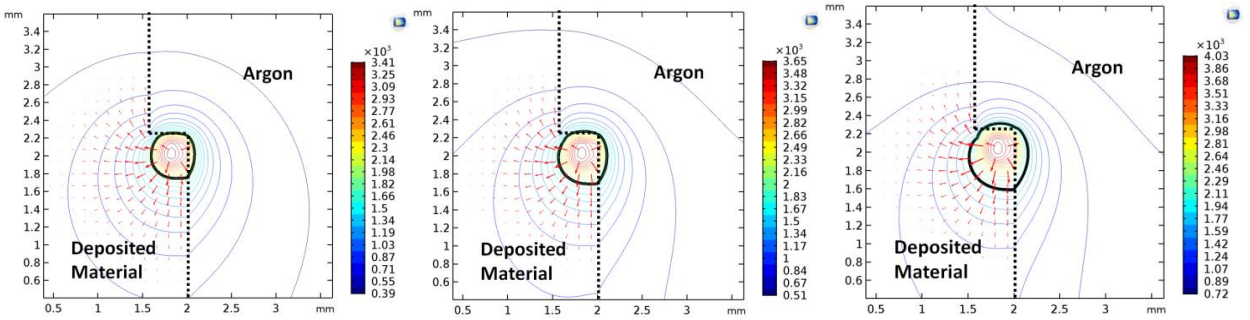

(a) (b) (c)

Figure 32. Temperature field and heat flux near the molten pool for 90-degree rotation (a) 1st layer; (b) 5th layer and (c) 10th layer. Black contours represent the molten pool boundaries derived from the temperature contours.

Figure 34a and b show the simulated temperature contour and heat flux field underneath the molten pool for hatch rotation angles of 0° and 90°, respectively, at the point of interest indicated by the 'x' in Figure. 34 (c). The 'x' is at the mid-point of the first track in the fourth layer for the 0° hatch, and at the starting point of the fourth track in the fourth layer for the 90° hatch. The red arrows in Figure. 34 (a) and (b) represent the magnitude and direction of heat flux. In the 0° parallel hatched build the laser is scanning in the positive y direction, toward the right side of the plot. In the 90° cross-hatched build, the laser is scanning in the positive x direction, i.e., pointing into the page. Since the grain growth direction is inversely parallel to the heat flow direction, adopting 0° parallel scan strategy preferred epitaxial growth, as illustrated in Figure 34.

Because there is no layer wise rotation of the heat flux, the parallel hatch pattern produces predisposition to similar preferred orientations and could potentially results in grain elongation across multiple layers. By contrast, the heat flux adopting 90° cross-hatched strategy results in significant layer-wise deviations between the preferred cellular growth directions in subsequent layers, which reduces the proclivity for preferred grain directions and directional elongation.

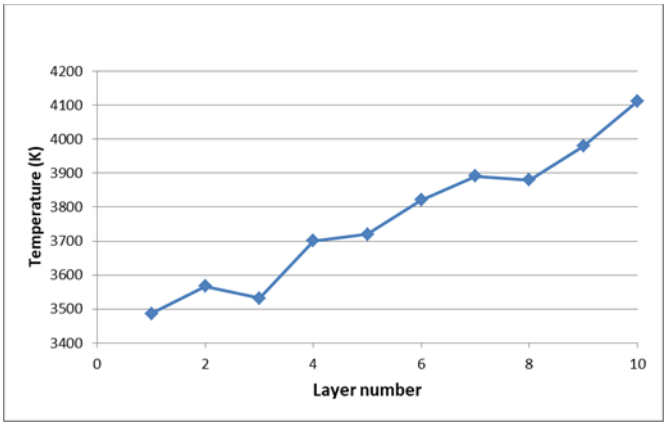

Figure 33. Peak molten pool temperature at different layers.

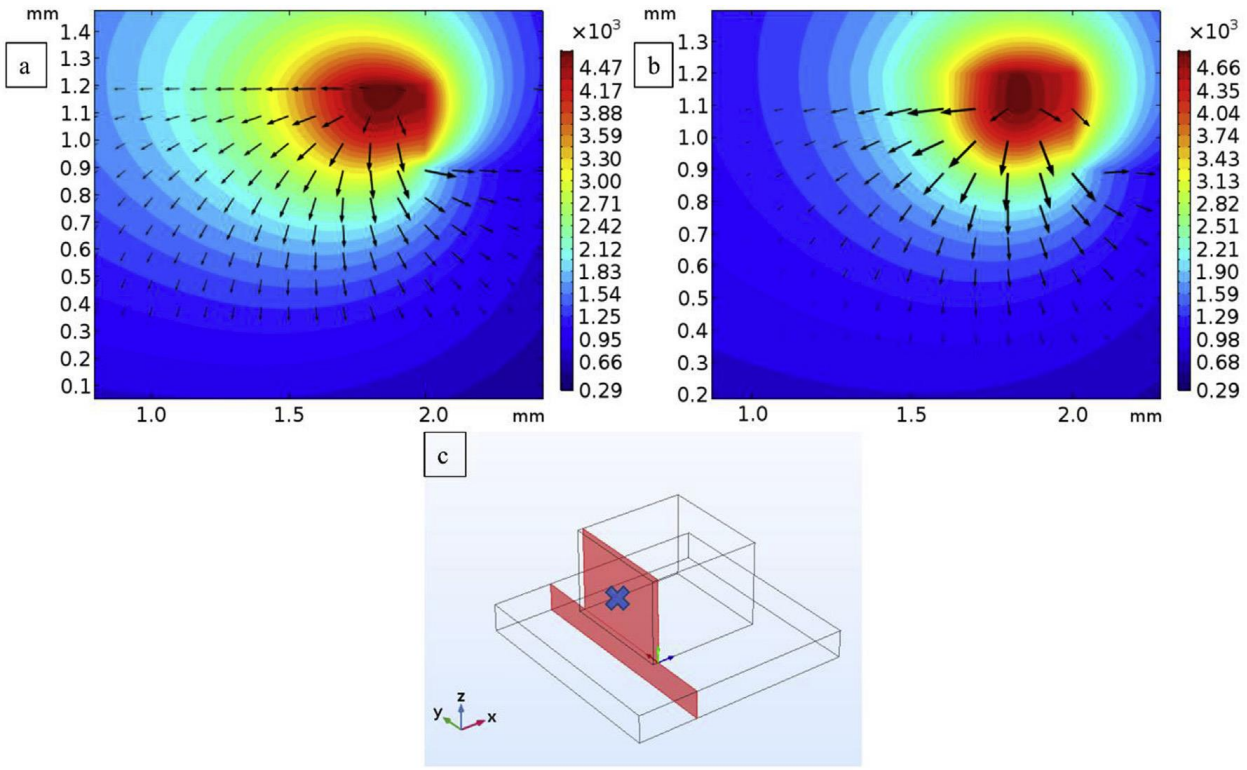

Figure 34. Simulated temperature field (contour lines) and heat flux (red arrows) of (a) a 0° build and (b) a 90° build (c) Cut plane of the simulated heat flux plot with the laser at point 'x'.

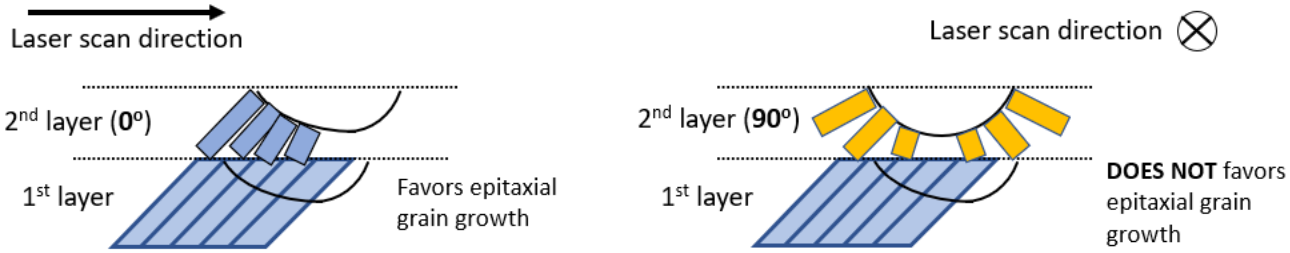

Figure 35. Illustration of preferred grain growth direction as a result of the heat flux. (a) 0° rotation angle (b) 90° rotation angle.

4.3.3 Feature dimensional effects

Parts geometries and feature thickness can have significant influence on heat transfer and thermal histories. To address this issue, the above model was modified to have different leg thickness: 0.5, 2.5 and 5.0 mm, as represented in Figure 36. The finer meshed regions were assigned to the features scanned by the laser beam, while the coarser meshed regions were assumed

to have thermal conductivity of 0.01 times that of the bulk SS 316L alloy, representing the powder bed surrounding the deposited build. Rectangular elements with maximum size of 0.03 mm were used for the central finer meshed region and free tetrahedral elements with maximum size of 0.28 mm were used for the rest coarser regions. The simulations were performed for the entire 100th layer (2 mm away from the substrate), with laser parameters listed in table 6 for all three leg thickness values.

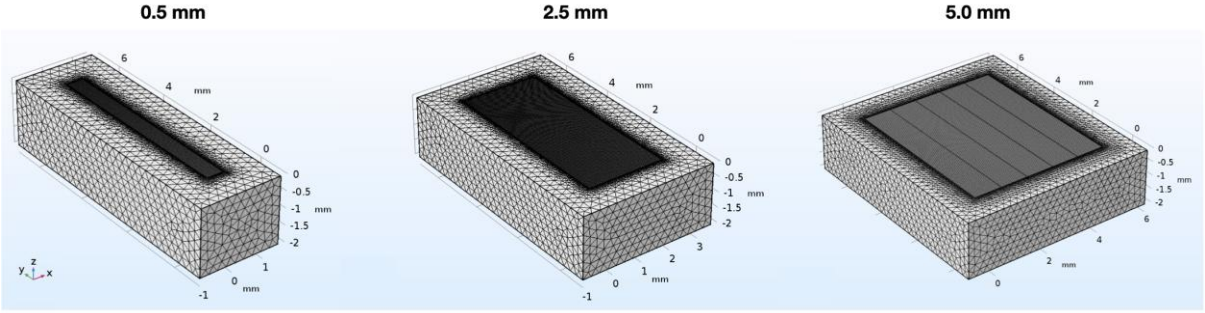

Figure 36. Meshed geometries for finite element analysis (FEA) of heat flow within features of different thicknesses.

Table 6. Laser powder bed fusion (LPBF) process parameters used for sample fabrication. The calculated value for volumetric energy density is also provided.

Sample ID	Laser power (W)	Scan speed (mm/s)	Hatch spacing (mm)	Layer thickness (mm)	Volumetric energy density (J/mm^3)
B120	195	800	0.10	0.02	122
B200	370	2520	0.04	0.02	196

The calculated molten pool peak temperature and dimensions for the three leg thickness values, derived from the 1600 K isotherm that corresponds to the melting point of SS 316, are plotted in Figure 37. Since the thicker feature thickness will prefer the heat to conducting sideways, the consequences are that both the molten pool dimensions and peak temperature decreased for

increasing feature thickness. The width of the molten pool dropped from 122 μm for 0.5 mm leg to 104 μm for 5 mm leg, while the molten pool depth slightly decreased from 43 μm for 0.5 mm leg to 38 μm for 5 mm leg. The peak temperature reduced from 2760 K for 0.5 mm leg to 2540 K for 5 mm leg. The thermal gradient and the cooling rate also seen decreased values for thicker feature. The estimated thermal gradients were 3.4×10^7 K/m, 3.0×10^7 K/m, 2.2×10^7 K/m for 0.5, 2.5 and 5 mm leg thickness, respectively, and the cooling rates were 7.0×10^5 K/s, 6.5×10^5 K/s, 4.4×10^5 K/s for 0.5, 2.5 and 5 mm leg thickness, respectively.

The effects of feature dimensions on microstructural evolution, phase composition and mechanical properties of the additive manufactured parts have been studied from previous works for various materials, including stainless steels 316L [74], 304L [75], Ti-6Al-4V [76,77] , Inconel 625 [78]and AlSi10Mg [79]. Although a clear relationship has yet to established, some researchers have found an increase in yield strength and ultimate tensile strength for increased sample thickness, attributed to the surface toughness and defects. However, based on the simulation results in this study, the lower cooling rate found in 5 mm feature thickness should favor the finer grains which, according to the Hall-Petch relationship, promotes higher yield strength. This suggests that other factors, such as solidification rate [80] or temperature gradient [81] could also influence the grain growth in the as-deposited samples. More thorough experimental works are needed to further explain and understand the relationship between feature dimension and build properties.

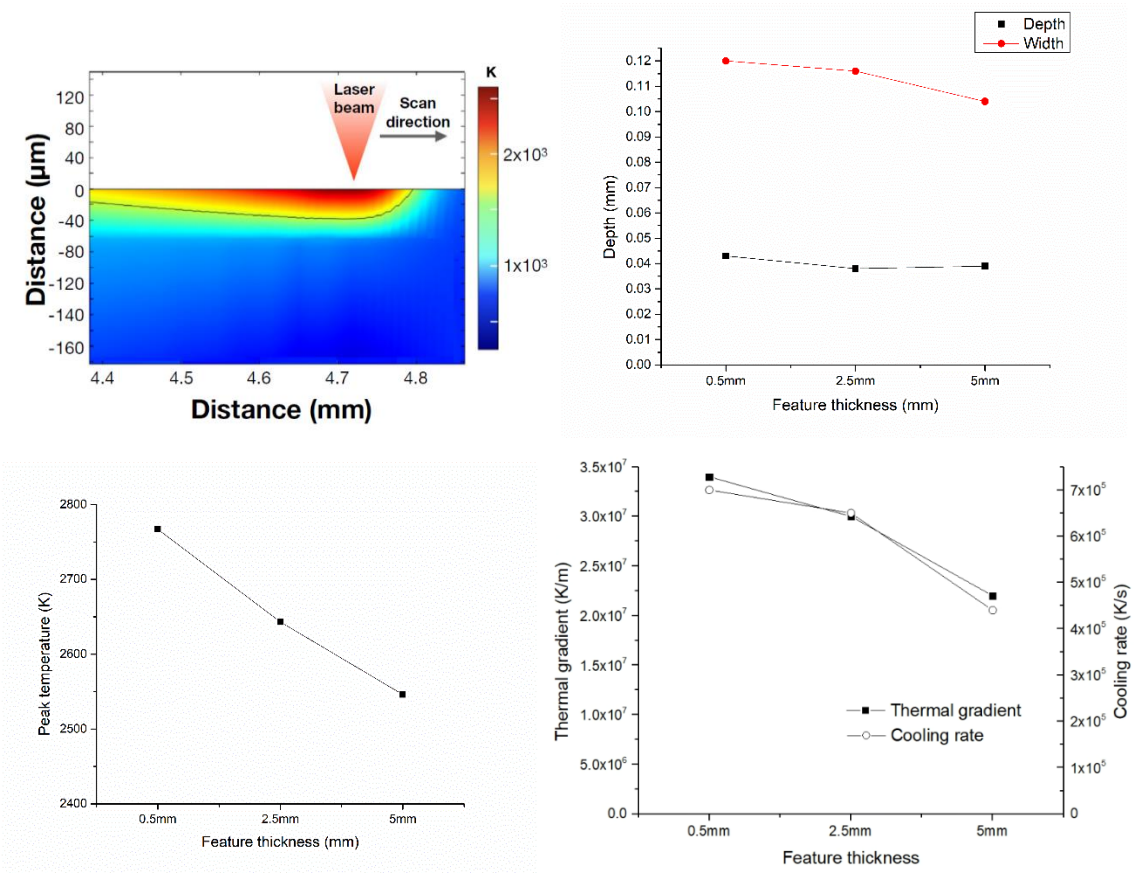

Figure 37. Calculated temperature field and molten pool shape (a) and effect of feature thickness on: (b) molten pool depth; (c) molten pool peak temperature and (d) thermal gradient.

4.4. Summary

3-D heat transfer models were constructed in COMSOL® Multiphysics software. Temperature fields, thermal histories, temperature gradient and cooling rate were calculated and compared for different hatch rotation angles and feature thicknesses. Distinct thermal histories were found for 0 and 90 degree hatch rotation angles. Adopting 90 degree hatch rotation angle results in more randomized thermal history. 0 degree hatch rotation angle favors epitaxial grain growth due to the similar heat flux direction to the predeposited layers.Feature dimension was found to influences the molten pool sizes, molten pool temperature, thermal gradients and cooling rate. Increased feature thickness results in decreased molten pool dimension, peak temperature and cooling rates.

Chapter 5: Role of Nb on Phase Evolution of Ni-based Metal Matrix Composites Fabricated via Directed Energy Deposition (DED)

5.1. Introduction

Nickel-based superalloys, such as those in the Inconel and Haynes series, are widely used in aerospace, chemical and marine applications due to their high melting temperatures, excellent oxidation resistance, and high creep strength and stability [82]. Incorporation of ceramic particles such as TiC, WC and SiC into nickel-based superalloys to form particle-reinforced metallic matrix composites (MMCs) can further modify their mechanical behavior, including strength, hardness and wear resistance [23,83,84]. Inspection of the published literature shows that the conventional liquid stir casting method is typically used to synthesize particle reinforced MMCs [20,24]. However, agglomeration of the reinforcement particles and poor wettability between the reinforcement ceramic particles and the metallic matrix commonly occur, which leads to deleterious effects on fracture toughness and fatigue life [19]. Moreover, post-processing and machining of the as-cast MMCs present formidable challenges due to their high hardness and wear resistance attributes, frequently rendering this processing approach prohibitively expensive [20]. Laser Engineered Net Shaping (LENS®), one of the widely adopted laser-based directed energy deposition (DED) additive manufacturing techniques, can effectively overcome the challenges of processing particle reinforced MMCs. The technique allows for the fabrication of metallic parts with complex geometries by implementing computer aided design (CAD) files. The layer-by-layer additive material deposition allows for the synthesis of parts with complex geometries and eliminates the need for post-processing and tooling [18–20]. The temperature at the center of the laser beam can reach as high as 3500 K, which is higher than the melting points of many ceramic

powders such as TiC and WC [9]. Many types of alloy systems and ceramic materials have reportedly been deposited successfully utilizing DED, including Ti6Al4V + TiC [23,85], Inconel 625 + TiC [52,86], stainless steel + WC [87] and AlSi10Mg + SiC [21]. While some of these previous results have been encouraging, there are also issues that remain, such as the presence of lack-of-fusion pores and cracks, as well as the decohesion of ceramic/matrix interfaces and the formation of undesired metallurgical phases [16,88]. These challenges provide an opportunity to further explore the underlying fundamental phenomena that drive phase formation and mechanical behavior.

Inconel 718 is a high-strength, corrosion-resistant nickel-based superalloy that has been extensively studied as a potential material for a wide range of high temperature applications [89]. It is strengthened by both gamma prime (γ', $Ni_3(Al,Ti)$, ordered face centered cubic, FCC) and gamma double prime (γ'', Ni_3Nb, ordered body centered tetragonal, BCT) precipitate phases, obtained through proper heat treatment and aging [90]. Haynes 282, on the other hand, is a relatively newly developed, γ' strengthened nickel-based superalloy that exhibits excellent creep strength and thermal stability as well as better weldability [91]. Although investigators have previously studied both alloys and their corresponding MMCs via laser-based additive manufacturing, the beneficial precipitation strengthening phase (i.e., γ' and/or γ'') is usually not observed in the as-deposited samples, likely due to the rapid cooling and solidification process that occurs during deposition [22,89,90,92–95]. In some studies, detrimental topologically close-packed (TCP) phases, such as Laves phases, have been observed in the as-deposited samples due to severe elemental segregation upon solidification, which may negatively impact mechanical behavior [96,97]. Furthermore, the phase formation that occurs when ceramic particles are introduced into the alloy matrix leads to additional complexities. The effect of ceramic particle

content on the microstructural evolution and phase formation needs to be carefully addressed for superior alloy design and adaptation of the DED manufacturing technique to MMC manufacturing.

In this work, DED was used to fabricate Inconel 718/TiC and Haynes 282/TiC particle reinforced MMCs with variable TiC content. The resultant microstructures were characterized and compared for the two composites to determine the differences in phase formation during DED. The mechanical behavior of as-deposited samples was analyzed through tensile tests and observation of the fracture surfaces. The influence of TiC content on phase formation in the as-built samples were predicted using Scheil solidification calculations within CALculated PHAse Diagram (CALPHAD) thermodynamic calculation software, Thermo-Calc.

5.2. Materials and Methods

The powder feedstocks used are gas atomized Inconel 718 and Haynes 282 powder (Praxair, 45 - 125 μm), and TiC powder (Advanced Powder Solutions, 25 - 45 μm). The chemical compositions (provided by the supplier) for the two alloys are listed in Table 7. The nickel alloy powder and TiC powder were blended in a V-blender for 1 hour before feeding the blended powder into the LENS® machine. Figure 38 shows a representative scanning electron micrograph of the blended powder mixture. Samples containing Inconel 718 and Haynes 282 with 0, 5, and 10 wt% of TiC (hereafter referred as IN-0 and HA-0, IN-5 and HA-5, and IN-10 and HA-10, respectively) were deposited using a LENS® 750 system (Optomec Inc., New Mexico, USA), with laser power of 300 W and scan speed of 16.7 mm/s for all samples. A representative photo of an as-deposited sample is provided in Figure 39. The dimensions for pure alloy samples were 14 x 14 x 40 mm and for composite samples were 10 x 10 x 40 mm. The as-deposited samples were sectioned along the vertical direction by electrical discharging machining (EDM) for tensile test coupons and

microscopic examination. The tensile specimens were prepared with 10 mm gauge length, 2.5 mm width and 1.5 mm thickness. The tensile tests were conducted using an Instron 8801 load frame with a 100 kN load cell and video extensometer to measure strain. Tensile specimens were prepared such that the build direction was oriented along the length of the gauge section. Several tests were conducted per sample with a nominal strain rate of $1x10^{-3}$ s^{-1}.

Table 7. Chemical composition of Inconel 718 and Haynes 282 alloys (wt%)

	Ni	Cr	Co	Mo	Nb	Ti	Al	Fe	Mn	C	Si
Inconel 718	55	17	1	3.0	5.5	1.15	0.8	15	0.35	0.08	0.35
Haynes 282	57	20	10	8.5	-	2.1	1.5	1.5	0.3	0.06	0.15

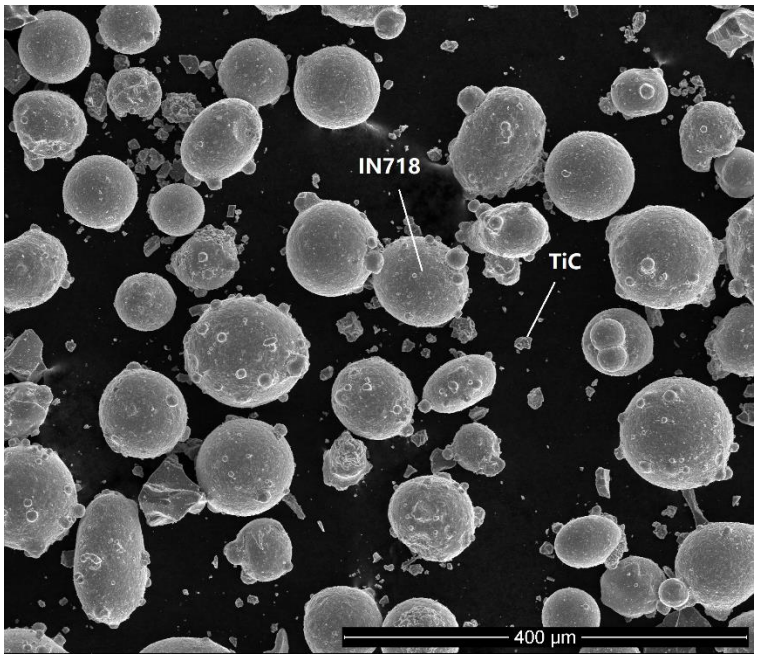

Figure 38. Representative SEM image of blended Inconel 718 (IN718) and TiC powders.

The microstructure of the as-deposited samples was characterized by scanning electron microscopy (SEM, FEI Quanta 3D). For higher magnification microstructural and chemical

analysis, we performed transmission electron microscopy (TEM, JEOL 2800) combined with dual energy dispersive X-ray spectroscopy (EDS) detectors, and high-resolution scanning TEM using a double aberration-corrected JEOL JEM-ARM300. The TEM samples were lifted out near the TiC/matrix interface by using focused ion beam (FIB) in an FEI Quanta 3D SEM. For SEM characterization, all samples were mechanically polished, finishing with 1 μm diamond suspension. Pure alloy samples (IN-0 and HA-0) were etched with an electro-polisher (Buehler ElectroMet 4) following mechanical polishing for 15 s under 12 V DC, in 10% perchloric acid and 90% ethanol. The composite samples (IN-5, IN-10, HA-5 and HA-10) were not etched.

Figure 39. Representative photograph of LENS® as-deposited metal matrix composite sample.

5.3. Results

5.3.1 Microstructural characterization

Figure 40 and Figure 41 show representative SEM micrographs of as-deposited Inconel 718 (sample IN-0) and Hayes 282 (sample HA-0), respectively. In sample IN-0, a secondary phase with brighter, elongated shape is observed in the interdendritic regions. EDS analysis suggests that these regions are likely to be Laves phase with high Nb content. The chemical composition of this Laves phase, as determined by EDS analysis, is shown in Table 8 and compared with literature values [96]. In sample HA-0, darker and spheroidal secondary phase regions on the order of less

than 1 μm in size are visible. High resolution TEM results presented later reveal that these regions are likely the γ' phase.

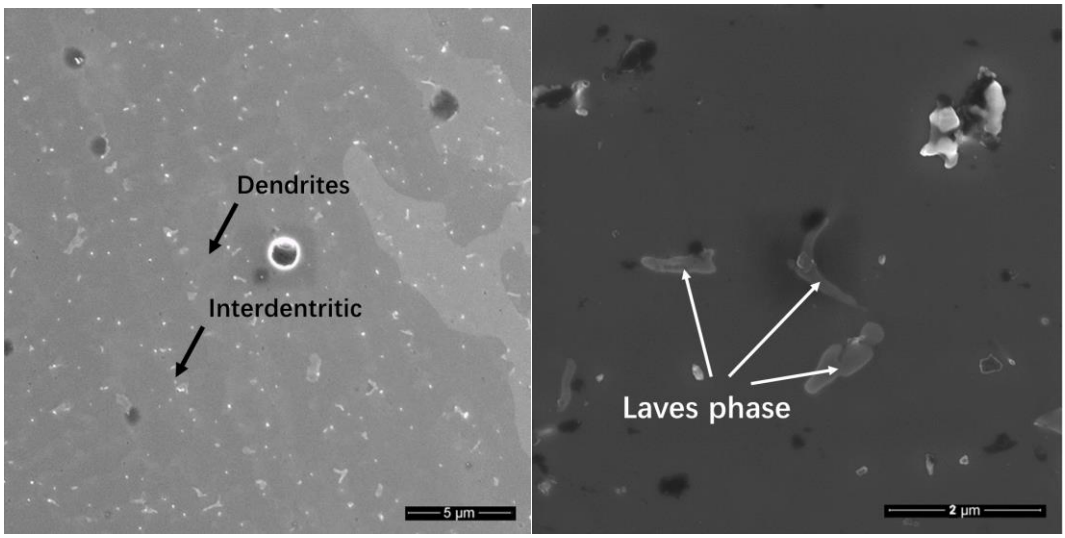

(a) (b)

Figure 40. SEM image showing (a) LENS® as-deposited Inconel 718 (sample IN-0), with irregular, elongated Laves phase visible in the interdentritic region. (b) is at higher magnification image.

Table 8. Chemical composition of the Nb-rich Laves phase as determined by EDS point analysis for sample IN-0. Literature reported values for the Laves phase are provided for comparison.

	Ti	**Nb**	**Ni**	**Cr**	**Fe**	**Mo**
From EDS	2.32	20.86	48.21	14.32	13.01	1.32
Literature Reported [96]	1.426	21.714	45.883	14.298	14.235	3.832

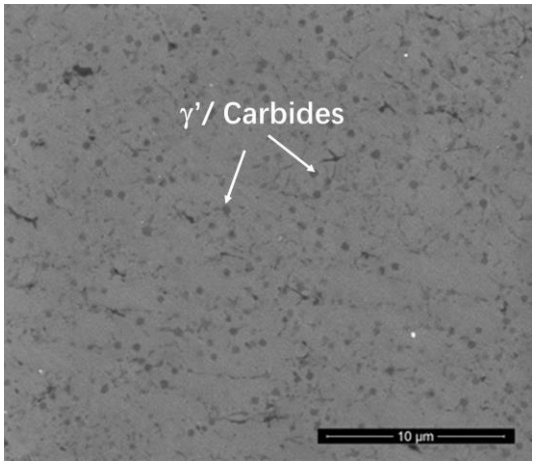

Figure 41. SEM image showing LENS® as-deposited Haynes 282 (sample HA-0), showing darker, fine and spherical γ' phase and carbide phases.

Figure 42 and Figure 43 show the SEM micrographs for the composite samples, IN-10 and HA-10. Severe agglomeration of the original TiC particles, appearing as the darker regions, was not observed in either sample. Some TiC particles show internal cracks (Figure 41b and 41d), which are likely the result of thermal shock during the interaction with the laser beam and molten pool, and residual stresses that result after cooling and solidification [16,98]. A large portion of the original TiC particles present in the builds possess smooth edges, in contrast with the original faceted morphologies found in the starting powder (i.e., compare Figure 37 to Figure 41). Interfacial layers with submicron thickness were observed between the alloy matrix and TiC particles in sample IN-10, while such interfacial layers were not observed in sample HA-10. Secondary precipitate phases are also observed in both alloys and are uniformly dispersed throughout the matrix; these are polygon shaped carbide phases with a size of approximately 1 μm. EDS point analysis at different locations in sample IN-10 (Table 9) suggests that the interfacial layer and secondary precipitate phase have a similar chemical composition – as a multi-element MC-type carbide, (Ti,Nb,Mo)C phase. Hong et al. reported a similar interfacial layer and secondary precipitates in DED deposited Inconel 718/TiC composites [92]. It is noted that the Nb

content in the matrix region of sample IN-10 was measured by EDS to be 0 at%, while by contrast the nominal Nb content in the original alloy was over 5 wt%. Laves phase was not observed in the matrix region of sample IN-10.

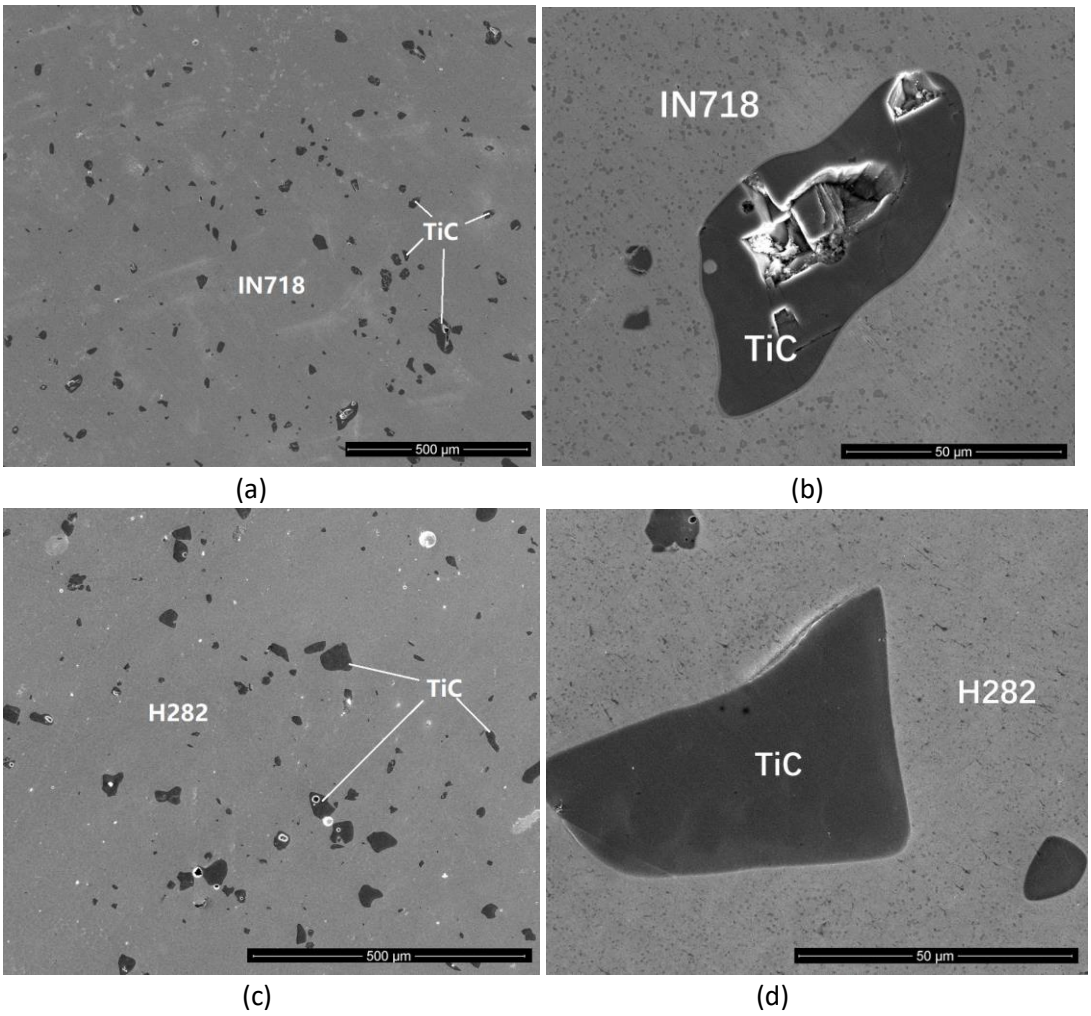

Figure 42. SEM images showing LENS® as-deposited (a) (b) sample IN-10, and (c) (d) sample HA-10. (b) and (d) are higher magnification images showing details of TiC particles in (a) and (c), respectively.

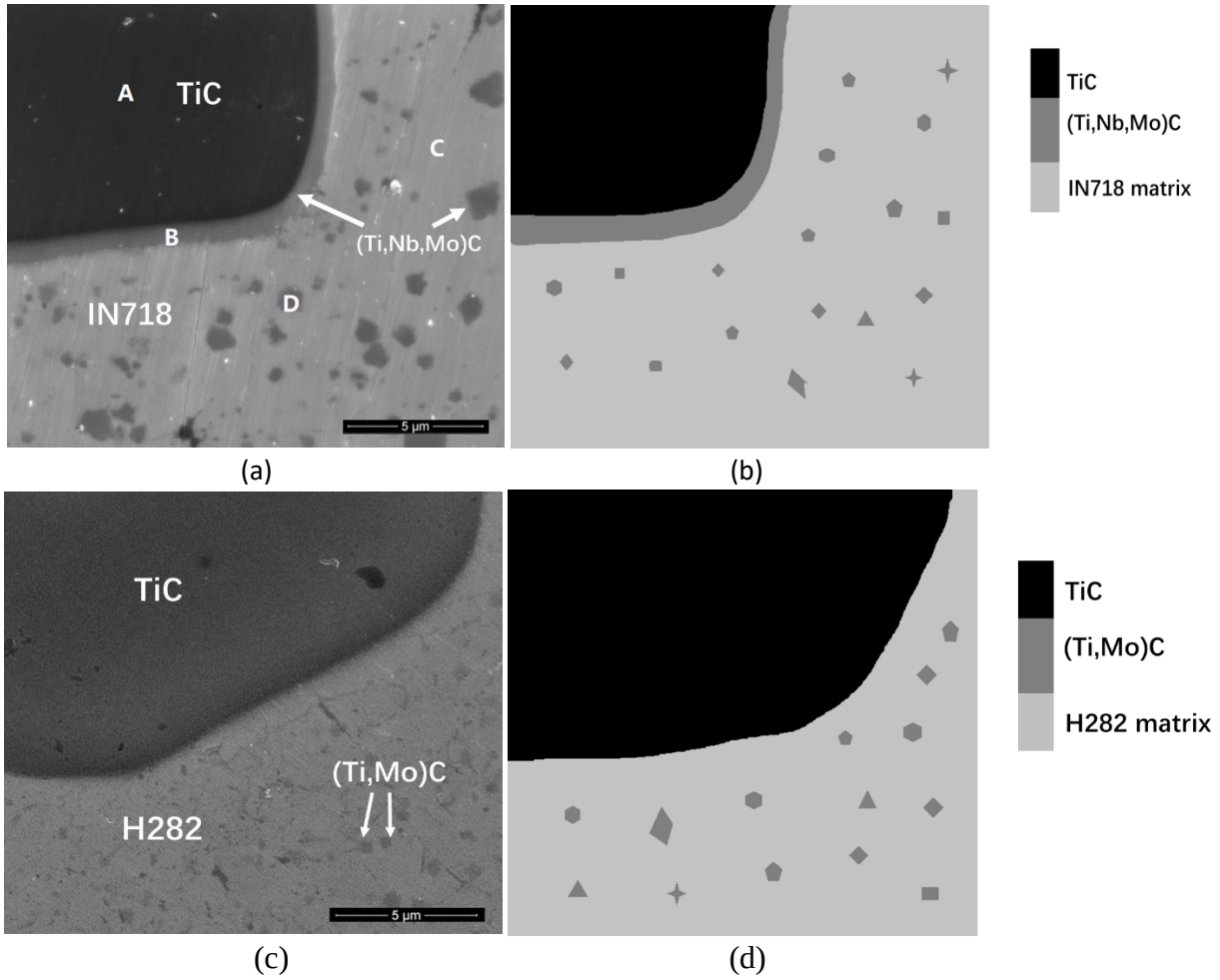

Figure 43. SEM images of TiC/matrix interfaces for (a) sample IN-10 and (c) sample HA-10. (b) and (d) are schematic representation of the phases seen in (a) and (c), respectively. Interface layer of 1-2 μm thickness was visible in IN-10, but was absent in HA-10. Locations selected for EDS analysis in sample IN-10: A: TiC particle, B: interfacial layer, C: Inconel 718 matrix, D: secondary phase precipitates.

Table 9. EDS point analysis (atom %) for select regions in sample IN-10 (see Figure 4a).

	A	B	C	D
C	56.88	62.00	0	53.68
Ti	43.12	24.86	3.24	14.96
Cr	-	1.58	20.98	5.65
Fe	-	0	14.64	2.39
Co	-	0	2.83	1.24
Ni	-	1.04	55.91	10.43
Nb	-	8.11	0	8.65
Mo	-	2.40	2.39	2.99

To further understand the chemical composition and crystalline orientation of the interfacial layer and the precipitates, TEM characterization was carried out in regions adjacent to TiC particles for both composites. Figure 44 shows a TEM bright field image near a TiC particle in sample IN-10. The chemical composition for the interfacial layer and secondary precipitates in sample IN-10 was determined by EDS mapping, as shown in Figure 45 and Figure 46. The results confirm that both the interfacial layer and the secondary precipitates were Nb- and Mo-rich multi-element MC-type carbide, (Ti,Nb,Mo)C phase. A high density of geometrically necessary dislocations (GND) was observed in this interfacial layer, which form due to the thermal stress induced by the mismatch of the thermal expansion coefficients during the cooling process [99,100]. The diffraction patterns at the IN-10 interface layer and TiC particle (Figure 43c and 43d) indicate identical crystallographic structures and orientations. Closer examination of the diffraction pattern indicates that the [110] signals are present in the nickel matrix, which suggest formation of the

ordered γ' ($Ni_3(Al,Ti)$) superlattice. The γ' phase was not identifiable in SEM images (Figure 41a and 41b), probably due to its small size stemming from the high cooling rate during LENS® deposition (10^3-10^4K/s) [9].

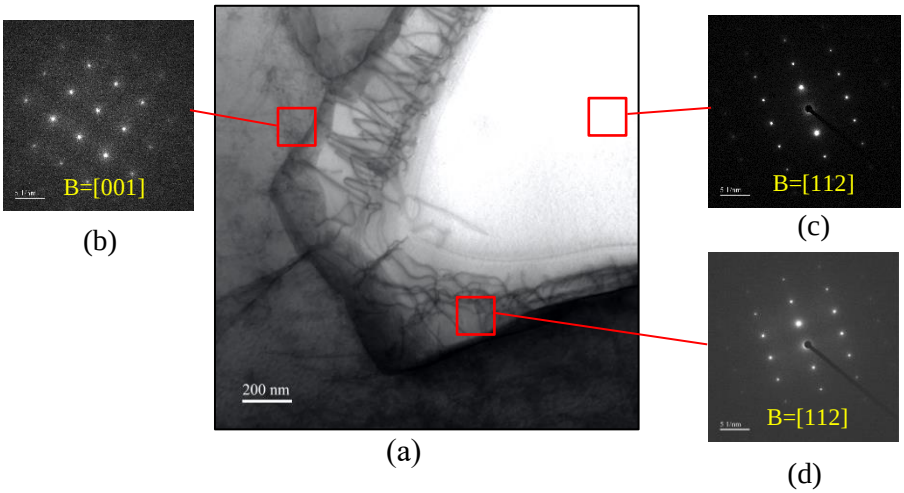

Figure 44. TEM bright field image showing region (a) near Inconel 718/TiC interface in sample IN-10, and diffraction patterns at (b) Inconel 718 matrix, (c) TiC particle, and (d) interface layer.

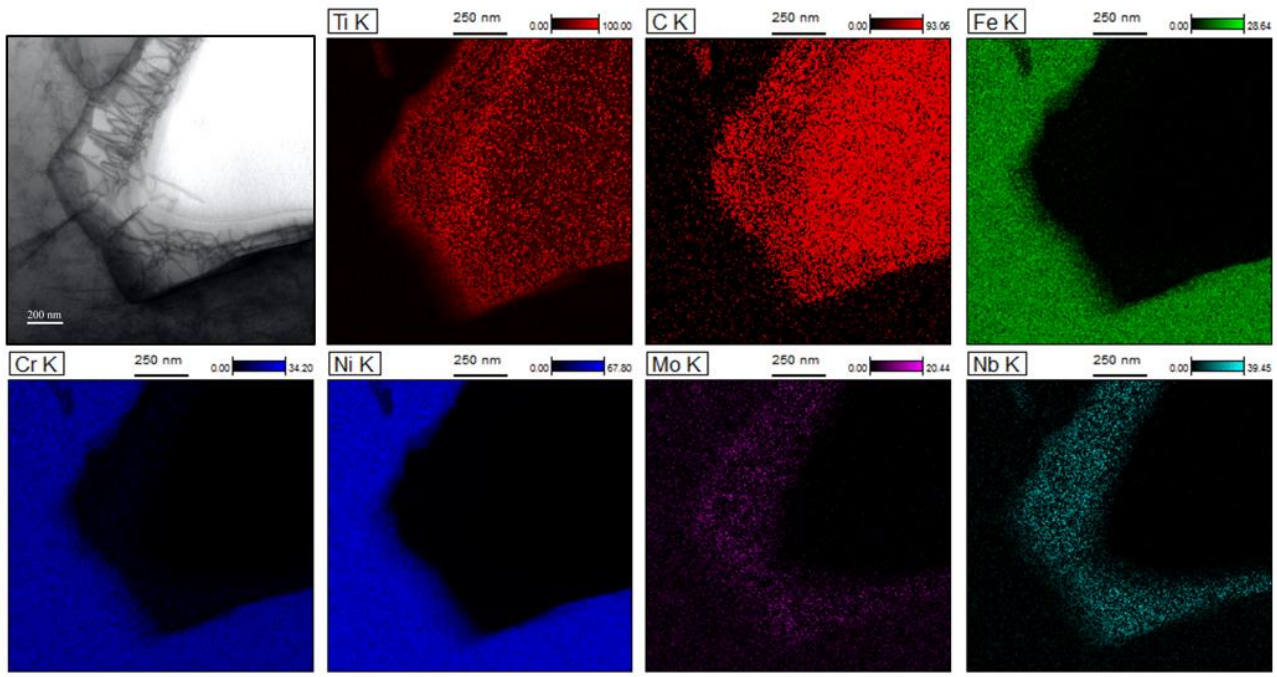

Figure 45. EDS mapping results near TiC/Inconel 718 interface in sample IN-10.

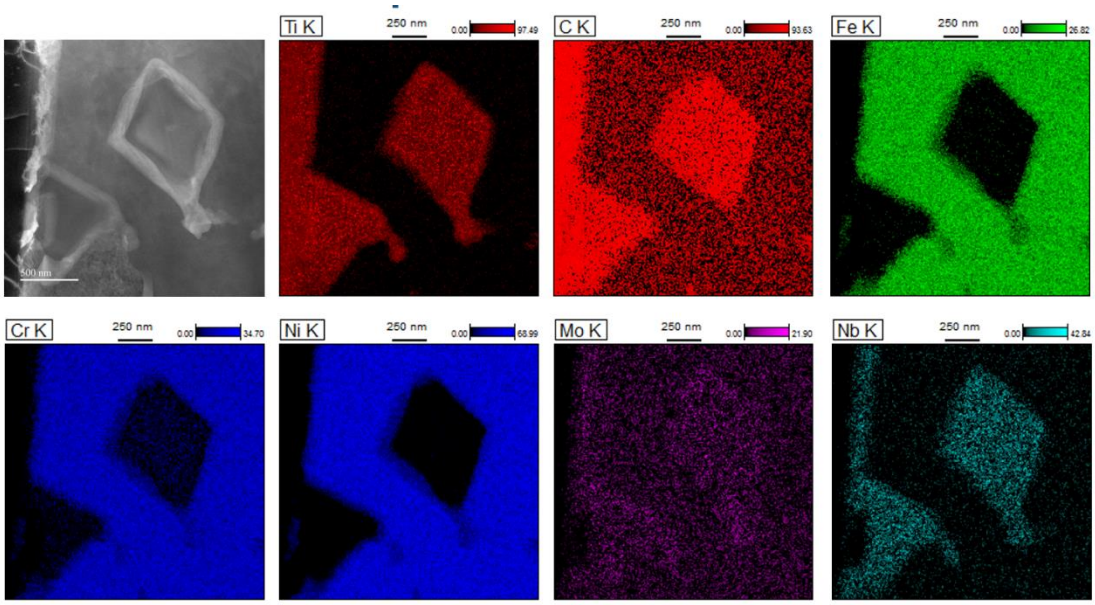

Figure 46. EDS mapping results of multi-element carbide precipitation phase in Inconel 718 matrix in sample IN-10.

Figure 47 shows a TEM bright field image near the Haynes 282/TiC interface in sample HA-10. A less than 100 nm thick layer region can be observed. EDS data suggest that the interface is rich in Mo. The diffraction patterns corresponding to the TiC and matrix regions are shown in Figure 47 b and 47 c, respectively. Similar to the findings for sample IN-10, the [110] signals that correspond to the γ' superlattice are again identified in the nickel matrix. High-resolution TEM was performed in the matrix region, as shown in Figure 48a. Precipitate phases in the size of 5-7 nm can be identified. The [110] signals (red circles in Figure 47c) in fast Fourier transform (FFT) results further confirm the formation of the γ' phase.

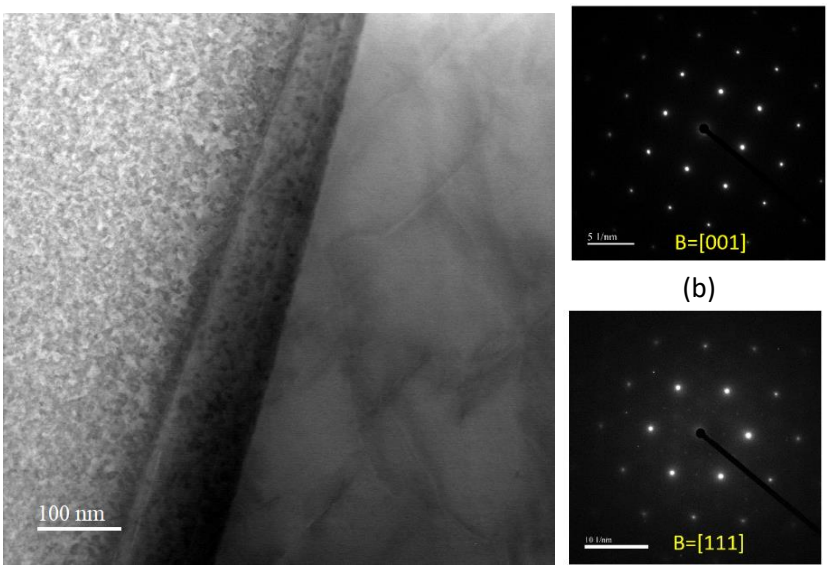

Figure 47. (a) TEM bright field image showing region near Haynes 282/TiC interfaceHA-10, and diffraction patterns at (b) TiC particle and (c) matrix.

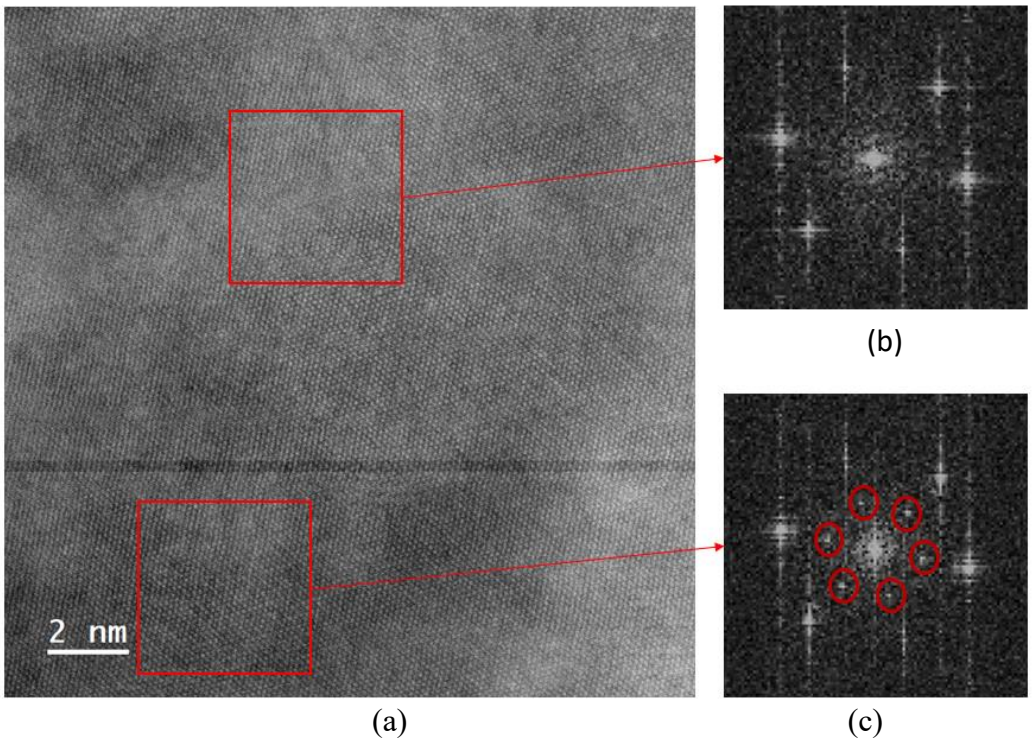

Figure 48. (a) HRTEM image of Haynes 282 matrix in sample HA-10, and (b) (c) FFT applied at different regions. The [110] signals (red circles in (c)) suggest formation of the γ' phase.

5.3.2 Mechanical Behavior

The tensile test results for the as-deposited Inconel 718/TiC and Haynes 282/TiC samples are presented in Table 10. For both alloys, significant increases in yield strength (YS) and ultimate tensile strength (UTS) are observed for the TiC reinforced composites, as is expected for MMCs [100,101]. The YS values for samples IN-0, IN-5 and IN-10 are 555, 1008 and 1033 MPa, respectively, and the UTS values are 928, 1168 and 1208 MPa, respectively. The YS values for samples HA-0, HA-5 and HA-10 are 548, 967 and 1138 MPa, respectively, and the UTS values are 876, 1168 and 1248 MPa, respectively. The ductility for both alloys, however, decreased drastically for the TiC reinforced composites, as expected [101]. The ductility for each of the as-deposited pure alloys is greater than 40%, whereas the values were ~2% for samples IN-10 and HA-10.

Table 10. Tensile test results for Inconel 718/TiC and Haynes 282/TiC as-deposited samples. YS = yield strength; UTS = ultimate tensile strength

Sample ID	YS (MPa)	UTS (MPa)	Ductility (%)
IN-0	555	928	44
IN-5	1008	1168	4.4
IN10	1033	1208	2.3
HA-0	548	876	48
HA-5	967	1223	4.8
HA-10	1138	1248	2.0

Figure 49 shows the fracture surfaces of the tensile test specimens for samples IN-10 and HA-10. Ductile fracture is seen in the alloy matrix as evidenced by the presence of a high density

of micron-sized dimples, while the TiC reinforcement particles exhibit brittle transgranular fracture and possibly act as the crack initiation site during tensile tests. No decohesion of the TiC particles is evident for either alloy, and cracks are not seen propagating into the alloy matrix. In related work, Gu et al. reported that no cracks, pores or other defects were formed at interfaces during sliding wear tests [102].

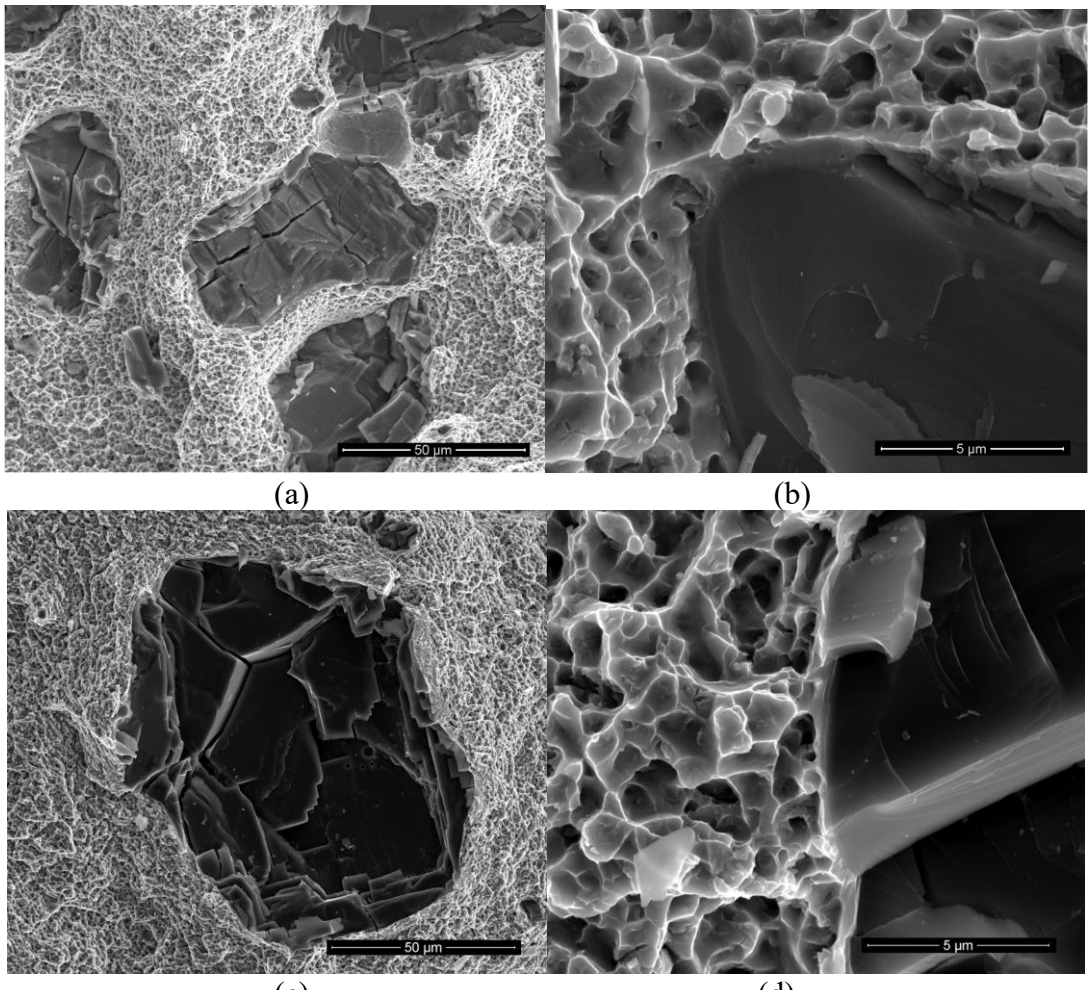

Figure 49. Fracture surface of (a) sample IN-10 and (c) sample HA-10, after tensile tests. (b) and (d) are higher magnification images of (a) and (c), respectively.

5.4. Discussion

5.4.1 Nb segregation and Laves phase in sample IN-0

In sample IN-0, Laves phase formed in the as-deposited samples due to the Nb segregation during solidification. Nb, having the lowest partition coefficient among the other alloying elements, often experiences severe segregation in the interdendritic region in Nb-containing superalloys [96,103]. The Nb content in the interdendritic regions can reach as high as ~24 wt% in as-cast Inconel 718 alloy, while the nominal composition is approximately 5 wt% [96]. Nb segregation and formation of the Laves phase are a common and undesired phenomenon reported for cast Inconel 718 alloys. Proper heat treatment and aging processes are often required to eliminate the Laves phase in order to assure desirable mechanical behavior.

5.4.2. Influence of TiC content on phase formation in the two nickel-based composites

During the LENS® process, some fraction of the TiC particles will undergo melting and dissolve into the nickel alloy matrix, as the molten pool can be overheated to a temperature greater than 3500 K by the laser beam. The smoothed edges of the TiC particles, as shown in Figure 40, provide evidence of partial melting during the interaction with the laser beam and the molten pool [52,92]. Although the exact amount of TiC dissolved is difficult to determine, it is expected that the increased TiC content in the matrix alters the phase evolution in the as-deposited samples. To understand the elemental segregation and phase formation for the two composite systems during LENS®, solidification calculations, based on the Scheil-Gulliver model [104] were performed for both the pure alloys and the composites using Thermo-Calc®. The Scheil-Gulliver model assumes perfect mixing in the liquid and no diffusion in the solid phase, and despite these limiting assumptions has been successfully used to predict solid phase formation in AM [34-39]. It is

plausible that the presence of Marangoni convective flow and liquid diffusion in the melt pool may result in conditions that are close to those for ideal mixing in the melt during solidification. In this work, TiC content values of 2 wt % and 4 wt % in each composite system were selected, to consider the melting and dissolution of TiC into the nickel alloy matrices during deposition. A temperature resolution of 1 K was used for all the calculations.

Figure 50 shows the calculation results for the Inconel 718/TiC system. When there is no TiC content in the system (Figure 50a), the γ matrix phase starts to form at a temperature of 1598 K, followed by the precipitation of the Nb-rich multi-element MC-type carbide phase starting to form at a temperature of approximately 1580 K. δ (Ni_3Nb) and topologically close packed (TCP) phases including the Laves phase and σ phase are predicted to form at lower temperatures. For the system with 2 wt% TiC (Figure 50b), notable differences in the phase formation sequence are observed, as the MC-type carbide phase precipitates before the formation of the γ matrix phase at much higher temperature of 1900 K . δ and Laves phase are still predicted but start to form at lower liquid fractions. For higher TiC content (4 wt%, Figure 50c), a similar solidification curve is predicted, except that the TCP phases were not predicted when solidification is complete. These results suggest that the formation of the Nb-containing phases, including Laves phase and Ni_3Nb in Inconel 718 samples is inhibited as TiC is introduced. These results are in agreement with those from the EDS point analysis provided in Table 9, specifically, no Nb content is observed in the Inconel 718 matrix (point D in Figure 43a) for sample IN-10. In Inconel 718, Nb is one of the most active carbide forming elements, and during the solidification process Nb will compete with Ti and Mo to form the MC-type carbide phase. In Ni-based superalloys, the preferred order of formation for MC type carbide (in order of decreasing stability) is HfC, TaC, NbC and TiC, and less reactive element such as Mo can also substitute in these carbides [105]. This results in the

formation of the (Ti,Nb,Mo)C interfacial layers surrounding the TiC particles and fine precipitates in the matrix, which are discussed further in the next section. Consequently, as all the Nb appears in the aforementioned (Ti,Nb,Mo)C phase, none is left in the Inconel 718 matrix, and therefore Laves phase and Ni_3Nb will not form. On the one hand, the elimination of Laves phase is beneficial since the Laves phase is known to be brittle and detrimental to the alloy mechanical behavior, while on the other hand, γ'' (Ni_3Nb), an important strengthening phase for Inconel 718, will also be inhibited as TiC content increases. Further study is needed to understand the overall effect on the mechanical behavior due to this altered phase evolution.

Figure 51 presents the Scheil calculation results for the Haynes 282/TiC system. Unlike in the Inconel 718/TiC system, only the multi-element MC-type carbide phase and the Cr-rich σ phase are predicted, other than the γ matrix phase. The composition of the MC-type carbide is mostly (Ti (Mo))C for this Haynes-based composite, instead of Nb-rich carbide, as was seen for the Inconel 718/TiC. The Mo content in the MC-type carbide phase is slightly higher in the Haynes/TiC than in the Inconel 718/TiC. Table 11 compares the calculated chemical composition of the multi-element MC-type carbide phase in both composites.

Figure 52 presents the calculated mole percent of each phase for the two composite systems. γ matrix phase is not shown in these diagrams so that the y-axis can be expanded for easier viewing. For both alloys, the amount of MC-type carbide phase increases as more TiC is added into the system. For the Inconel 718/TiC system, δ and Laves phases exhibit a decreasing trend as the TiC content is increased from 0 to 4 wt%, while γ' phase exhibits an increasing trend, due to the higher Ti content. For the Haynes 282/TiC system, other than the increase in Ti-rich MC-type carbide phase content, the other secondary phases (γ' and σ) do not exhibit significant changes as a function of TiC content. As Nb is competing with Ti to form the multi-element MC-type

(Ti,Nb,Mo)C carbide phase, more Ti will remain in the matrix, and therefore favor the formation of the γ' (Ni_3Ti) phase in Inconel 718. The mole percent of Ni_3Ti phase increases from 0 to 2.2 % as the TiC content is increased to 4 wt%. The above phenomena in Inconel 718/TiC system can be expressed by the following reaction:

$$TiC + Ni + Nb + Mo \rightarrow (Ti, Nb, Mo)C + Ni_3Ti \quad (1)$$

By contrast, the increased TiC content in the Haynes 282 alloy does not have a significant influence on phase formation in the matrix, as there is a lack of Nb in the Haynes 282 alloy, and therefore the carbide composition remains roughly Ti:C=1:1. The Ni_3Ti phase remains at a value of approximately 0.5-1 mole % for all the TiC compositions in the Haynes 282/TiC system. Although the γ' strengthening phase typically forms after proper heat treatment, HRTEM (Figure 48) and diffraction patterns in TEM (Figure 44b) suggest that fine, spherical γ' precipitates with a scale of several nanometers are observed in both composites. Several studies have reported the formation of fine γ' phase in DED as-deposited Ni superalloy samples [92,94,95]. The accumulation of thermal energy and continuous heating and cooling cycles that occur during the deposition may promote the formation of the γ' phase [95]. Since Inconel 718 is designed to be strengthened primarily by the γ'' phase and usually contains much less γ' phase, the decrease in γ'' content and increase in γ' content due to the TiC addition may affect the mechanical behavior and stability of the Inconel 718 matrix. The above results suggest that γ' strengthened superalloys might be more suitable and experience less severe undesirable phase alteration when TiC is added as a reinforcement particle during DED processing.

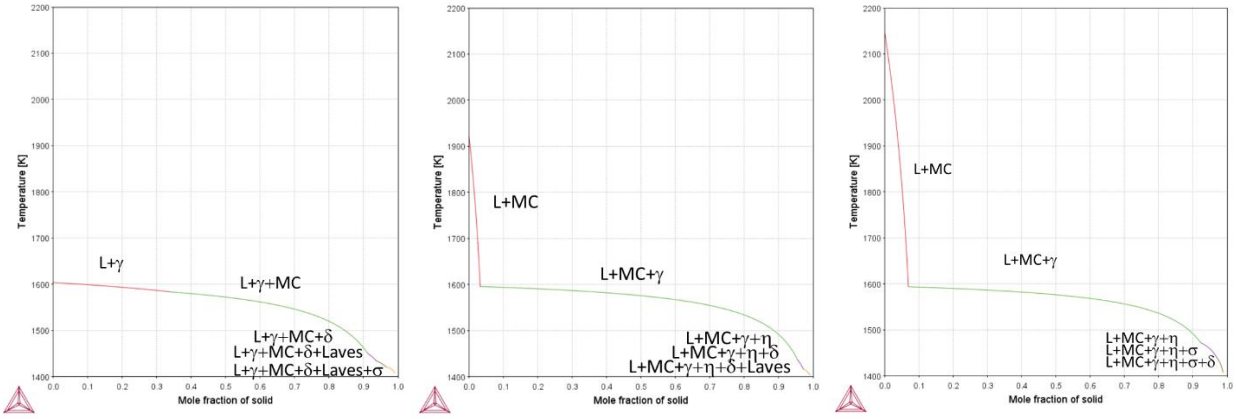

(a) (b) (c)

Figure 50. Scheil solidification calculation for (a) Inconel 718, (b) Inconel 718 + 2 wt.% TiC, and (c) Inconel 718 + 4 wt.% TiC.

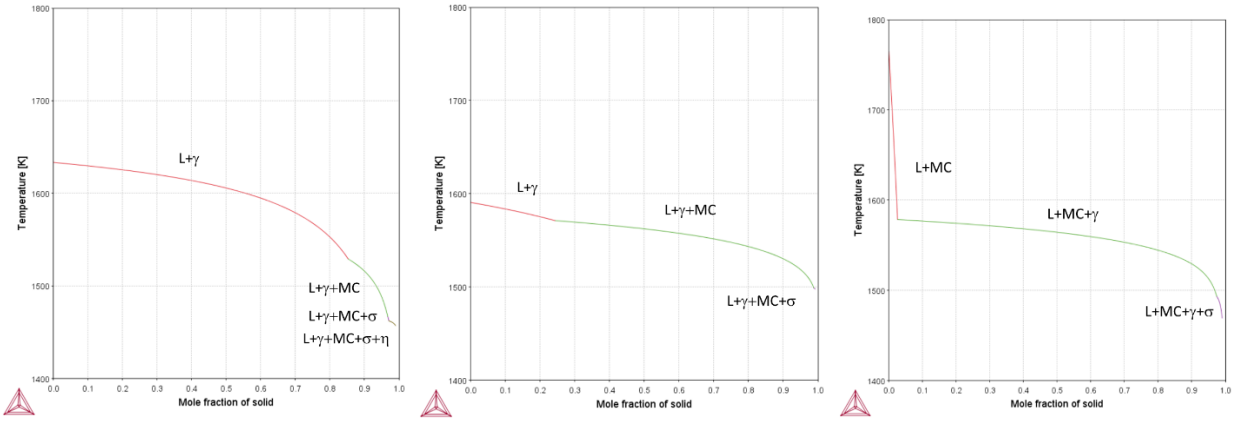

(a) (b) (c)

Figure 51. Scheil solidification calculation for (a) Haynes 282, (b) Haynes 282 + 2 wt.% TiC, and (c) Haynes 282 + 4 wt.% TiC.

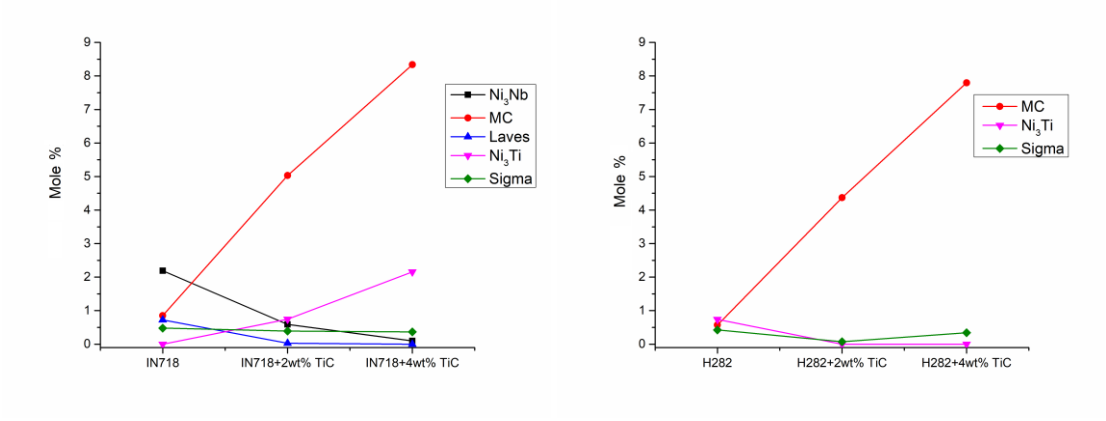

(a) (b)

Figure 52. Calculated phase composition in (a) Inconel 718/TiC and in (b) Haynes 282/TiC for various TiC content values. Values for the γ phase (balance of composition) are not shown.

Table 11. Calculated chemical composition (mole %) for the multi-element MC-type carbide phases after complete solidification, as determined from the Scheil solidification curves.

	IN718	**IN718+ 2%TiC**	**IN718+ 4%TiC**	**HA282**	**HA282+ 2%TiC**	**HA282+ 4%TiC**
Cr	0.067	0.062	0.072	0.094	0.260	0.120
Ti	11.1	18.4	24.2	52.9	49.8	52.4
C	47.7	48.1	48.2	45.7	46.3	45.9
Nb	40.8	33.3	27.3	-	-	-
Mo	0.15	0.16	0.20	1.29	3.58	1.55

5.4.3 Formation of interfacial layers and precipitates in sample IN-10

The formation of the (Ti,Nb,Mo)C carbide phase interfacial layers and precipitates has been previously reported in the literature for additively manufactured TiC reinforced Nb-containing nickel superalloy composites [92]. In their work, the formation mechanism for this (Ti,Nb,Mo)C phase was explained via a diffusion and dissolution-precipitation phenomena: the Ti and C atoms are released from a TiC particle during heating and diffuse into the molten pool, and then react with Nb and Mo from liquid Inconel 718 to form the (Ti,Nb,Mo)C interfacial layer and precipitates. From the EDS analysis and TEM diffraction patterns in the current study, the

interfacial layers and precipitates in sample IN-10 have been identified to be a MC-type carbide phase, with an ordered FCC crystal structure. The Scheil solidification calculations shown in Figures 50b and 50c suggest that the (Ti,Nb,Mo)C phase will precipitate first before the solidification of the γ matrix when the TiC content is greater than 2 wt%. On this basis one can speculate that when unmelted TiC particles are present in the molten pool, (Ti,Nb,Mo)C is likely to nucleate on TiC particles as the molten pool undergoes solidification, and eventually forms an interfacial layer surrounding the TiC particle. Since the TiC, MoC and NbC share the identical FCC crystal structure with very similar lattice parameters, it is plausible that the Nb-rich carbide phase interfacial layer grows epitaxially with the same crystalline orientation as the TiC particle. TEM diffraction patterns in Figures 44b and 44c confirm the FCC crystal structure for both the interface and the TiC particle, and indicate that there is no detectable difference in lattice parameters. From another perspective, this phenomenon could be described as the TiC particle experiencing "grain growth" during the solidification of the molten pool, with increased Nb content in the "growth" regions, observed as an interface in both SEM and TEM. The other portion of (Ti,Nb,Mo)C forms as fine and polygon shaped precipitates that are evenly distributed in the matrix, as shown in Figure 42b. In ref. [102], the homogeneous distribution of the (Ti,Nb,Mo)C precipitates was attributed to the vigorous Marangoni convection flow in the molten pool resultant of the large temperature gradient. Large portions of the fine precipitates exhibit diamond or triangular morphologies, which are consistent with (Ti,Nb,Mo)C phase particles nucleating and growing freely relative to the (111) closest packed planes [106,107].

5.4.4 Tensile behavior

The LENS® as-deposited Inconel 718 and Haynes 282 composites exhibit similar YS and

UTS values for a given TiC content, even though there are Nb-rich interfacial layers present in samples IN-5 and IN-10. The hypothesis that the interfacial layer could potentially enhance the wettability of TiC in the Ni matrix and therefore be beneficial to the tensile properties may not be valid given the very similar YS and UTS values for samples IN-5 and HA-5, as well as for samples IN-10 and HA-10. Instead, for both alloy systems the 5 wt% TiC composite samples exhibit significantly higher YS and UTS values when compared to the pure alloys, and these values increase further when the TiC is increased to 10 wt%. The increase in YS and UTS is mainly attributed to the well-known strengthening effects caused by thermal mismatch induced strain hardening [16][101], which led to the high density of geometrically necessary dislocations observed in Figure 43a. The morphology of the fracture surfaces suggest that failure was initiated inside the TiC particles, as they may undergo thermal shock when interacting with the laser beam and molten pool [3,98]. No apparent delamination was visible at the interface between the TiC and the matrix for both alloys (Figure 49). In this work, the size of the reinforcement TiC particles is as large as 20-45 μm, which favors crack initiation inside the particle instead of occurring at the particle-matrix interface [108,109]. Thus, for both sets of as-deposited composites, the tensile behavior is dominated by the response of the TiC particles rather than the variations in phase and composition in the matrix, as described above.

5.5. Summary

In the present work, Inconel 718/TiC and Haynes 282/TiC MMC samples were successfully fabricated via LENS®. The phase formation and microstructure were characterized in SEM and TEM and analyzed with Scheil solidification calculations. Some of the key findings are summarized below:

(1) Submicron interfacial layers of (Ti,Nb,Mo)C-type multi-elemental carbide phase with the same crystalline orientation as the ex-situ added TiC particles were observed in the Inconel 718/TiC composites. High geometrically necessary dislocations density was observed within the interfacial layers.

(2) Fine, spheroidal γ' phase was identified by HRTEM in the matrix phase for both the Inconel 718/TiC and Haynes 282/TiC as-deposited samples.

(3) Scheil solidification calculations indicate that an increase in TiC content inhibits the formation of the detrimental Laves phase and δ phase in Inconel 718/TiC samples, since the Nb has a higher tendency to form MC-type carbides during solidification. On the other hand, the increased Ti content remaining in the matrix tends to promote the formation of the γ' phase. The increased TiC content was not found to have a significant effect on the phases in the matrix of the Haynes 282/TiC MMCs.

(4) Significantly higher YS and UTS values were observed in the as-deposited MMC samples, compared to the as-deposited pure alloys. Examination of the fracture surfaces indicated that failure possibly initiated from cracks that form within the TiC particles.

Chapter 6: Conclusions and Future Work

This dissertation investigated the complicated physics that occur at different stages during the DED process, with the aid of high-speed photography and simulation models. These tools can be continuously used for the research of DED processing of other material system. One such example would be the functionally graded materials (FGM). Because DED has excellent flexibility in delivering different types of powder feedstocks, it would be a good fit for additively manufacturing FGM in which the composition of the material is constantly changing at different location. By carefully implementing process control to adjust the powder flowrate for each component, a graded structure can be achieved. In Chapter 2, we have seen that feeding inhomogeneous particle leads to unique challenge to obtain desired compositions in the final product, due to the different flow behavior. In FGM systems, this challenge will persist and will be even bigger when more than two components are used, plus the introduction of another temporal dimension. Different powder flow behavior, latent system response when changing the flowrate, instability during the process and unexpected chemical/physical interactions between each component could all add to the challenges and require more efforts to address. Developing reliable process control methods and design of an effective manufacturing route would be key to successfully implementation of such a complex system.

In Chapter 3 of this dissertation, we have used high-speed photography to observe the molten pool and interactions of particle with the molten pool surface. Although much useful data were acquired, the high speed videos only probe the surface of the molten pool, while the details the surface of the molten pool cannot be revealed. Synchrotron X-ray method can effectively fill this gap. The X-ray is able to capture the dynamic processes radiographically at a high spatial (a few micrometers) and temporal (microseconds to milliseconds) resolution [110], and much

research has been done using this method to observe the formation of pores inside the molten pool as well as the stability of keyholes [110,111]. The method may be especially useful for studying the deposition process of MMCs, in which the movement of the reinforcement ceramic particles can be observed within the molten pool, providing valuable information such as the distribution of the ceramic particles in the matrix, the interaction between the solid phase ceramic and liquid alloy, the solidification of the molten pool etc.

Finally, in Chapter 5, Scheil solidification calculation were performed to understand the phase formation sequence and element segregation during solidification. As mentioned in the text, this method assumes infinitely fast diffusion of the elements and therefore representing equilibrium condition. However, as the cooling rate in DED can reach as high as 10^6 K/s, high undercooling may exist during the solidification and therefore the equilibrium assumptions are no longer valid. A good kinetic model is needed to better describe the rapid solidification process and more accurately predict the phase formation in DED.

REFERENCES

[1] D. Svetlizky, M. Das, B. Zheng, A.L. Vyatskikh, S. Bose, A. Bandyopadhyay, J.M. Schoenung, E.J. Lavernia, N. Eliaz, Directed energy deposition (DED) additive manufacturing: Physical characteristics, defects, challenges and applications, Mater. Today. (2021). https://doi.org/https://doi.org/10.1016/j.mattod.2021.03.020.

[2] B. Zheng, Y. Zhou, J.E. Smugeresky, J.M. Schoenung, E.J. Lavernia, Thermal Behavior and Microstructural Evolution during Laser Deposition with Laser-Engineered Net Shaping: Part I. Numerical Calculations, Metall. Mater. Trans. A. 39 (2008) 2228–2236. https://doi.org/10.1007/s11661-008-9557-7.

[3] I. Gibson, D. Rosen, B. Stucker, Directed Energy Deposition Processes BT - Additive Manufacturing Technologies: 3D Printing, Rapid Prototyping, and Direct Digital Manufacturing, in: I. Gibson, D. Rosen, B. Stucker (Eds.), Springer New York, New York, NY, 2015: pp. 245–268. https://doi.org/10.1007/978-1-4939-2113-3_10.

[4] G. Tapia, A. Elwany, A Review on Process Monitoring and Control in Metal-Based Additive Manufacturing, J. Manuf. Sci. Eng. 136 (2014). https://doi.org/10.1115/1.4028540.

[5] P. Balu, P. Leggett, R. Kovacevic, Parametric study on a coaxial multi-material powder flow in laser-based powder deposition process, J. Mater. Process. Technol. 212 (2012) 1598–1610. https://doi.org/10.1016/j.jmatprotec.2012.02.020.

[6] J.C. Haley, B. Zheng, U.S. Bertoli, A.D. Dupuy, J.M. Schoenung, E.J. Lavernia, Working distance passive stability in laser directed energy deposition additive manufacturing, Mater. Des. 161 (2019) 86–94. https://doi.org/https://doi.org/10.1016/j.matdes.2018.11.021.

[7] J.C. Haley, J.M. Schoenung, E.J. Lavernia, Observations of particle-melt pool impact events in directed energy deposition, Addit. Manuf. 22 (2018) 368–374. https://doi.org/https://doi.org/10.1016/j.addma.2018.04.028.

[8] U. Scipioni Bertoli, G. Guss, S. Wu, M.J. Matthews, J.M. Schoenung, In-situ characterization of laser-powder interaction and cooling rates through high-speed imaging of powder bed fusion additive manufacturing, Mater. Des. 135 (2017) 385–396. https://doi.org/https://doi.org/10.1016/j.matdes.2017.09.044.

[9] T. DebRoy, H.L. Wei, J.S. Zuback, T. Mukherjee, J.W. Elmer, J.O. Milewski, A.M. Beese, A. Wilson-Heid, A. De, W. Zhang, Additive manufacturing of metallic components – Process, structure and properties, Prog. Mater. Sci. 92 (2018) 112–224. https://doi.org/https://doi.org/10.1016/j.pmatsci.2017.10.001.

[10] Y. Xiong, W.H. Hofmeister, Z. Cheng, J.E. Smugeresky, E.J. Lavernia, J.M. Schoenung, In situ thermal imaging and three-dimensional finite element modeling of tungsten carbide–cobalt during laser deposition, Acta Mater. 57 (2009) 5419–5429. https://doi.org/https://doi.org/10.1016/j.actamat.2009.07.038.

[11] D. Rosenthal, The Theory of Moving Sources of Heat and Its Application of Metal Treatments, Trans. ASME. 68 (1946) 849–866. http://ci.nii.ac.jp/naid/10004812806/en/ (accessed November 6, 2021).

[12] R. Vilar, 10.07 - Laser Powder Deposition, in: S. Hashmi, G.F. Batalha, C.J. Van Tyne, B.B.T.-C.M.P. Yilbas (Eds.), Elsevier, Oxford, 2014: pp. 163–216. https://doi.org/https://doi.org/10.1016/B978-0-08-096532-1.01005-0.

[13] J.C. Ion, K.E. Easterling, M.F. Ashby, A second report on diagrams of microstructure and hardness for heat-affected zones in welds, Acta Metall. 32 (1984) 1949–1962. https://doi.org/https://doi.org/10.1016/0001-6160(84)90176-7.

[14] T. Eagar, N.-S. TSAI, Temperature Fields Produced by Traveling Distributed Heat Sources Use of a Gaussian heat distribution in dimensionless form indicates final weld pool shape can be predicted accurately for many welds and materials, Weld. J. (Miami, Fla). 62 (1983).

[15] T. Mukherjee, W. Zhang, T. DebRoy, An improved prediction of residual stresses and distortion in additive manufacturing, Comput. Mater. Sci. 126 (2017) 360–372. https://doi.org/https://doi.org/10.1016/j.commatsci.2016.10.003.

[16] B. Al-Mangour, Additive Manufacturing of Emerging Materials, 2019. https://doi.org/10.1007/978-3-319-91713-9.

[17] C. Atwood, M. Griffith, L. Harwell, E. Schlienger, M. Ensz, J. Smugeresky, T. Romero, D. Greene, D. Reckaway, Laser engineered net shaping (LENS^{TM}): A tool for direct fabrication of metal parts, Int. Congr. Appl. Lasers Electro-Optics. 1998 (1998) E1–E7. https://doi.org/10.2351/1.5059147.

[18] Y. Hu, W. Cong, A Review on Laser Deposition-Additive Manufacturing of Ceramics and Ceramic Reinforced Metal Matrix Composites, Ceram. Int. (2018). https://doi.org/10.1016/j.ceramint.2018.08.083.

[19] J. Hashim, L. Looney, M.S.J. Hashmi, Metal matrix composites: production by the stir casting method, J. Mater. Process. Technol. 92–93 (1999) 1–7. https://doi.org/https://doi.org/10.1016/S0924-0136(99)00118-1.

[20] M.P. Behera, T. Dougherty, S. Singamneni, Conventional and Additive Manufacturing with Metal Matrix Composites: A Perspective, Procedia Manuf. 30 (2019) 159–166. https://doi.org/https://doi.org/10.1016/j.promfg.2019.02.023.

[21] D. Gu, H. Wang, F. Chang, D. Dai, P. Yuan, Y.-C. Hagedorn, W. Meiners, Selective Laser Melting Additive Manufacturing of TiC/AlSi10Mg Bulk-form Nanocomposites with Tailored Microstructures and Properties, Phys. Procedia. 56 (2014) 108–116. https://doi.org/https://doi.org/10.1016/j.phpro.2014.08.153.

[22] S. Li, Q. Wei, D. Zhang, C. Kai, Microstructures and Texture of Inconel 718 Alloy Fabricated by Selective Laser Melting, 2014. https://doi.org/10.3850/978-981-09-0446-3_021.

[23] B. Zheng, J.E. Smugeresky, Y. Zhou, D. Baker, E.J. Lavernia, Microstructure and Properties of Laser-Deposited Ti6Al4V Metal Matrix Composites Using Ni-Coated Powder, Metall. Mater. Trans. A. 39 (2008) 1196–1205. https://doi.org/10.1007/s11661-008-9498-1.

[24] Y. Hu, F. Ning, X. Wang, H. Wang, B. Zhao, W. Cong, Y. Li, Laser deposition-additive manufacturing of in situ TiB reinforced titanium matrix composites: TiB growth and part performance, Int. J. Adv. Manuf. Technol. 93 (2017) 3409–3418. https://doi.org/10.1007/s00170-017-0769-0.

[25] A.A. Filippov, V.M. Fomin, A.G. Malikov, A.M. Orishich, Selective laser sintering of cermet mixtures Ti and B4C, AIP Conf. Proc. 1770 (2016) 30095. https://doi.org/10.1063/1.4964037.

[26] B. AlMangour, D. Grzesiak, J.-M. Yang, In-situ formation of novel TiC-particle-reinforced 316L stainless steel bulk-form composites by selective laser melting, J. Alloys Compd. 706 (2017) 409–418. https://doi.org/https://doi.org/10.1016/j.jallcom.2017.01.149.

[27] H. Attar, M. Bönisch, M. Calin, L.-C. Zhang, S. Scudino, J. Eckert, Selective laser melting of in situ titanium–titanium boride composites: Processing, microstructure and mechanical properties, Acta Mater. 76 (2014) 13–22. https://doi.org/https://doi.org/10.1016/j.actamat.2014.05.022.

[28] H. Niu, I. Chang, Selective laser sintering of gas atomized M2 high speed steel powder, J. Mater. Sci. 35 (2000) 31–38. https://doi.org/10.1023/A:1004720011671.

[29] W. Zhou, X. Sun, K. Tsunoda, K. Kikuchi, N. Nomura, K. Yoshimi, A. Kawasaki, Powder fabrication and laser additive manufacturing of MoSiBTiC alloy, Intermetallics. 104 (2019) 33–42. https://doi.org/https://doi.org/10.1016/j.intermet.2018.10.012.

[30] D. Eisenbarth, P.M. Borges Esteves, F. Wirth, K. Wegener, Spatial powder flow measurement and efficiency prediction for laser direct metal deposition, Surf. Coatings Technol. 362 (2019) 397–408. https://doi.org/https://doi.org/10.1016/j.surfcoat.2019.02.009.

[31] F. Zhang, J. Chen, H. Tan, X. Lin, W. Huang, Composition control for laser solid forming from blended elemental powders, Opt. Laser Technol. 41 (2009) 601–607. https://doi.org/https://doi.org/10.1016/j.optlastec.2008.10.006.

[32] A. Lamikiz, I. Tabernero, E. Ukar, S. Martínez, L. Lacalle, Current Designs of Coaxial Nozzles for Laser Cladding, Recent Patents Mech. Eng. 4 (2011) 29–36. https://doi.org/10.2174/2212797611104010029.

[33] A.J. Pinkerton, An analytical model of beam attenuation and powder heating during coaxial laser direct metal deposition, J. Phys. D. Appl. Phys. 40 (2007) 7323–7334. https://doi.org/10.1088/0022-3727/40/23/012.

[34] Z. Liu, H.-C. Zhang, S. Peng, H. Kim, D. Du, W. Cong, Analytical modeling and experimental validation of powder stream distribution during direct energy deposition, Addit. Manuf. 30 (2019) 100848. https://doi.org/https://doi.org/10.1016/j.addma.2019.100848.

[35] F. Mazzucato, S. Tusacciu, M. Lai, S. Biamino, M. Lombardi, A. Valente, Monitoring Approach to Evaluate the Performances of a New Deposition Nozzle Solution for DED Systems, Technologies. 5 (2017) 29. https://doi.org/10.3390/technologies5020029.

[36] O. Kovalev, A. Zaitsev, D. Novichenko, I. Smurov, Theoretical and Experimental Investigation of Gas Flows, Powder Transport and Heating in Coaxial Laser Direct Metal

Deposition (DMD) Process, J. Therm. Spray Technol. 20 (2011) 465–478. https://doi.org/10.1007/s11666-010-9539-3.

[37] H. Pan, T. Sparks, Y. Thakar, F. Liou, The Investigation of Gravity-Driven Metal Powder Flow in Coaxial Nozzle for Laser-Aided Direct Metal Deposition Process, J. Manuf. Sci. Eng. Asme - J MANUF SCI ENG. 128 (2006). https://doi.org/10.1115/1.2162588.

[38] G.D. Smith, An Introduction to Fluid Dynamics, Phys. Bull. 10 (1959) 13–13. https://doi.org/10.1088/0031-9112/10/1/007.

[39] Computational Fluid Dynamics: Physical Law based Finite Volume Method, Introd. to Comput. Fluid Dyn. (2016) 251–269. https://doi.org/doi:10.1002/9781119369189.ch8.

[40] COMSOL Multiphysics 5.3a examples, Flow Past a Cylinder, (2019). https://www.comsol.com/model/download/449401/models.mph.cylinder_flow.pdf.

[41] A. Haider, O. Levenspiel, Drag coefficient and terminal velocity of spherical and nonspherical particles, Powder Technol. 58 (1989) 63–70. https://doi.org/https://doi.org/10.1016/0032-5910(89)80008-7.

[42] E.P. Cox, A Method of Assigning Numerical and Percentage Values to the Degree of Roundness of Sand Grains, J. Paleontol. 1 (1927) 179–183. http://www.jstor.org/stable/1298056.

[43] G.H. Yeoh, J. Tu, Chapter 4 - Gas–Particle Flows, in: G.H. Yeoh, J.B.T.-C.T. for M.F. Tu (Eds.), Butterworth-Heinemann, Oxford, 2010: pp. 243–311. https://doi.org/https://doi.org/10.1016/B978-0-08-046733-7.00004-7.

[44] M. Sommerfeld, N. Huber, Experimental analysis of modelling of particle-wall collisions, Int. J. Multiph. Flow. 25 (1999) 1457–1489. https://doi.org/10.1016/S0301-9322(99)00047-6.

[45] INCONEL® alloy 718, Corp. Spec. Met. (2007). https://www.specialmetals.com/assets/smc/documents/inconel_alloy_718.pdf.

[46] S.-H.K. James F. Shackelford, Young-Hwan Han, Sukyoung Kim, CRC Materials Science and Engineering Handbook, CRC Press, 2016.

[47] Gases - Dynamic Viscosity Absolute viscosities of gases, Eng. TooolBox. (2014). https://www.engineeringtoolbox.com/gases-absolute-dynamic-viscosity-d_1888.html (accessed October 25, 2021).

[48] R. Israel, D.E. Rosner, Use of a Generalized Stokes Number to Determine the Aerodynamic Capture Efficiency of Non-Stokesian Particles from a Compressible Gas Flow, Aerosol Sci. Technol. 2 (1982) 45–51. https://doi.org/10.1080/02786828308958612.

[49] M.J. Matthews, G. Guss, S.A. Khairallah, A.M. Rubenchik, P.J. Depond, W.E. King, Denudation of metal powder layers in laser powder bed fusion processes, Acta Mater. 114 (2016) 33–42. https://doi.org/https://doi.org/10.1016/j.actamat.2016.05.017.

[50] J. Karlsson, A. Snis, H. Engqvist, J. Lausmaa, Characterization and comparison of materials produced by Electron Beam Melting (EBM) of two different Ti–6Al–4V powder fractions, J. Mater. Process. Technol. 213 (2013) 2109–2118. https://doi.org/https://doi.org/10.1016/j.jmatprotec.2013.06.010.

[51] M.C.H. Karg, M. Rasch, K. Schmidt, S.A.E. Spitzer, T.F. Karsten, D. Schlaug, C.-R. Biaciu, A.I. Gorunov, M. Schmidt, Laser Alloying Advantages by Dry Coating Metallic Powder Mixtures with SiOx Nanoparticles, Nanomater. . 8 (2018). https://doi.org/10.3390/nano8100862.

[52] B. Zheng, T. Topping, J.E. Smugeresky, Y. Zhou, A. Biswas, D. Baker, E.J. Lavernia, The Influence of Ni-Coated TiC on Laser-Deposited IN625 Metal Matrix Composites, Metall. Mater. Trans. A. 41 (2010) 568–573. https://doi.org/10.1007/s11661-009-0126-5.

[53] E. Gärtner, H.Y. Jung, N.J. Peter, G. Dehm, E.A. Jägle, V. Uhlenwinkel, L. Mädler, Reducing cohesion of metal powders for additive manufacturing by nanoparticle dry-coating, Powder Technol. 379 (2021) 585–595. https://doi.org/https://doi.org/10.1016/j.powtec.2020.10.065.

[54] A.J. Cavaleiro, C.M. Fernandes, A.R. Farinha, C. V. Gestel, J. Jhabvala, E. Boillat, A.M.R. Senos, M.T. Vieira, The role of nanocrystalline binder metallic coating into WC after additive manufacturing, Appl. Surf. Sci. 427 (2018) 131–138. https://doi.org/10.1016/J.APSUSC.2017.08.039.

[55] S. Ghosh, Self-Healing Materials: Fundamentals, Design Strategies, and Applications, in: Self-Healing Mater. Fundam. Des. Strateg. Appl., 2009: pp. 1–28. https://doi.org/10.1002/9783527625376.ch1.

[56] R. Das, C. Melchior, K.M. Karumbaiah, 11 - Self-healing composites for aerospace applications, in: S. Rana, R.B.T.-A.C.M. for A.E. Fangueiro (Eds.), Woodhead

Publishing, 2016: pp. 333–364. https://doi.org/https://doi.org/10.1016/B978-0-08-100037-3.00011-0.

[57] R. Lumley, Self Healing in Aluminium Alloys BT - Self Healing Materials: An Alternative Approach to 20 Centuries of Materials Science, in: S. van der Zwaag (Ed.), Springer Netherlands, Dordrecht, 2007: pp. 219–254. https://doi.org/10.1007/978-1-4020-6250-6_11.

[58] J.C. Haley, J.M. Schoenung, E.J. Lavernia, Modelling particle impact on the melt pool and wettability effects in laser directed energy deposition additive manufacturing, Mater. Sci. Eng. A. 761 (2019) 138052. https://doi.org/10.1016/J.MSEA.2019.138052.

[59] A. Aggarwal, A. Chouhan, S. Patel, D.K. Yadav, A. Kumar, A.R. Vinod, K.G. Prashanth, N.P. Gurao, Role of impinging powder particles on melt pool hydrodynamics, thermal behaviour and microstructure in laser-assisted DED process: A particle-scale DEM – CFD – CA approach, Int. J. Heat Mass Transf. 158 (2020) 119989. https://doi.org/https://doi.org/10.1016/j.ijheatmasstransfer.2020.119989.

[60] D.-G. Lee, H.-Y. Kim, Impact of a Superhydrophobic Sphere onto Water, Langmuir. 24 (2008) 142–145. https://doi.org/10.1021/la702437c.

[61] Stainless Steel - Grade 316 (UNS S31600), AZO Mater. (2001). https://www.azom.com/article.aspx?ArticleID=863 (accessed November 2, 2021).

[62] EngineeringToolBox, Metals - Latent Heat of Fusion, Eng. ToolBox. (2008). https://www.engineeringtoolbox.com/fusion-heat-metals-d_1266.html (accessed November 2, 2021).

[63] Zinc – Specific Heat, Latent Heat of Fusion, Latent Heat of Vaporization, Nucl. Power. (2021). https://www.nuclear-power.com/zinc-specific-heat-latent-heat-vaporization-fusion/#:~:text=Latent Heat of Vaporization of Zinc is 115.3 kJ%2Fmol. (accessed November 2, 2021).

[64] Materials Thermal Properties Database, Thermtest Instruments. (2021). https://thermtest.com/thermal-resources/materials-database (accessed November 2, 2021).

[65] N. Yang, J. Yee, B. Zheng, K. Gaiser, T. Reynolds, L. Clemon, W.Y. Lu, J.M. Schoenung, E.J. Lavernia, Process-Structure-Property Relationships for 316L Stainless Steel Fabricated by Additive Manufacturing and Its Implication for Component

Engineering, J. Therm. Spray Technol. 26 (2017) 610–626. https://doi.org/10.1007/s11666-016-0480-y.

[66] O. Carrier, D. Bonn, Chapter 2 - Contact Angles and the Surface Free Energy of Solids, in: D.B.T.-D.W. and E. Brutin (Ed.), Academic Press, Oxford, 2015: pp. 15–23. https://doi.org/https://doi.org/10.1016/B978-0-12-800722-8.00002-3.

[67] J.L. Shereshefsky, Surface Tension of Saturated Vapors and the Equation of Eötvös, J. Phys. Chem. 35 (1931) 1712–1720. https://doi.org/10.1021/j150324a014.

[68] J. Song, L. Fan, Temperature dependence of the contact angle of water: A review of research progress, theoretical understanding, and implications for boiling heat transfer, Adv. Colloid Interface Sci. 288 (2020) 102339. https://doi.org/10.1016/j.cis.2020.102339.

[69] M.T. Ensz, M.L. Griffith, L.D. Harwell, Software development for Laser Engineered Net Shaping, in: United States, 1998. https://www.osti.gov/biblio/656769.

[70] K. Guan, Z. Wang, M. Gao, X. Li, X. Zeng, Effects of processing parameters on tensile properties of selective laser melted 304 stainless steel, Mater. Des. 50 (2013) 581–586. https://doi.org/https://doi.org/10.1016/j.matdes.2013.03.056.

[71] T. Vilaro, C. Colin, J.D. Bartout, As-Fabricated and Heat-Treated Microstructures of the Ti-6Al-4V Alloy Processed by Selective Laser Melting, Metall. Mater. Trans. A. 42 (2011) 3190–3199. https://doi.org/10.1007/s11661-011-0731-y.

[72] P. Peyre, P. Aubry, R. Fabbro, R. Neveu, A. Longuet, Analytical and numerical modelling of the direct metal deposition laser process, J. Phys. D. Appl. Phys. 41 (2008) 25403. https://doi.org/10.1088/0022-3727/41/2/025403.

[73] I.A. Roberts, C.J. Wang, R. Esterlein, M. Stanford, D.J. Mynors, A three-dimensional finite element analysis of the temperature field during laser melting of metal powders in additive layer manufacturing, Int. J. Mach. Tools Manuf. 49 (2009) 916–923. https://doi.org/https://doi.org/10.1016/j.ijmachtools.2009.07.004.

[74] A.M. Roach, B.C. White, A. Garland, B.H. Jared, J.D. Carroll, B.L. Boyce, Size-dependent stochastic tensile properties in additively manufactured 316L stainless steel, Addit. Manuf. 32 (2020) 101090. https://doi.org/https://doi.org/10.1016/j.addma.2020.101090.

[75] B. Brown, W. Everhart, J. Dinardo, Characterization of bulk to thin wall mechanical response transition in powder bed AM, Rapid Prototyp. J. 22 (2016) 801–809. https://doi.org/10.1108/RPJ-10-2015-0146.

[76] S.M.J. Razavi, B. Van Hooreweder, F. Berto, Effect of build thickness and geometry on quasi-static and fatigue behavior of Ti-6Al-4V produced by Electron Beam Melting, Addit. Manuf. 36 (2020) 101426. https://doi.org/https://doi.org/10.1016/j.addma.2020.101426.

[77] X. Tan, Y. Kok, Y.J. Tan, G. Vastola, Q.X. Pei, G. Zhang, Y.-W. Zhang, S.B. Tor, K.F. Leong, C.K. Chua, An experimental and simulation study on build thickness dependent microstructure for electron beam melted Ti–6Al–4V, J. Alloys Compd. 646 (2015) 303–309. https://doi.org/https://doi.org/10.1016/j.jallcom.2015.05.178.

[78] A. Majeed, A. Ahmed, B. Liu, S. Ren, Influence of wall thickness on the hardness of AlSi10Mg alloy parts manufactured by selective laser melting, 81 (2019) 459–463. https://doi.org/10.1016/j.procir.2019.03.079.

[79] M.R. Stoudt, M.E. Williams, L.E. Levine, A. Creuziger, S.A. Young, J.C. Heigel, B.M. Lane, T.Q. Phan, Location-Specific Microstructure Characterization Within IN625 Additive Manufacturing Benchmark Test Artifacts, Integr. Mater. Manuf. Innov. 9 (2020) 54–69. https://doi.org/10.1007/s40192-020-00172-6.

[80] U. Scipioni Bertoli, B.E. MacDonald, J.M. Schoenung, Stability of cellular microstructure in laser powder bed fusion of 316L stainless steel, Mater. Sci. Eng. A. 739 (2019) 109–117. https://doi.org/https://doi.org/10.1016/j.msea.2018.10.051.

[81] M. Letenneur, A. Kreitcberg, V. Brailovski, The Average Grain Size and Grain Aspect Ratio in Metal Laser Powder Bed Fusion: Modeling and Experiment, J. Manuf. Mater. Process. . 4 (2020). https://doi.org/10.3390/jmmp4010025.

[82] M.B. Henderson, D. Arrell, R. Larsson, M. Heobel, G. Marchant, Nickel based superalloy welding practices for industrial gas turbine applications, Sci. Technol. Weld. Join. 9 (2004) 13–21. https://doi.org/10.1179/136217104225017099.

[83] D.E. Cooper, N. Blundell, S. Maggs, G.J. Gibbons, Additive layer manufacture of Inconel 625 metal matrix composites, reinforcement material evaluation, J. Mater. Process. Technol. 213 (2013) 2191–2200. https://doi.org/https://doi.org/10.1016/j.jmatprotec.2013.06.021.

[84] S. Cao, D. Gu, Q. Shi, Relation of microstructure, microhardness and underlying thermodynamics in molten pools of laser melting deposition processed TiC/Inconel 625 composites, J. Alloys Compd. 692 (2016). https://doi.org/10.1016/j.jallcom.2016.09.098.

[85] R. Mahamood, E. Akinlabi, D.M. Shukla, S. Pityana, Scanning velocity influence on microstructure, microhardness and wear resistance performance of laser deposited Ti6Al4V/TiC composite, Mater. Des. 50 (2013) 656–666. https://doi.org/10.1016/j.matdes.2013.03.049.

[86] S. Cao, D. Gu, Laser metal deposition additive manufacturing of TiC/Inconel 625 nanocomposites: Relation of densification, microstructures and performance, J. Mater. Res. 30 (2015) 3616–3628. https://doi.org/DOI: 10.1557/jmr.2015.358.

[87] D. Gu, J. Ma, H. Chen, K. Lin, L. Xi, Laser additive manufactured WC reinforced Fe-based composites with gradient reinforcement/matrix interface and enhanced performance, Compos. Struct. 192 (2018) 387–396. https://doi.org/https://doi.org/10.1016/j.compstruct.2018.03.008.

[88] T.W. Clyne, 4.1 An Introductory Overview of Metal Matrix Composites Systems, Types and Developments, in: P.W.R. Beaumont, C.H.B.T.-C.C.M.I.I. Zweben (Eds.), Elsevier, Oxford, 2018: pp. 1–21. https://doi.org/https://doi.org/10.1016/B978-0-12-803581-8.09961-6.

[89] F. Liu, X. Lin, G. Yang, M. Song, J. Chen, W. Huang, Microstructure and residual stress of laser rapid formed Inconel 718 nickel-base superalloy, Opt. Laser Technol. 43 (2011) 208–213. https://doi.org/10.1016/j.optlastec.2010.06.015.

[90] A. Mostafa, I. Rubio, V. Brailovski, M. Jahazi, M. Medraj, Structure, Texture and Phases in 3D Printed IN718 Alloy Subjected to Homogenization and HIP Treatments, Met. - Open Access Metall. J. 7 (2017) 196. https://doi.org/10.3390/met7060196.

[91] L. Pike, HAYNES® 282™ Alloy: A New Wrought Superalloy Designed for Improved Creep Strength and Fabricability, 2006. https://doi.org/10.1115/GT2006-91204.

[92] C. Hong, D. Gu, D. Dai, A. Gasser, A. Weisheit, I. Kelbassa, M. Zhong, R. Poprawe, Laser metal deposition of TiC/Inconel 718 composites with tailored interfacial microstructures, Opt. Laser Technol. 54 (2013) 98–109. https://doi.org/https://doi.org/10.1016/j.optlastec.2013.05.011.

[93] H. Xiao, S. Li, X. Han, J. Mazumder, L. Song, Laves phase control of Inconel 718 alloy using quasi-continuous-wave laser additive manufacturing, Mater. Des. 122 (2017) 330–339. https://doi.org/https://doi.org/10.1016/j.matdes.2017.03.004.

[94] A. Ramakrishnan, G.P. Dinda, Functionally graded metal matrix composite of Haynes 282 and SiC fabricated by laser metal deposition, Mater. Des. 179 (2019) 107877. https://doi.org/https://doi.org/10.1016/j.matdes.2019.107877.

[95] A. Ramakrishnan, G.P. Dinda, Microstructure and mechanical properties of direct laser metal deposited Haynes 282 superalloy, Mater. Sci. Eng. A. 748 (2019) 347–356. https://doi.org/https://doi.org/10.1016/j.msea.2019.01.101.

[96] M.J. Sohrabi, H. Mirzadeh, M. Rafiei, Solidification behavior and Laves phase dissolution during homogenization heat treatment of Inconel 718 superalloy, Vacuum. 154 (2018) 235–243. https://doi.org/https://doi.org/10.1016/j.vacuum.2018.05.019.

[97] D. Sivakumar, M. Kamaraj, P. Kalvala, Laves Phase Control in Inconel 718 Weldments, Mater. Sci. Forum. (2012).

[98] K.K. Chawla, N. Chawla, Thermal Shock Behavior of Ceramic Matrix Composites BT - Encyclopedia of Thermal Stresses, in: R.B. Hetnarski (Ed.), Springer Netherlands, Dordrecht, 2014: pp. 5114–5119. https://doi.org/10.1007/978-94-007-2739-7_94.

[99] R.J. Arsenault, N. Shi, Dislocation generation due to differences between the coefficients of thermal expansion, Mater. Sci. Eng. 81 (1986) 175–187. https://doi.org/https://doi.org/10.1016/0025-5416(86)90261-2.

[100] M. Taya, K.E. Lulay, D.J. Lloyd, Strengthening of a particulate metal matrix composite by quenching, Acta Metall. Mater. 39 (1991) 73–87. https://doi.org/https://doi.org/10.1016/0956-7151(91)90329-Y.

[101] N. Chawla, Y.-L. Shen, Mechanical Behavior of Particle Reinforced Metal Matrix Composites, Adv. Eng. Mater. 3 (2001) 357–370. https://doi.org/https://doi.org/10.1002/1527-2648(200106)3:6<357::AID-ADEM357>3.0.CO;2-I.

[102] D. Gu, C. Hong, Q. Jia, D. Dai, A. Gasser, A. Weisheit, I. Kelbassa, M. Zhong, R. Poprawe, Combined strengthening of multi-phase and graded interface in laser additive manufactured TiC/Inconel 718 composites, J. Phys. D. Appl. Phys. 47 (2013) 45309. https://doi.org/10.1088/0022-3727/47/4/045309.

[103] W. Yang, W. Chen, K.-M. Chang, S. Mannan, J. deBarbadillo, Segregation and Solid Evolution During the Solidification of Niobium-Containing Superalloys, 2000. https://doi.org/10.7449/2000/Superalloys_2000_75_84.

[104] E. Scheil, Bemerkungen zur Schichtkristallbildung, Int. J. Mater. Res. 34 (1942) 70–72. https://doi.org/doi:10.1515/ijmr-1942-340303.

[105] M. Donachie, S. Donachie, Superalloys: A Technical Guide, 2nd Edition, 2002. https://doi.org/10.31399/asm.tb.stg2.9781627082679.

[106] J. Chen, J.H. Lee, C.Y. Jo, S.J. Choe, Y.T. Lee, MC carbide formation in directionally solidified MAR-M247 LC superalloy, Mater. Sci. Eng. A. 247 (1998) 113–125. https://doi.org/https://doi.org/10.1016/S0921-5093(97)00761-2.

[107] B.-X. Dong, F. Qiu, Q. Li, S.-L. Shu, H.-Y. Yang, Q.-C. Jiang, The Synthesis, Structure, Morphology Characterizations and Evolution Mechanisms of Nanosized Titanium Carbides and Their Further Applications, Nanomater. (Basel, Switzerland). 9 (2019) 1152. https://doi.org/10.3390/nano9081152.

[108] B. DERBY, Microstructure and fracture behaviour of particle-reinforced metal–matrix composites, J. Microsc. 177 (1995) 357–368. https://doi.org/https://doi.org/10.1111/j.1365-2818.1995.tb03567.x.

[109] X. Xia, H.J. McQueen, H. Zhu, Fracture Behavior of Particle Reinforced Metal Matrix Composites, Appl. Compos. Mater. 9 (2002) 17–31. https://doi.org/10.1023/A:1012605425351.

[110] Y. Chen, S.J. Clark, L. Sinclair, C.L.A. Leung, S. Marussi, T. Connolley, R.C. Atwood, G.J. Baxter, M.A. Jones, I. Todd, P.D. Lee, Synchrotron X-ray imaging of directed energy deposition additive manufacturing of titanium alloy Ti-6242, Addit. Manuf. 41 (2021) 101969. https://doi.org/https://doi.org/10.1016/j.addma.2021.101969.

[111] C.L.A. Leung, S. Marussi, M. Towrie, J. del Val Garcia, R.C. Atwood, A.J. Bodey, J.R. Jones, P.J. Withers, P.D. Lee, Laser-matter interactions in additive manufacturing of stainless steel SS316L and 13-93 bioactive glass revealed by in situ X-ray imaging, Addit. Manuf. 24 (2018) 647–657. https://doi.org/https://doi.org/10.1016/j.addma.2018.08.025.